
Electronic Thesis and Dissertation Repository

8-23-2013 12:00 AM

Molecular Gas in the Circumstellar Environment of Unusual Evolved Stars

Sarah E. Malek
The University of Western Ontario

Supervisor
Jan Cami
The University of Western Ontario

Graduate Program in Astronomy
A thesis submitted in partial fulfillment of the requirements for the degree in Doctor of Philosophy
© Sarah E. Malek 2013

Follow this and additional works at: <https://ir.lib.uwo.ca/etd>



Part of the [Other Astrophysics and Astronomy Commons](#), and the [Physical Processes Commons](#)

Recommended Citation

Malek, Sarah E., "Molecular Gas in the Circumstellar Environment of Unusual Evolved Stars" (2013).
Electronic Thesis and Dissertation Repository. 1570.
<https://ir.lib.uwo.ca/etd/1570>

This Dissertation/Thesis is brought to you for free and open access by Scholarship@Western. It has been accepted for inclusion in Electronic Thesis and Dissertation Repository by an authorized administrator of Scholarship@Western. For more information, please contact wlsadmin@uwo.ca.

MOLECULAR GAS IN THE CIRCUMSTELLAR ENVIRONMENT OF
UNUSUAL EVOLVED STARS
(Thesis format: Integrated Article)

by

Sarah Malek

Graduate Program in Physics and Astronomy

A thesis submitted in partial fulfillment
of the requirements for the degree of
Doctor of Philosophy

The School of Graduate and Postdoctoral Studies
The University of Western Ontario
London, Ontario, Canada

© Sarah Elizabeth Malek 2013

Abstract

As low- and intermediate mass stars ($M_{\star} < 8-9 M_{\odot}$) age, they experience a series of evolutionary changes which culminate in the removal of nearly their entire envelope through extensive mass loss. The ejected material cools down, which allows for the formation of molecules and the nucleation of dust grains in the circumstellar environment (CSE) of the star. Much about the properties and composition of the gas and dust in these CSEs is not well understood.

Here, we study the rich CSEs of two unusual evolved stars by analyzing spectral observations in the infrared and using molecular spectroscopy to determine the chemical and physical properties of the circumstellar gas.

We first present the mid-infrared spectrum of the carbon-rich pre-planetary nebula SMP LMC 11. The spectrum is rich in molecular bands from a variety of species, including several polyyne and cyanopolyyne and unusually strong absorption from benzene. We also confirm the presence of propyne. We find that this molecular gas resides in a dense torus around the central object. A detailed comparison with results from chemical models indicates that important chemical pathways to benzene and other carbon-rich molecules are currently missing from the models.

Next, we analyze the molecular gas in the mid- and near-infrared spectrum of the peculiar evolved binary HR 4049. This system is known to be surrounded by a long-lived circumbinary disk. We find that the disk is gas-rich, hot, massive and much more radially extended than previously thought. A recent and significant increase in CO_2 emission may also point to ongoing processing in the disk. Given the column densities of especially CO_2 and H_2O in the disk, radiative trapping must be an important ingredient in determining the physical structure of the disk and its resulting spectrum. Such effects may well be important in many other circumstellar environments as well. Finally, we can also estimate the mass of the primary, and conclude that it may be too low for the star to have experienced a “normal” evolutionary path.

Keywords: astrochemistry, binaries: spectroscopic, circumstellar matter, planetary nebulae, stars: AGB and post-AGB, stars: carbon, stars: evolution, techniques: spectroscopic

Co-Authorship Statement

I would like to acknowledge J. Bernard-Salas, who contributed to the paper *The Rich Circumstellar Chemistry of SMP LMC 11* by providing feedback and suggestions for improving the text and analysis.

I would also like to acknowledge J. Cami, who contributed to all three papers in this thesis by providing the initial ideas for the projects, helping to guide the analysis as well as providing feedback and suggestions for improving the text.

Acknowledgements

First of all, I would like to thank my supervisor, Jan. You've taught me so much over the years and have patiently put up with me and helped me through even the most frustrating times (which were perhaps more frequent recently). Also thank you for believing in me and encouraging me; I could not have succeeded without you. I'm going to miss getting to work with you as well as getting to spend time with you at the security meetings on Friday afternoons.

I would also like to thank the members of my group: Neil, Sanaz, Cameron, Elisabetta and Hoda. I've really enjoyed our meetings and the different perspectives each of you bring to different research topics as well as hearing about your work. As well, thank you all for your encouragement and support. Elisabetta, thank you for your advice about career and thesis writing as well, it's been very helpful and has meant a lot to me.

I would also like to thank the members of my advisory committee Pauline and Carol. Your feedback over the years has been really helpful and has made me better at presenting my work. Pauline, I also enjoy our chats about knitting.

In my graduate career, I have been fortunate enough to meet and befriend many wonderful people. Were it not for your support and friendships, I could not have made it this far. That said, I'm going to try to keep this short.

Tyler, I really appreciate our chats and the fact that you give me excuses to take well-needed breaks. Also, thank you for your candour and your advice.

Alex, thank you for being a great friend and letting me vent when I've been stressed out as well as letting me ramble on about my research. Also, thank you for continuing to talk to me even though I got you to cat sit that one time and you got to find out how my apartment sometimes has a bat problem. I probably still owe you for that.

Samantha, thank you for being an awesome friend. You've always been there when I needed to talk and for some reason, you seem to have a lot of confidence in me and I really appreciate this. Also, thank you for being as wonderfully blunt as you are.

Martin, you're an excellent teacher and I've learned a lot from you. Also, thank you for great conversations and for making sure that my glass doesn't stay empty very long (except that one time).

Scott, thank you for your friendship and for regularly coming out for some drinks when I've needed a break or to celebrate something (even when you're busy too). Also, thank you for taking over making coffee when I was getting really busy, I totally needed that.

Sophia, you've been really encouraging and supportive when I needed it, so thank you for that. I'll also never forget how excellent a hostess you are and I hope someday you'll visit me wherever I end up and return the favour.

Dave, I appreciate your advice and insights, both in research and in job hunting. Thank you for being willing to listen to various frustrations as well.

Rob, I've enjoyed our time hanging out at the Grad Club and thank you for all the advice and tips on finishing the thesis. It's been really helpful to hear this firsthand from someone who's been through this particular system.

Andrew and Shiva, thanks for inviting me along on random adventures when I was stressed out and needed to take my mind off things.

I would also like to thank my family, especially my parents. Without your love, support and encouragement, I would not be the person I am today, nor would I have been capable of accomplishing the things I have accomplished. Thank you both for encouraging me to learn new things and letting me explore things that I think are interesting, even when they aren't practical. Mom, thank you for understanding that I haven't been able to come visit very often. Dad, thank you for instilling me with a love of science and teaching me about the stars.

Finally, I would like to thank daid. Even though you've been on the other side of the planet, I've probably shared more of my frustrations with you than anyone else and even if you can't do much about it, you usually know how to make me feel better. You may also be one of the few people who has voluntarily read all my papers without prompting. Your love and encouragement mean world to me.

The beauty of a living thing is not the atoms that go into it, but the way the atoms are put together. The cosmos is also within us. We're made of star stuff, we are a way for the cosmos to know itself.

Carl Sagan

Contents

Abstract	ii
Co-Authorship Statement	iii
Acknowledgments	iv
List of Figures	xi
List of Tables	xiii
List of Appendices	xiv
List of Abbreviations, Symbols, and Nomenclature	xv
1 Introduction	1
1.1 Stellar Evolution of Low- and Intermediate-Mass Stars	3
1.1.1 From Molecular Clouds to the Main Sequence	3
1.1.2 The Main Sequence	4
1.1.3 Post-Main Sequence	7
1.1.4 Nucleosynthesis	12
Hydrogen burning	12
Helium burning	14
s-process	14
Hot Bottom Burning	15
1.1.5 Dredge-Ups	15
1.1.6 From oxygen-rich AGB star to carbon star	16
1.1.7 Mass Loss	16
Mechanisms	17
Observations	18
1.1.8 Evolution in Binary Systems	18
1.2 Circumstellar Environment	20

1.2.1	Carbon versus Oxygen-rich Chemistry	20
1.2.2	Molecules	21
1.2.3	Dust	24
1.3	Spectroscopic Analysis of CSEs	25
	Molecular Spectroscopy	26
	Dust	27
1.4	Open Problems	27
1.5	This Thesis	28
2	Spitzer data reduction	35
2.1	Spitzer-IRS Observations	35
2.2	Using SMART	37
2.3	Custom Routines	37
2.3.1	Finishing Touches and Notes	40
3	Circumstellar Chemistry of SMP LMC 11	42
3.1	Introduction	42
3.2	Observations and Data Reduction	44
3.3	The dust continuum	44
3.4	Molecular bands	46
3.4.1	Molecular Inventory	46
3.4.2	Modeling the molecular absorption	47
3.5	Results	48
3.5.1	Benzene	49
3.5.2	Acetylene Chains	51
3.5.3	Cyanopolyynes	53
3.5.4	Other Species	54
3.6	Discussion	54
3.6.1	Circumstellar geometry	54
3.6.2	The chemistry in SMP LMC 11	56
3.6.3	Pathways to PAHs?	57
3.7	Conclusions	58
4	A Detailed Study of the Mid-Infrared Spectrum of HR 4049	63
4.1	Introduction	63
4.2	Observations and Data Reduction	66
4.2.1	Spitzer-IRS	66

4.2.2	ISO-SWS	66
4.3	Analysis	67
4.3.1	Modeling the Spitzer Spectrum	68
4.4	Results	69
4.4.1	CO ₂	70
4.4.2	H ₂ O and OH	71
4.4.3	HCN	72
4.4.4	Fullerenes	73
4.4.5	PAHs	73
4.4.6	Residual Features	73
4.4.7	ISO Spectrum	75
4.5	Discussion	77
4.5.1	Isotopic Ratios	77
4.5.2	Gas Distribution and Disk Structure	78
4.5.3	Total Gas Mass	80
4.5.4	Time Evolution	81
4.6	Conclusion	83
5	A Detailed study of the Near-Infrared Spectrum of HR 4049	87
5.1	Introduction	87
5.2	Observations	89
5.3	Analysis	89
5.3.1	The 2.3 μ m Region	90
H ₂ O	94	
5.3.2	The 4.6 μ m Region	95
5.3.3	Kinematics	97
5.4	Discussion	100
5.4.1	Dust Temperatures	101
5.4.2	The size of the gas disk	101
5.4.3	On the Mass of HR 4049	102
5.5	Conclusion	103
6	Conclusions and Future Work	106
A	Model Spectra	110
A.1	Optical Depth Profiles	110
A.2	Single Layer Model	112

A.2.1	Effects of Temperature and Column Density	113
A.3	Statistical Techniques	117
A.4	Multi-Layer Models	119
Curriculum Vitae		122

List of Figures

1.1	The stellar life cycle	2
1.2	A Hertzsprung-Russel diagram	5
1.3	Colour magnitude diagram of M3	6
1.4	Core densities and temperatures through the stellar life cycle	9
1.5	Schematic of an AGB star and its CSE	10
1.6	Comparing the spectra of oxygen-rich, carbon-rich and mixed chemistry circumstellar environments	22
2.1	An example of partially reduced data	38
2.2	An example of the final steps	39
3.1	Low resolution spectrum of SMP LMC 11.	45
3.2	Normalized spectrum of SMP LMC 11 with model fits.	50
3.3	The benzene bands at 6.8 and 14.8 μm in SMP LMC 11	52
3.4	The SMP LMC 11 compared to CRL 618 at 16 μm	53
4.1	Spitzer-IRS and ISO-SWS observations of HR 4049	67
4.2	Spitzer-IRS spectrum of HR 4049 with best fit model to molecular emission between 10 and 20 μm	69
4.3	Spitzer-IRS spectrum of HR 4049 at LH wavelengths with H ₂ O and OH models.	71
4.4	Full wavelength Spitzer-IRS and ISO-SWS spectra compared to best fit models.	76
5.1	Normalized spectrum of HR 4049 at 2.3 μm with model fits	91
5.2	Excitation diagram for CO overtone absorption in HR 4049	92
5.3	HR 4049 spectrum and model predictions at 4.6 μm	95
5.4	Comparison of radial velocities and line widths of the CO overtone in HR 4049	98
5.5	Comparison of overtone and fundamental line profiles for CO	99
A.1	CO ₂ at different temperatures and column densities (15 μm band).	114
A.2	CO ₂ at different temperatures and column densities (15 μm band).	115
A.3	CO ₂ at different temperatures and column densities (4 μm band)	116

A.4 A schematic of a two layer model. 120

List of Tables

1.1	Molecules found in the circumstellar environments of oxygen-rich, carbon- and s-stars.	23
1.2	Dust species found in the circumstellar environments of oxygen-rich, carbon- and s-stars	25
2.1	Description of the observing modes for Spitzer-IRS	36
3.1	Parameters for the model fit to the spectrum of SMP LMC 11	49
4.1	Parameters for the model fit to the mid-infrared spectrum of HR 4049	70
5.1	Parameters for the excitation diagram and model fits for HR 4049	94
A.1	Transition wavelengths with corresponding upper and lower vibrational states for the main CO ₂ isotopologue in the 10—19 μm range.	118

List of Appendices

Appendix A Model Spectra	110
------------------------------------	-----

List of Abbreviations, Symbols, and Nomenclature

Abbreviation	Definition
2MASS	– Two Micron All Sky Survey
AGB	– asymptotic giant branch
AOR	– astronomical observation request
AU	– astronomical unit (1 AU = 1.4960×10^{13} cm)
bcd	– basic caillibrated data
CMD	– colour magnitude diagram
CNO	– carbon nitrogen and oxygen
CRL #	– Cambridge Research Lab #
CSE	– circumstellar environment
DCE	– data collection event
FWHM	– full width at half maximum
Gyr	– Gigayear 1 Gyr = 10^9 yr
HB	– horizontal branch
HBB	– hot bottom burning
HR	– Hertzsprung-Russel diagram
HR #	– Harvard Revised Photometry Catalogue #
IDL	– Interactive Data Language
IR	– infrared
IRAS	– Infrared Astronomical Satellite
IRC #	– Infrared Catalogue #
IRS	– Infrared Spectrograph
ISM	– interstellar medium
ISO	– Infrared Space Observatory
Jy	– Jansky (1 Jy = 10^{-23} erg s ⁻¹ cm ⁻² Hz ⁻¹)
LH	– long high
LL	– long low
LMC	– Large Magellanic Cloud
LTE	– local thermodynamic equilibrium
MS	– main sequence
Myr	– Megayear 1 Myr = 10^6 yr
PAH	– polycyclic aromatic hydrocarbon
pc	– parsec (1 pc = 3.00857×10^{18} cm)
(p)PN	– (pre-)planetary nebula

RGB	– red giant branch
SGB	– sub giant branch
SH	– short high
SL	– short low
SMART	– Spectroscopic Modeling Analysis and Reduction Tool
SMC	– Small Magellanic Cloud
SMP #	– Sanduleak MacConnell and Phillip catalogue #
S/N	– signal-to-noise
submm	– sub-millimetre
SWS	– Short Wavelength Spectrometer
UV	– ultra violet

Symbol	– Definition
A_{21}	– Einstein A coefficient for spontaneous emission
B_{21}	– Einstein B coefficient for stimulated emission
B_{12}	– Einstein A coefficient for absorption
E	– Energy (in units of cm^{-1})
G	– gravitational constant ($G = 6.67259 \times 10^{-8} \text{ dyne cm}^2 \text{ g}^{-2}$)
I_ν	– intensity (in units of $\text{erg s}^{-1} \text{ cm}^{-2} \text{ ster}^{-1} \text{ Hz}^{-1}$)
F_ν	– flux (in units of Jy)
h	– Planck constant ($h = 6.62606957 \times 10^{-27} \text{ erg s}$)
J	– rotational quantum number
k	– Boltzmann constant ($k = 1.3807 \times 10^{-16} \text{ erg K}^{-1}$)
L	– luminosity (units of erg s^{-1})
L_\odot	– solar luminosity ($3.898 \times 10^{33} \text{ erg s}^{-1}$)
M_\odot	– Solar mass ($1 M_\odot = 1.989 \times 10^{33} \text{ g}$)
N	– column density (units of cm^{-2})
R	– spectral resolution ($R = \lambda(\Delta\lambda)^{-1}$)
R_\odot	– Solar radius ($1 R_\odot = 6.9599 \times 10^{10} \text{ cm}$)
T	– temperature (units of K)
T_{eff}	– effective temperature (units of K)
ν	– vibrational quantum number
$\nu_\#$	– vibrational mode # for polyatomic molecules
ν_{rad}	– radial velocity (units of km s^{-1})
α	– ^4He nucleus
λ	– wavelength (in μm)
σ	– standard deviation

τ	– optical depth
ν	– frequency (in units of Hz)
	– degrees of freedom (in context of statistical analysis)
χ^2_ν	– reduced χ^2 function

Chapter 1

Introduction

It was once thought that the stars in the sky did not change; for example, Aristotle described a cosmos in which the stars were perfect spheres, eternal and unchanging. This idea persisted for a very long time and it seems quite reasonable; for instance, ancient star charts mostly resemble our own, indicating that the stars have not changed much since ancient astronomers began to observe the night sky.

However, we now know that this is not quite true. Not only are some stars observed to change dramatically in their appearance (e.g. their magnitude) over time scales ranging from hours to millenia, but we have determined that stars are born, they age and they die—they evolve. This occurs over very long timescales, much longer than human lifetimes, which is why the sky seems so unchanged since antiquity. Thus, although stars live significantly longer than we do—and many will outlast our own Sun—they will all die out eventually.

Stars are part of a cosmic circle of life, as illustrated in Figure 1.1; they are born from clouds of gas and dust in the interstellar medium (ISM). Then, throughout their lives they turn lighter elements into heavier ones, which generates the energy that makes them shine. This process of converting lighter elements into heavier ones also causes them to evolve and, eventually, to die. After they die, stars return much of their material—enriched by the heavier elements produced throughout their lives—to the ISM. Some of this material will make its way into the next generation of stars in a large scale cosmic recycling process. This process is crucial for the existence of life, for we, and everything around us, are mostly composed of these heavier elements.

As depicted in Figure 1.1, the high-mass stars (stars with masses greater than 8 – 9 solar masses; $M_{\star} > 8 - 9 M_{\odot}$) experience a different evolutionary path than their low- and intermediate-mass counterparts. These stars form successively heavier elements and continue to evolve until they begin to create iron in their centres. They are unable to gain energy from creating elements heavier than this, so their cores collapse and they undergo very energetic explosions known as supernovae. The evolution of these high-mass stars is beyond the scope of

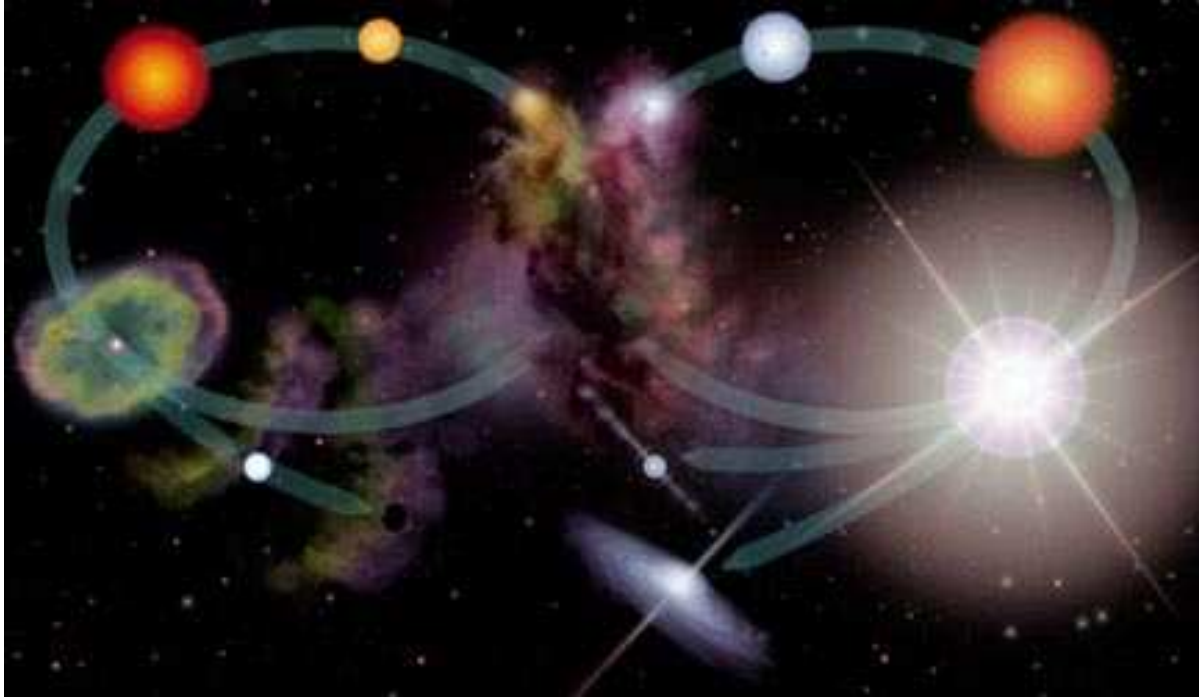


Figure 1.1: The stellar life cycles for low- and intermediate-mass stars (left, moving counter clockwise from centre) and high-mass stars (right, clockwise). In the centre, we see a depiction of a star forming region. Once the stars are born, we see them move onto the main sequence and eventually they become giants. The high-mass stars rapidly eject mass as they terminate their evolution in supernovae, leaving behind a black hole or neutron star while the low- and intermediate-mass stars slowly lose mass, becoming planetary nebulae and then white dwarfs. The material from these stars returns to the ISM where it is recycled into the next generation of stars.

the current work, however, so we refer the interested reader to Woosley et al. (2002); Woosley & Weaver (1986) for a review.

Low- and intermediate-mass stars ($0.8 M_{\odot} < M_{\star} < 2.3 M_{\odot}$ and $2.3 M_{\odot} < M_{\star} < 8 - 9 M_{\odot}$ respectively) undergo a much quieter evolution. Instead of exploding as supernovae, they become cool giants and gradually lose mass. These stars do not form elements much heavier than carbon and oxygen, and individually they do not return as much material to the ISM as their high-mass counterparts. However, since they are much more abundant, they are collectively responsible for recycling $\sim 90\%$ of all material to the ISM (Stahler & Palla, 2004).

Before returning to the ISM, the material lost by these stars undergoes (often extensive) processing in warm, relatively dense regions known as circumstellar environments (CSEs). In these environments, a rich chemistry will often occur, resulting in the formation of large and complex molecular species and dust minerals which play important roles in the ISM. However,

the chemical networks giving rise to these species and the conditions under which they form and are processed are often not well established. In addition, the effects of binarity on the evolution of low- and intermediate-mass stars and their circumbinary environments are not understood either. The research presented in this thesis will address some of these issues, but first, we will describe aspects of stellar evolution, mass loss and circumstellar environments, and spectroscopy that are necessary to understand the relevance and importance of these open questions.

This chapter is organized as follows: We begin with an overview of stellar evolution in Section 1.1 which we follow with a description of the circumstellar environment (CSE) that forms around highly evolved stars in Section 1.2. Then we briefly describe the use of spectroscopy in studying these CSEs in Section 1.3. Next, in Section 1.4, we summarize the open problems and finally, in Section 1.5, we outline the structure of this thesis.

1.1 Stellar Evolution of Low- and Intermediate-Mass Stars

1.1.1 From Molecular Clouds to the Main Sequence

Stars are born in clusters from large, relatively dense collections of gas and dust in the ISM known as giant molecular clouds (with masses up to $10^6 M_{\odot}$, average densities $n_{\text{H}_2} \approx 20 \text{ cm}^{-3}$ and diameters, $d \approx 100 \text{ pc}$, Larson, 2003). These molecular clouds may begin to experience gravitational contraction when some external force (e.g. collision with another molecular cloud) compresses them. As a molecular cloud contracts, it fragments into many smaller, denser pieces known as clumps ($M \approx 10^3 M_{\odot}$, $n_{\text{H}_2} \approx 10^3 \text{ cm}^{-3}$, $d \approx 1 \text{ pc}$) which can fragment further into cores ($M \approx 1 M_{\odot}$, $n_{\text{H}_2} \approx 10^5 \text{ cm}^{-3}$, $d \approx 0.1 \text{ pc}$) which continue to contract under their own gravitation, potentially each forming a star or multiple-star system.

As the cores contract, they convert gravitational potential energy, to kinetic energy creating additional thermal pressure which would prevent further contraction. In order for the core to continue contracting instead of dispersing, some of this energy must be removed. This is typically accomplished through molecules (especially CO) which convert energy from collisions into rotational and vibrational energy which they radiate away (Gilden, 1984).

When the centre becomes hot and dense enough, hydrogen fusion is ignited which creates sufficient thermal pressure in the core to support the star against further gravitational contraction. Thus, a star is born and moves onto what is known as the main sequence (MS).

1.1.2 The Main Sequence

While on the main sequence, a star quiescently burns hydrogen into helium in its core through the proton-proton chain (or pp chain) and the carbon-nitrogen-oxygen (CNO) cycle (described further in Section 1.1.4). While some amount of both of these processes occur in all stars on the MS, one or the other dominates depending on the initial mass of the star, which determines the temperature of its core. Although both processes become more efficient at higher temperatures, the CNO cycle is more sensitive to temperature than the pp chain, so it becomes even more efficient if the temperature increases. Thus, in stars with initial masses less than $1.5 M_{\odot}$ which have relatively cool cores, the pp chain is the dominant mechanism for hydrogen fusion while for stars with masses greater than $1.5 M_{\odot}$, the CNO cycle dominates.

Since the CNO cycle is so temperature dependent, the hydrogen fusion in a star with mass greater than $1.5 M_{\odot}$ is highly concentrated in the centre of its core, causing a steep temperature gradient. The result of this temperature gradient is that energy is transported through the core by convection—where parcels of gas rise and fall. Then energy is transported through its envelope—the region above the core—by radiation before escaping the star entirely. For stars between $0.5 M_{\odot}$ and $1.5 M_{\odot}$, the reverse is true; these stars transport energy radiatively in their cores and have convective envelopes. Finally, stars with masses less than $0.5 M_{\odot}$ are fully convective and material is mixed all the way from their cores to their surfaces.

Observations of large numbers of MS stars reveal particular patterns on two types of diagrams which are commonly used to describe some of the properties of stars: Hertzsprung-Russell diagrams (HR diagrams, see Figure 1.2) and colour magnitude diagrams (CMDs, see Figure 1.3). Due to the utility of these diagrams in describing various stages in stellar evolution as well as properties of stars, we will take a moment to describe them in some detail.

An HR diagram is a plot of the effective temperature (or surface temperature) of a star on the horizontal axis (with higher temperatures on the left and lower temperatures on the right) versus the luminosity of a star (the rate at which energy leaves its surface) on the vertical axis. In Figure 1.2, we show theoretical evolutionary tracks for two stars of different masses as well as the zero age main sequence (ZAMS), indicating the temperatures and luminosities of stars with a range of masses when they first arrive on the MS. Here, we see that the $5 M_{\odot}$ has a higher effective temperature and luminosity on the MS than the $1 M_{\odot}$ star. Indeed, stars with higher masses still will fall closer to the top left on the ZAMS and stars with masses lower than $1 M_{\odot}$ will fall closer to the bottom right on the MS. In general, the stars toward the top of the HR diagram have larger radii (R_{\star}) than those at the bottom since radius squared is proportional to the luminosity ($L_{\star} \propto R_{\star}^2$). The stars in the top right of this diagram (the cool giants) have the largest radii.

A CMD is a similar plot which is typically used for observational purposes. Here, the colour

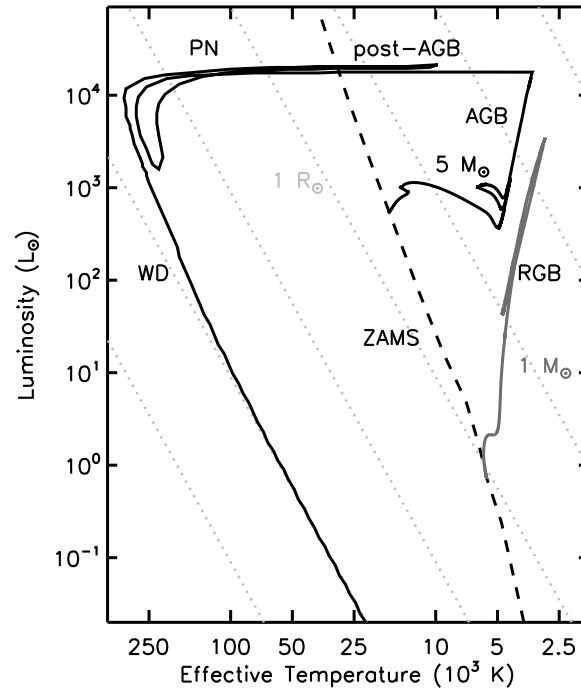


Figure 1.2: A Hertzsprung-Russel diagram showing the effective temperatures and luminosities of stars of two different masses ($1 M_{\odot}$ in grey and $5 M_{\odot}$ in black) at various stages of their life cycle. Here we use models for the evolution up to the end of the AGB from Cordier et al. (2007) and post-AGB evolution from Bloeker (1995a). The zero-age main sequence (ZAMS) for stars up to $15 M_{\odot}$ is indicated by the dashed line. The dotted grey lines indicate lines of constant radii in multiples of $10 R_{\odot}$ between 10^{-3} – $10^3 R_{\odot}$. The $5 M_{\odot}$ model shows a single late thermal pulse on the post-AGB, which causes its temperature to drop briefly.

of a star (which is related to its temperature since hot stars emit strongly at shorter wavelengths compared to cool stars) is plotted on the horizontal axis and magnitude (which is related to the luminosity) is on the vertical axis. In Figure 1.3, we show a CMD for the globular cluster M3 and note that the MS is truncated (it does not extend as high as the theoretical ZAMS in Figure 1.2). This is due to the significant age of the cluster (~ 10 Gyr) which means that many of the stars have evolved off the MS. This is the result of yet another consequence of different stellar masses, which is that stars with higher masses evolve faster.

Since fusion reactions in a star counteract its own self-gravitation, more massive stars require greater amounts of thermal pressure to support themselves against collapse. The result is that more massive stars have hotter cores and more efficient fusion reactions in their cores. They thus produce more energy in the same amount of time than their low mass counterparts. This is why stars with higher masses are closer to the top of the HR diagram on the MS. The

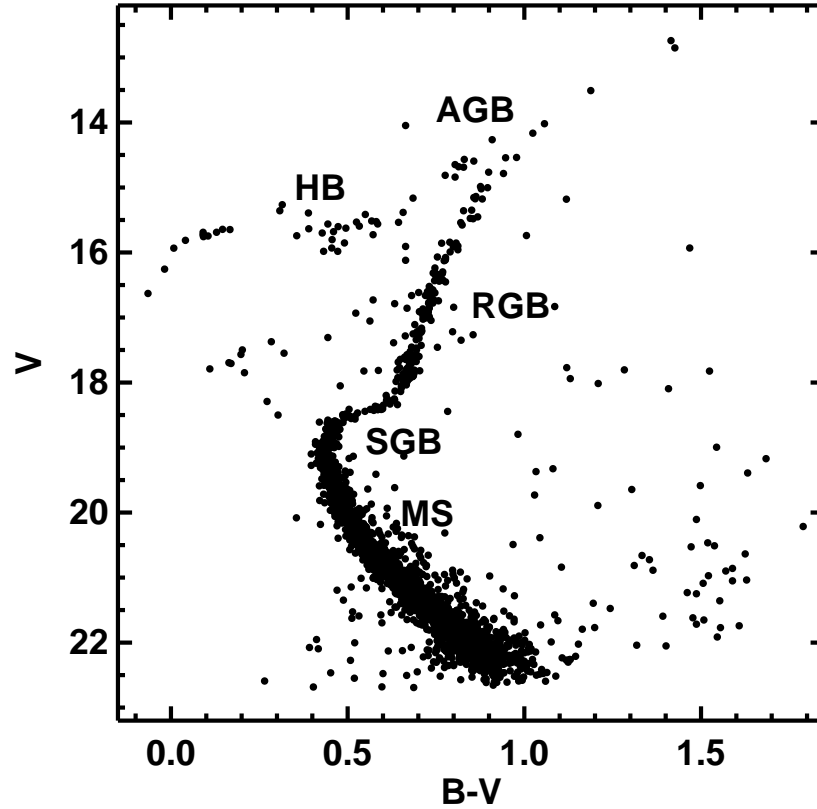


Figure 1.3: The colour magnitude diagram (CMD) of the globular cluster M3 based on data from Rey et al. (2001). The horizontal axis indicates the colour of the stars in the cluster while the vertical axis indicates their magnitude in the visible band. The stars on the right are coolest while the stars toward the top of the diagram are the brightest. The stars with lowest initial masses in the cluster remain on the main sequence (MS) while those with slightly higher masses are on the sub giant branch (SGB). The next most massive stars are on red giant branch (RGB), these are followed by the stars on the horizontal branch (HB) and finally, the asymptotic giant branch (AGB).

masses (M_{\star}) and luminosities (L_{\star}) of stars on the MS are related by the expressions:

$$\begin{aligned} L_{\star} &\propto M_{\star}^4 && \text{for } 0.43 M_{\odot} < M_{\star} < 2 M_{\odot} \\ L_{\star} &\propto M_{\star}^{3.5} && \text{for } 2 M_{\odot} < M_{\star} < 20 M_{\odot}. \end{aligned} \quad (1.1)$$

The energy generation in the core of a star on the MS depletes the core of hydrogen and enriches it with helium. This is what will cause the star to evolve and eventually leave the MS. The time a star spends on the MS thus depends both on its initial mass and its luminosity ($t_{\text{MS}} \approx M_{\star} L_{\star}^{-1}$).

From Equation 1.1, we can easily see that the low mass stars should remain on the MS much longer than the high mass stars. Indeed, while the Sun is expected to remain on the MS for roughly 10 Gyr, a star with an initial mass of $5 M_{\odot}$ is expected to have a $t_{\text{MS}} \approx 0.2$ Gyr and one with a mass of $20 M_{\odot}$ would have a $t_{\text{MS}} \approx 6$ Myr. This is why the MS in Figure 1.3 is truncated; only some of the low-mass stars remain on the MS while other low-mass and intermediate-mass stars appear in various stages of post-MS evolution.

While on the MS, the fusion of hydrogen in the core of a star into helium reduces the number of particles in the core. This decreases the thermal pressure, causing the core to contract. This contraction heats the core, which increases its rate of energy generation (since fusion processes are sensitive to temperature). In turn, this causes a slight increase in the luminosity of a star on the MS.

The contraction and heating of the core also heats the inner portion of the stellar envelope. As the star settles into a new equilibrium position, its envelope expands slightly due to the higher luminosity from the core. Thus, as a star evolves on the MS, it will burn slightly brighter and become slightly larger. As a result it moves up slightly in Figures 1.2 and 1.3 from its position on the ZAMS. In Figure 1.2, we see that on the MS, the $1 M_{\odot}$ model moves almost straight upward while the $5 M_{\odot}$ model moves up and to the right, as its effective temperature decreases as well. We also see this effect on the magnitudes of the stars in Figure 1.3 in the broadening of the MS.

1.1.3 Post-Main Sequence

As the core continues to contract and the hydrogen therein becomes more depleted, it continues to heat up and continues to heat the bottom of the stellar envelope. Eventually, the core is too enriched with helium to continue hydrogen fusion so the hydrogen burning continues in a shell surrounding the core. The hydrogen shell is hotter than the core was when it was fusing hydrogen and the shell has access to more hydrogen from the envelope. Thus the star burns material significantly faster and increases in luminosity.

The burning shell generates additional thermal pressure that pushes against both the stellar core and the envelope. This extra pressure from the shell burning causes the envelope to move outward, expanding to a large radius (on the order of 100 times larger than its MS radius) and cool (to $T_{\text{eff}} \approx 3000$ K) as the star settles into a new equilibrium state. The net result is that the luminosity of the star has increased significantly and the effective temperature has decreased, moving it onto the red giant branch (RGB; Iben, 1965). This branch appears in Figures 1.2 and 1.3 to the upper right of the MS. The envelope also becomes convective for all low- and intermediate-mass stars at this stage in its evolution due to the steep temperature

gradient created by the shell burning.

As the star evolves on the RGB, the hydrogen shell burning adds helium to the core, which increases its mass and it continues to contract and heat. This heats the hydrogen burning shell, which in turn causes it to generate even more energy, increasing its luminosity even more (e.g. a $1 M_{\odot}$ star will reach luminosities of over $1000 L_{\odot}$). In response, the stellar envelope expands further and the star is said to “ascend” the RGB.

As with the MS, the lifetime of a star on the RGB depends on its initial mass. For example, a $1 M_{\odot}$ star will stay on the RGB for ~ 1 Gyr and a $5 M_{\odot}$ star will stay on for ~ 0.5 Myr (Iben, 1967). In addition, *how* a star leaves the RGB will differ depending on the initial mass of the star.

As helium is added to the core of the star in low-mass stars, the density of the core increases to the point where it becomes degenerate. Thus, instead of being supported primarily by thermal pressure from collisions between particles, it is supported primarily by electron degeneracy pressure. This arises from the Pauli exclusion principle which prohibits two fermions (electrons, neutrons, protons) from occupying the same quantum state. We can see this in Figure 1.4 by following the evolutionary tracks of the 1 and $2 M_{\odot}$ stars where we note that these cross the line separating regions dominated by thermal and degeneracy pressure. While the core is degenerate, its pressure and temperature are only weakly dependent.

After the core has become degenerate, the hydrogen shell will continue to add mass to the core which continues to become hotter and denser. Eventually, it reaches the tip of the RGB (the most luminous point on the RGB in Figures 1.2 and 1.3). Then once its core has reached a mass of $0.45 M_{\odot}$ and a temperature of $\sim 10^8$ K, helium fusion begins in the core through the so-called triple- α process. This new source of fusion causes the temperature of the core to increase; however since the core is still degenerate, this is not accompanied by a corresponding increase in pressure so the core will not expand and cool as before. Since the triple- α process is extremely sensitive to pressure, helium fusion becomes increasingly efficient and the core continues to heat up. The result is runaway burning known as a *helium flash*.

The helium flash proceeds extremely rapidly until the core temperature has increased sufficiently to allow thermal pressure to dominate once again (Schwarzschild & Härm, 1962). When the core ceases to be degenerate, it begins to expand and cool and helium burning occurs in a quiescent manner as the star becomes a horizontal branch (HB) star. The hydrogen shell still remains active and it produces most of the energy for the star, but overall, the star produces less energy than it did at the tip of the RGB and its luminosity decreases. Its envelope contracts and heats up again so the star moves down and to the left on the CMD (see Figure 1.3). Some stars move to the so-called red clump—a region on the RGB of a similarly reduced luminosity—instead of the HB. Whether a star goes to the HB or the red clump depends on its

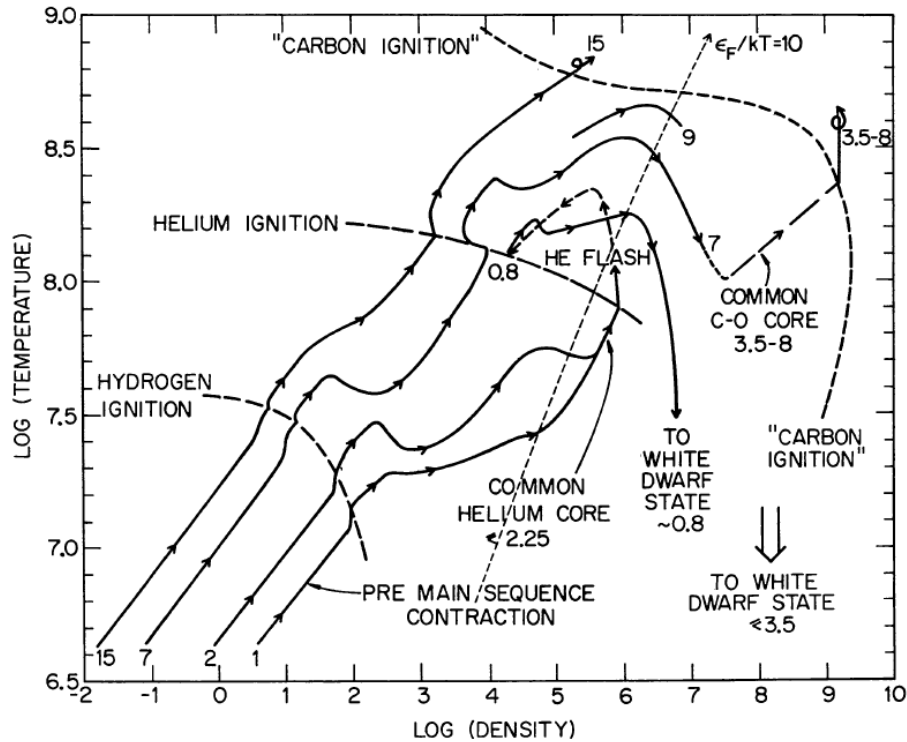


Figure 1.4: Densities and temperatures in the cores of stars with masses between 1 and 15 M_{\odot} (Iben, 1974). The evolution of stellar cores from stars of various masses are shown starting from the pre-main sequence. The dashed diagonal line distinguishes degeneracy from non-degeneracy, the characteristic thermal energy (i.e. this is the line between degeneracy on the right and non-degeneracy on the left).

metallicity and its mass loss history on the RGB (e.g. stars with low metallicities such as those found in globular clusters, or high mass-loss rates along the RGB evolve onto the HB), but they are essentially very similar states (Cannon, 1970).

Intermediate-mass stars do not develop degenerate cores on the RGB since their cores are hotter as a result of their higher masses (note that the 7 M_{\odot} core remains above the degeneracy line in Figure 1.4). Nor do they ascend to the tip of the RGB as low-mass stars do. Instead, they begin core helium fusion quiescently and migrate to the HB as soon as their cores reach temperatures of $\sim 10^8$ K.

The triple- α process fuses three helium nuclei (or α particles) into a carbon nucleus. An additional α particle may also fuse to the carbon nucleus creating oxygen. Through this process, the core becomes depleted of helium as it is replaced by carbon and oxygen.

The evolution of these stars during helium core burning is similar to their evolution on the MS; the cores contract as the number of particles in their core decrease which reduces

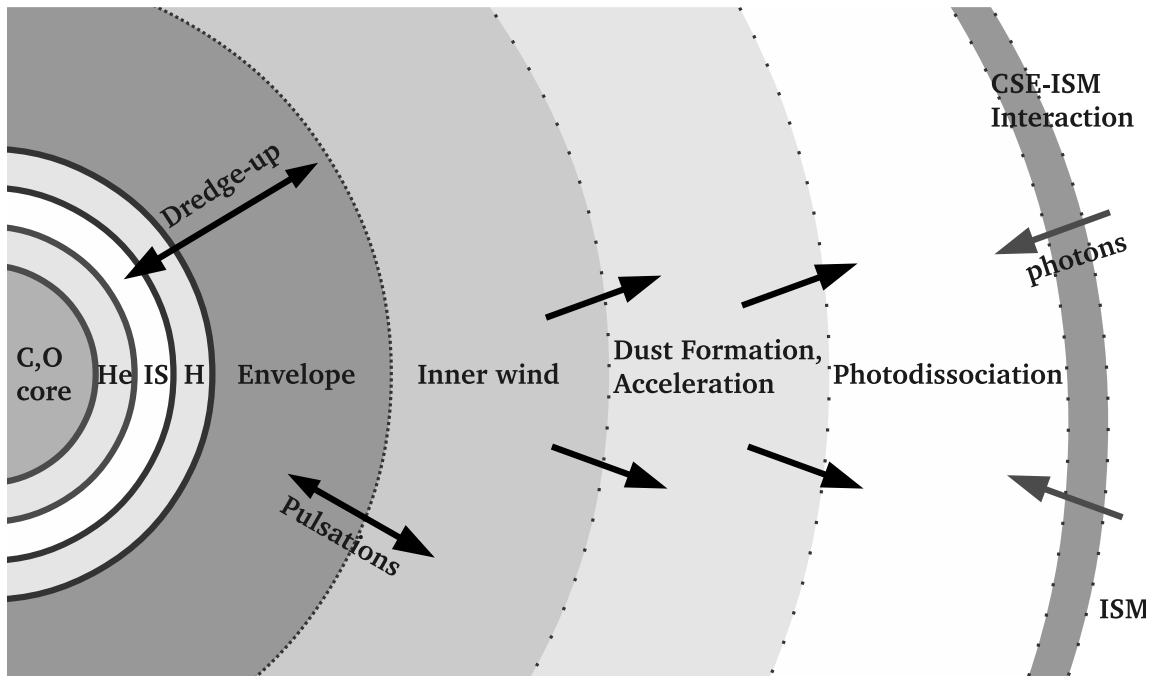


Figure 1.5: A schematic diagram of the structure of an AGB star and its CSE (not to scale). The innermost region of the star is its degenerate carbon and oxygen core. This is followed by the helium burning shell (He), then the intershell region (IS) and the hydrogen burning shell (H) and the large convective envelope. The approximate extent of the dredge-ups is also indicated. The CSE begins with the inner wind, which is affected by pulsations from the stellar photosphere, continuing into the dust acceleration zone and the photodissociation region where the photons from the ISM begin to interact with the CSE.

the thermal pressure. The core then contracts and heats up, which heats the layers above it. Eventually, the helium in the core is depleted and helium burning begins in a shell around the core. At this point, both low- and intermediate-mass stars have developed degenerate carbon and oxygen cores (see Figure 1.4).

With this new round of shell burning, low- and intermediate-mass stars settle into a new equilibrium state where their envelopes have once again expanded and cooled. These stars migrate onto the asymptotic giant branch (AGB), which lies just to the blue (hotter) side of the RGB on the HR diagram and CMD (see Figures 1.2 and 1.3). Stars which have just arrived on the AGB are sometimes referred to as early-AGB stars to contrast them with stars further along the AGB which are undergoing events known as thermal pulsations.

The structure of AGB stars is slightly more complicated than that of stars on the RGB, as illustrated in Figure 1.5. On the AGB, a star has an electron degenerate core composed of

carbon and oxygen. Immediately surrounding this core is a thin shell of burning helium which adds carbon and oxygen to the core. This is surrounded by an intershell region which is in turn surrounded by a shell of burning hydrogen, which adds helium to the intershell region. Finally, this shell is surrounded by an extended, cool ($R_{\star} \approx 1 \text{ AU}$ $T_{\text{eff}} \approx 3000 \text{ K}$), convective envelope.

On the early AGB, the hydrogen burning shell moves outward in mass as it consumes hydrogen until its temperature is too low and it is extinguished. The helium layer then provides the luminosity for the star, but it too moves outward in mass as it consumes helium and adds carbon and oxygen to the core. The helium burning shell becomes thinner and approaches the bottom of the hydrogen envelope. Eventually it heats the hydrogen envelope and re-ignites hydrogen shell burning.

As the helium burning shell becomes geometrically thin, it also becomes unstable. The results of this instability are periodic thermal runaways known as *thermal pulses*. During a thermal pulse, the energy produced in the helium shell increases significantly. This increases the temperature in the shell, which in turn causes the triple- α process to occur at a higher rate. Thus, the helium shell expands and pushes the envelope outward. This pushes the hydrogen shell burning to cooler regions of the envelope where it is effectively shut off. As the helium shell continues to expand, it cools, which decreases its luminosity, eventually causing it to cool and allowing the envelope to contract once more. As the envelope contracts, the hydrogen shell is heated and can resume burning. Once the first thermal pulse has occurred, the star is said to have begun the thermally pulsing AGB.

During each thermal pulse, as the hydrogen burning shell is nearly shut off, the convective envelope extends into the intershell region of a star (and sometimes into the helium burning shell), which is enriched with the products of nuclear burning (especially ^4He and ^{12}C). This deep convection brings these freshly created elements to the surface of the star and is known as a *dredge-up*. These events are important for the chemical composition of the stellar surface which is described in greater detail in Section 1.1.5. A thermal pulse is a repeating phenomenon which occurs every 10^4 to 10^5 years once they have been initiated (Iben & Renzini, 1983) and each one is accompanied by a dredge-up which further alters the chemical composition of the stellar envelope.

In the earlier stages of the stellar life cycle, the evolution of a star was determined by the amount of fuel and the rate at which this fuel is consumed in its interior. AGB stars, however, are characterized by rapid mass loss from the envelope which occurs at a higher rate than material is consumed by nuclear burning in its interior. Thus, it is this mass loss which primarily determines subsequent evolution.

The material lost by a star on the AGB forms a circumstellar environment (CSE). This is illustrated in Figure 1.5 where it extends from the top of the convective envelope to the ISM. It

is a relatively cool ($T < 3000$ K) region which is a formation site for molecules and dust grains (described further in Section 1.2).

The mass-loss rate increases toward the end of the AGB and stars typically experience what is known as a *superwind* phase, in which they eject the remaining stellar envelope in a very short amount of time at the end. When the envelope reaches a critical mass ($\sim 1\%$ of the original envelope mass), the star leaves the AGB and becomes either what is known as a post-AGB star or a pre-planetary nebula (pPN, sometimes called a proto-planetary nebula). At this point, the stellar wind changes from a slow, massive wind to a fast wind with a much lower mass-loss rate and the star evolves rapidly (10^4 – 10^5 yr; Vassiliadis & Wood, 1994) across the HR diagram as the degenerate core becomes increasingly exposed (see Figure 1.2).

Depending on the rate of its evolution across the HR diagram and the expansion rate of the CSE, the stellar core may ionize the material in the CSE and become a planetary nebula (PN) for some time. Then eventually, the material surrounding the core will dissipate and all that will remain of the star is a bare, degenerate core known as a white dwarf. All that remains for this white dwarf is a slow cooling period.

1.1.4 Nucleosynthesis

The fusion processes in stars not only provide energy to prevent gravitational collapse, but they also result in the formation of heavier elements. These nucleosynthesis products play a significant role in the chemistry of the CSE and ultimately result in the enrichment of the ISM (e.g. the outflows of AGB stars are one of the primary sources of carbon in our galaxy; Wallerstein & Knapp, 1998). Additionally, the end- and by-products of the various nuclear fusion reactions that occur over a stellar lifetime can be used to observationally test stellar evolution theories and determine the evolutionary status of individual objects.

Hydrogen burning

When stars burn hydrogen into helium, they do so via the pp chain and the CNO cycle. The overall efficiency of these reactions depends on the temperature of the burning region, which in turn depends on the stellar mass and the location of the hydrogen burning (e.g. in shell burning, the CNO cycle tends to dominate). Typically, in stars with initial masses less than $1.5 M_{\odot}$, the proton-proton chain is the dominant mechanism for proton fusion on the MS. The first pp chain (pp I) is relatively simple:



there are two other proton-proton branches which involve steps 1.2a and 1.2b followed by either the burning of lithium (in pp II) or beryllium and boron (in pp III). These latter reaction chains occur more frequently at higher temperatures, such as in higher mass MS stars and during shell burning, but they occur in small amounts in the Sun as well.

The CNO cycle also fuses protons into helium using ${}^{12}\text{C}$ as a catalyst for the reaction. This cycle can have interesting consequences for the abundances of carbon, nitrogen and oxygen in the stellar envelope which in turn reflects the chemical composition of the CSE, which we will see later has important effects on the chemistry in the CSE. The first CNO cycle is as follows:



The CNO cycle can also branch in two ways, resulting in the synthesis of different isotopes of nitrogen (${}^{15}\text{N}$) and oxygen (${}^{17}\text{O}$), however these reactions occur primarily at higher temperatures still.

Although ${}^{12}\text{C}$ acts as a catalyst for these reactions and reappears in the final step, the ${}^{14}\text{N}(p,\gamma){}^{15}\text{O}$ reaction¹ is slower than the other reactions in Equation 1.3, creating a bottleneck.

This results in a build up of ${}^{13}\text{C}$ and ${}^{14}\text{N}$ until the ${}^{12}\text{C}/{}^{13}\text{C}$ ratio reaches an equilibrium value of approximately 3.5, at which point ${}^{14}\text{N}$ will be the most abundant isotope in this cycle (Iben, 1964). Thus, some of the ${}^{12}\text{C}$ that begins in the CNO cycle will not complete the entire cycle. This is especially true for stars with lower masses and core temperatures (Weiss & Charbonnel, 2004). This change in isotopic ratio is observed on the surfaces of RGB stars as material from

¹This notation indicates the reactants and products of a nuclear reaction in a compact format. The reactants are on the left side of the comma and the products are on the right. Thus ${}^{14}\text{N}(p,\gamma){}^{15}\text{O}$ corresponds to reaction 1.3d. This notation will henceforth be used when discussing specific reactions in text.

the core is brought to the surface at the beginning of hydrogen shell burning (described further in Section 1.1.5).

Helium burning

When stars begin to fuse helium, they do so using the triple- α process, which is essentially:



The product of reaction 1.4a is unstable and decays on the order of 10^{-16} s. Thus, the triple- α process only occurs at high temperatures of at least $1\text{--}2 \times 10^8$ K when the rate of helium fusion is faster than the rate of ${}^8\text{Be}$ decay.

After helium is fused into carbon, it can undergo further reactions in what is known as the *alpha process*: ${}^{12}\text{C}(\alpha, \gamma){}^{16}\text{O}(\alpha, \gamma){}^{20}\text{Ne}(\alpha, \gamma){}^{24}\text{Mg}$. This process does not contribute significantly to the energy production in a star, though it will alter the abundances of these species. It is interesting to note that the rate of the first reaction in this series is notoriously uncertain (Fowler, 1984; Weaver & Woosley, 1993; Tang et al., 2010), which makes it difficult to ascertain an expected ${}^{12}\text{C}/{}^{16}\text{O}$ ratio.

s-process

In addition to the nuclear reactions that produce energy for a star, nucleosynthesis occurs through neutron capture on the AGB, in particular through the so-called s-process. The s-process is the *slow* capture of neutrons by seed nuclei. In this case, “slow” means that neutron capture timescales are longer than the timescales for beta decay. In other words, once a nucleus has captured a neutron, it will decay before it can capture another one. This differs from the r-process, where neutrons are captured faster than nuclei can decay. The high neutron flux required for the r-process is found in supernovae and leads to the formation of r-process elements such as platinum, germanium and xenon.

The s-process creates so-called s-process elements (e.g. strontium, barium, lead) and it was first discovered to occur in AGB stars with the observation of technetium (Tc, Merrill, 1952), the lightest element for which all isotopes are radioactive. Currently, AGB stars are considered the primary source of s-process elements in the galaxy (Busso et al., 1999). However, the details of how this process occurs are still not completely understood.

Hot Bottom Burning

Hot bottom burning (HBB) occurs in thermally pulsing AGB stars with masses above $5 M_{\odot}$. Here, the large convective envelopes extend to the tops of the hydrogen burning shells, so it is possible for some incomplete CNO cycle burning to occur at the bottom of the envelope. This depletes ^{12}C in the envelope and replaces it with ^{14}N due to the bottleneck reaction at $^{14}\text{N}(p,\gamma)^{15}\text{O}$.

1.1.5 Dredge-Ups

The products of nucleosynthesis in stellar interiors are transported to the surface by dredge-ups, which are events that occur when the convective envelope extends deep into the burning regions of a star. Since convection occurs when a steep temperature gradient is created, these typically occur around the onset of various forms of shell burning. By pulling freshly created material from fusion processes to the surface, dredge-ups alter the composition of stellar envelopes and photospheres.

There are up to three dredge-ups during the post-MS life of a low- and intermediate-mass star. The first dredge-up occurs at the beginning of the RGB. This material is primarily hydrogen, but it also contains the products of hydrogen burning. As discussed in Section 1.1.4, these include ^4He as well as ^{14}N and ^{13}C from partial CNO burning (Lattanzio & Boothroyd, 1997). This decreases the ratio of $^{12}\text{C}/^{13}\text{C}$ from ~ 90 on the MS to a value between 3 and 8 at the beginning of the RGB (Charbonnel, 1995; Sneden et al., 1986; Smith & Suntzeff, 1989).

The second dredge-up occurs in stars more massive than $4 M_{\odot}$ (Lattanzio & Boothroyd, 1997), when the helium core is exhausted at the end of the HB or red clump. This process once again changes the surface composition of ^{12}C , ^{13}C , ^{14}N and helium.

The third dredge-up is actually a series of events in which the mechanism and result are roughly the same each time. As mentioned in Section 1.1.3, a thermal pulse occurs with the runaway burning in the helium shell. A consequence of this event is the extinction of the hydrogen burning shell. This allows the convective envelope to penetrate deep into the intershell region (see Figure 1.5), and transport freshly created helium, carbon and oxygen to the surface. The number of third dredge-ups a star undergoes on the AGB depends (among other factors) on its initial mass, but each dredge-up event will alter the chemical composition of the stellar photosphere. As the star loses mass, the enriched material from the photosphere makes its way into the CSE.

1.1.6 From oxygen-rich AGB star to carbon star

Since the cosmic abundance of oxygen is greater than that of carbon, the photospheric abundances of stars initially contain more oxygen than carbon (giving them a carbon to oxygen ratio, $C/O < 1$). However, the value for photospheric C/O is changed by each subsequent third dredge-up event since these typically bring up more ^{12}C than ^{16}O . As we will describe further in Section 1.2, this ratio plays an important role in determining the chemical composition of the gas and dust in the CSE.

Stars typically begin the AGB with $C/O \sim 0.5$ and after a sufficient number of third dredge-up events, C/O will approach 1 (Smith & Lambert, 1990) and they become what are referred to as S-stars. When C/O becomes greater than 1, the star becomes a carbon (or C-) star (see Wallerstein & Knapp, 1998, for a review). Note that when AGB stars with $C/O < 1$ are discussed in this work they will be referred to as oxygen-rich to distinguish them from carbon and S-stars. In other works, they are sometimes referred to as M stars, which can be confusing since this can also refer to all stars with the spectral type M (including cool stars on the MS).

Stars with initial masses less than $1.5 M_{\odot}$ are not likely to become carbon stars (Smith & Lambert, 1990), as the mass they lose on the RGB and early on the AGB may cause them to evolve off the AGB before they experience sufficient third dredge-up events to reach $C/O > 1$. As a result, old clusters often do not show any carbon stars. In addition, stars more massive than $\sim 5 M_{\odot}$ are less likely to become carbon stars due to HBB which depletes the stellar envelope of carbon. However, some of these stars cease HBB toward the end of the AGB as they lose mass and may become carbon stars late in their lives.

Carbon stars are also more abundant when metallicity is low, as in the Small and Large Magellanic Clouds (SMC, LMC Blanco et al., 1980). Less carbon is required to make the C/O ratio greater than unity due to the lower metallicity of these galaxies, thus the star does not have to dredge up as much carbon to develop a photosphere with $C/O > 1$. In addition, third dredge-ups appear to operate more efficiently in stars with lower metallicities (Herwig, 2004; Karakas et al., 2002).

1.1.7 Mass Loss

Mass loss is the general name for those processes that remove material from the stellar surface. This can occur at any phase of stellar evolution (e.g. solar wind), but tends to be more pronounced for giants where the surface material is only loosely gravitationally bound to the star. This is especially true on the AGB, where mass loss rates range from $10^{-9} M_{\odot} \text{ yr}^{-1}$ (Omont et al., 1999) to $10^{-4} M_{\odot} \text{ yr}^{-1}$ (Lepine et al., 1995). While on the AGB, some stars will lose the majority of their initial masses, which we should expect since stars with masses up to $8\text{--}9 M_{\odot}$

end their lives as white dwarfs with masses of less than $1.4 M_{\odot}$, and typically closer to $0.6 M_{\odot}$.

Mechanisms

The mechanisms for such rapid mass loss among AGB stars are not entirely understood and a full discussion of all the work toward understanding this phenomenon is beyond the scope of the current work. Instead, we present a somewhat qualitative account of the processes that are considered to be important.

The mass loss process is thought to be initiated by stellar pulsations. We have observed that stars on the AGB are irregular—they vary in luminosity over time—and tend to pulsate—they expand and contract. Based on the regularity and amplitude of pulsations (measured by changes in the stellar magnitude as a function of time), stars can be divided into three main groups: L-type stars, semi-regular variables and Mira-variables. L-type stars have irregular light curves with little or no periodicity, while semi-regular variables exhibit some periodicity on the order of 30–1000 days with small variations in magnitude and Miras undergo large amplitude pulsations with periods longer than 100 days. As a star evolves along the AGB, it will evolve from irregular pulsations toward Mira-type pulsations and its mass loss rate will increase.

As an AGB star expands during a pulsation, its envelope is pushed outwards, away from the core. The outermost part of the stellar envelope will experience the greatest change in radius reaching heights of several stellar radii. This material eventually falls back toward the star; however, because the star continues to pulsate, the material falling inward will encounter material from the next pulse moving outward.

This phenomenon creates shocks—regions of enhanced density in the CSE—at several stellar radii above the photosphere (Höfner et al., 2003). At this distance, the temperature is sufficiently low that molecules will form and when the density is sufficiently high, dust will also form. Although there is much more gas than dust (typically the mass of gas is ~ 100 times the dust mass), radiation pressure from the central star is ineffective at pushing molecules, while it is very effective at pushing the dust grains away. Thus, once dust grains have formed, radiation pressure from the central star pushes them outward. The dust encounters gas molecules as it is pushed away, which causes the gas to couple with the dust, dragging it away from the star as well (Tielens, 1983; Wood, 1979).

Mass loss rates increase with the time a star has spent on the AGB (Willson, 2000; Iben & Renzini, 1983), ending in a superwind period where mass loss rates reach 10^{-5} to $10^{-4} M_{\odot} \text{ yr}^{-1}$. There are some semi-empirical mass loss laws (Bloeker, 1995b; Vassiliadis & Wood, 1993) which include this effect, although they have not been derived from first principles and the cause of this transition is the subject of much speculation (Wood, 2009; Bowen & Willson,

1991). It is possible, however, that the change is related to the onset of large pulsations (Mattsson et al., 2008).

Observations

Outflows from evolved stars were first observed by Adams & MacCormack (1935) who noted that the radial velocities of several sodium lines were shifted relative to the stellar radial velocities in several objects. However, mass loss was first conclusively observed in an evolved star by Deutsch (1956) who found an outflow from the circumbinary envelope of α Herculis which exceeded the escape velocity of the binary system. Since then, mass loss has been observed from many stars on the AGB.

Toward the end of the AGB, stars become enshrouded by dust, sometimes becoming invisible at optical wavelengths. Thus, objects are observed at longer wavelengths and the profiles of their molecular lines are often examined (Loup et al., 1993; Ramstedt et al., 2006; Decin et al., 2006; De Beck et al., 2012). These sorts of analyses can also provide insights in the mass loss histories of evolved objects. The examination of the dust emission in the mid-infrared can provide estimates for dust mass-loss rates (Groenewegen et al., 2007; Sloan et al., 2010).

In addition, there are photometric studies with high spatial resolution probing dust shells of evolved stars using scattered light including stars on the AGB (Leão et al., 2006; Maun et al., 2013) as well as (p)PNe (Sahai et al., 1998). Furthermore, by mapping cold dust in the far-infrared, it is possible to not only measure the early mass-loss history of evolved stars, but also observe the interaction between the CSE and ISM (Cox et al., 2012).

1.1.8 Evolution in Binary Systems

Thus far, we have described the evolution for low- and intermediate-mass evolution for single stars. However, many stars exist in binary systems and since the stars in such systems are likely to have different initial masses, they will evolve on different timescales. Thus, the more massive companion—known as the primary—will leave the MS and become a giant before the less massive companion—the secondary. If the stars are in a *close* binary system, the primary may transfer material to the secondary when it becomes a giant. The details of this mass transfer process are somewhat beyond the scope of this text, but we refer to Paczynski (1976); Taam & Sandquist (2000) for overviews.

The mass transfer from the primary to the secondary star has a number of implications on both stars and the evolution of the system as a whole. Indeed, this process can produce a number of interesting phenomena.

To begin with, as mass is transferred from the primary to the secondary, the orbital separation between the two stars decreases due to the conservation of angular momentum in the system. This accelerates the mass transfer and as a result, the primary will continue transferring material until after the secondary star has become more massive than the primary (or the primary ceases to be a giant). This results in binary systems where the more massive companion is on the MS and the less massive one is more evolved (e.g. Algol-type systems). If the primary star has experienced some third dredge-up events, this sort of transfer will also “pollute” the photosphere of the MS companion with s-process elements, resulting in a so-called barium (Ba) star (Han et al., 1995; McClure et al., 1980).

The exchange of material may also cause a star to terminate its evolution more rapidly due to its enhanced mass loss (Iben & Livio, 1993). This can mean an early termination of the AGB or in extreme cases, a star becomes a white dwarf immediately after the RGB. This sort of binary interaction is thought to be the cause of helium white dwarfs (low-mass white dwarfs composed of degenerate helium instead of carbon and oxygen, Althaus et al., 2010).

If mass transfer occurs after the primary has completed its evolution (and is a white dwarf) and the secondary has become a giant, this system will become a symbiotic system or a cataclysmic variable (Iben & Tutukov, 1996). These systems occasionally experience novae and are thought to be precursors to Type 1a supernovae.

Furthermore, there are some suggestions that PNe primarily form in stars with companions (de Marco, 2009; Moe & De Marco, 2006). This is thought to explain the wide variety in PNe morphologies since mass loss on the AGB is typically spherically symmetric while PNe are rarely so. While some studies indicate that binarity may be more common among PNe than among MS stars (e.g. De Marco et al., 2013), others do not agree with this assessment (e.g. Hrivnak et al., 2011).

In some cases, the stars may enter what is known as a *common envelope* period. In these systems, the mass transfer from the primary occurs more rapidly than the secondary can accrete the material, thus material from the primary surrounds both cores (Iben & Livio, 1993). When this occurs, the primary loses mass extremely rapidly and the orbital decay of the system is accelerated due to drag from the common envelope. In addition, the entire envelope can be ejected from the binary system entirely, forming a massive circumbinary disk. This is thought to have occurred for a class of peculiar evolved binaries; these objects have temperatures and luminosities which suggest they are in the post-AGB phase of their evolution, however their evolution is thought to be severely affected by the presence of a close binary companion (Van Winckel et al., 1995).

These stars typically show significant infrared excesses which suggest the presence of massive circumbinary disks. In addition, these unusual evolved binaries typically show unusual

photospheric abundances including extreme depletion in refractory elements and near-solar abundances for volatile elements (Takada-Hidai, 1990; Waelkens et al., 1991; Takeda et al., 2002). This unusual depletion pattern is thought to be the result of formation of dust in the circumbinary disk during periods of high mass loss and the subsequent re-accretion of “cleaned” gas onto the primary (Mathis & Lamers, 1992; Waters et al., 1992).

1.2 Circumstellar Environment

Although the material lost from the stellar surface eventually becomes part of the ISM, it will first spend time in the vicinity of the star as circumstellar matter. The fairly dense region between the photosphere and the interface with the ISM is called the circumstellar region, circumstellar envelope or circumstellar environment (CSE).

Different regions are often described in the CSE. The region of the CSE closest to the star is affected by stellar pulsations which cause regions of enhanced densities out to several stellar radii. Here, the high densities, cool temperatures and regular occurrences of shocks stimulate the formation of molecules. This region is occasionally referred to as the extended atmosphere, but in Figure 1.5, we refer to it as the inner wind.

At some point in the inner wind, temperatures are sufficiently low for some minerals to condense out and form dust grains. Radiation pressure on these dust grains will accelerate them outward and collisions with gas particles will cause the dust to grow and change composition through incorporating elements found in the gas. At the same time, the dust drags the gas along through the dust acceleration region (see Figure 1.5). When radiation pressure balances the drag, the dust has reached terminal velocity, typically between $10\text{--}20\text{ km s}^{-1}$ (Gustafsson & Höfner, 2004); this occurs within a few stellar radii of where dust formation begins. From here, the CSE is described by a constant-velocity dust-driven wind. Then, far from the star—where densities are low—interstellar radiation begins to penetrate the CSE triggering photochemistry. Finally, the CSE runs into the ISM, which often results in the formation of a bow shock (see e.g. Cox et al., 2012).

1.2.1 Carbon versus Oxygen-rich Chemistry

One of the first molecules to form in the photospheres of AGB stars is carbon monoxide (CO). Since CO is a very stable molecule due to the triple bond between carbon and oxygen, it is unlikely to dissociate once formed, thus all of either the carbon or oxygen (whichever is least abundant) which reaches the stellar photosphere can become trapped in CO. Since the material from the photosphere eventually makes its way into the CSE, the photospheric ratio of C/O in

the stellar atmosphere will largely determine the elements available for subsequent chemistry in the CSE.

As such, if $C/O < 1$, we would expect that all of the carbon will be locked away in CO, and if $C/O > 1$, all the oxygen will be kept in CO and unavailable for further chemistry. A completely different inventory of molecular species and dust minerals will result from this difference, as seen in Figure 1.6, where we compare the spectrum of one carbon star (RY Dra) to that of an oxygen-rich star (*o* Cet), Table 1.1, where we list a selection of the molecules observed in the CSEs of carbon- and oxygen-rich stars and Table 1.2, where we list a selection of dust minerals observed in these CSEs.

Oxygen-rich stars are often observed to show molecular features from e.g. OH, SiO, H₂O and will typically show oxide and silicate dust. Carbon stars, on the other hand show e.g. HCN, C₂H₂, C₃ and the dust typically constitutes silicon carbide (SiC), graphite and amorphous carbon. In the S-stars, there is often very little or no dust (since the carbon and oxygen have mostly been depleted, there is not much dust-forming material remaining). Where there is dust, it is typically oxygen-rich (Smolders et al., 2012). The molecules observed in these environments are typically diatomic (although emission from the polycyclic aromatic hydrocarbons, or PAHs, has been observed in some objects, Smolders et al., 2010).

Mixed-chemistry objects

There are some objects which show evidence of mixed carbon and oxygen chemistry. For instance, in Figure 1.6, in addition to *o* Cet and RY Dra, there is also the spectrum from an atypical J-type carbon star (V778 Cyg). In its spectrum, there is oxygen-rich dust and carbon-rich gas. This star is actually a binary star and in this system, the silicate dust is thought to be stored around the binary companion (a description of this system is given in Yamamura et al., 2000).

The peculiar evolved binaries often show mixed-chemistry environments as well including emission from both silicates or oxygen-rich gas and PAHs (e.g. Gielen et al., 2011; Cami & Yamamura, 2001).

1.2.2 Molecules

The number of molecular species which form in the photospheres of cool AGB stars is relatively small and typically limited to diatomic species (e.g. CO, TiO, LaO). However, many more—and often more complex—molecular species are observed to form in the CSE of AGB and post-AGB stars (see Table 1.1 for an incomplete list of observed molecular species).

This is especially true in the CSEs of carbon stars, as exemplified by the prototypical C-star

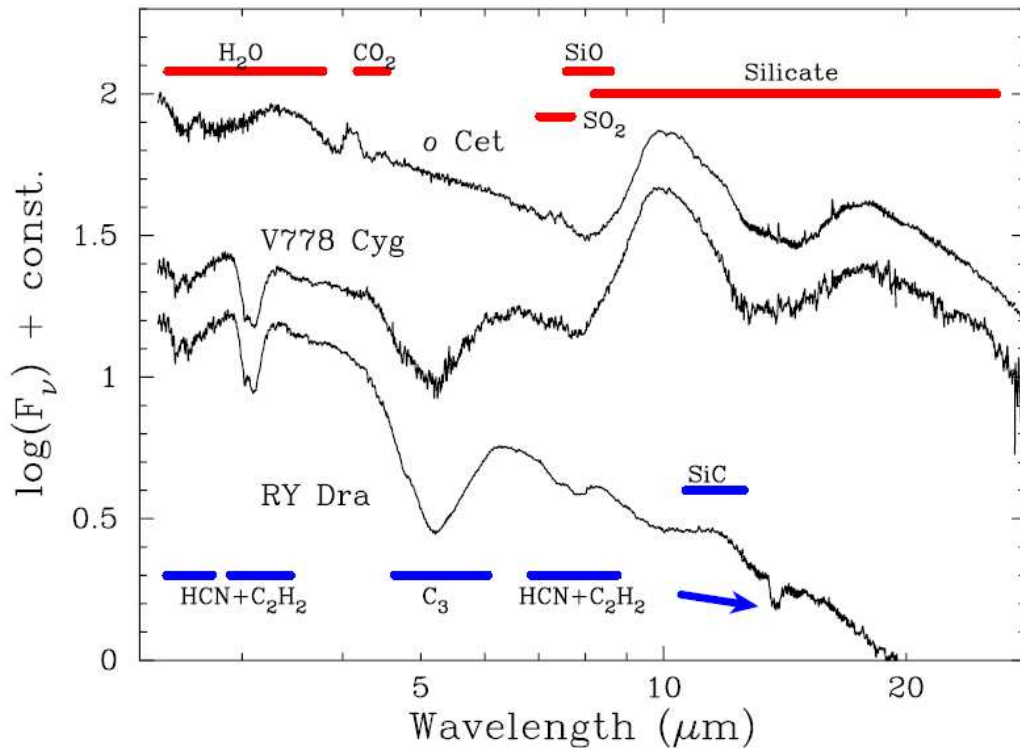


Figure 1.6: A comparison of the spectra from a typical O-rich star (*o* Cet), a typical C-star (RY Dra) and a so-called J-type star (V778 Cyg) from Yamamura et al. (2000).

IRC+10216 in which more than 60 molecular species have been identified (e.g. Cernicharo et al., 1996, 2010; Cordiner & Millar, 2009). Indeed, the outflows of C-rich AGB stars are observed to produce long carbon chains (polyynes and cyanopolyynes) which are precursors to more complex organic compounds such as the PAHs.

The chemistry in the CSEs of carbon stars becomes especially complex after a star has left the AGB when it is evolving as a post-AGB or pPN due to further processing which occurs in these environments. For instance in the CSE of pPNe, benzene (C_6H_6) has been detected (found in two pPNe thus far: CRL 618 and SMP LMC 11 Cernicharo et al., 2001; Bernard-Salas et al., 2006). Benzene is thought to be a bottleneck in the formation of the PAHs (Cherchneff et al., 1992), which are thought to form in the outflows of these stars (Latter, 1991; Frenklach & Feigelson, 1989). The PAHs are a family of large (average of ~ 50 carbon atoms Tielens, 2008), ubiquitous carbonaceous molecules in which up to 10–15% of all cosmic carbon is thought to be contained (Snow & Witt, 1995).

The exact formation mechanisms of benzene and PAHs in these environments is still uncertain. However, there are chemical models describing their formation including forming in circumstellar shocks (e.g. Cherchneff et al., 1992; Cherchneff, 2011) and through photochem-

Stellar chemistry	Molecules Detected			
O-rich	CO	OH	CN	SH
	CS	SiO	SiS	CO ₂
	SO	HCN	H ₂ O	NH ₃
	H ₂ S	HNC	SO ₂	PO [1]
	PN [1]			
C-star	CO	AlCl	AlF	CS
	CN	SiC	SiN	KCl
	SiO	SiS	CP	NaCl
	AlNC	MgCN	C ₂ H	HNC
	C ₂ S	HCN	H ₂ S	MgNC
	SiC ₂	SiCN	C ₃ N	NaCN
	C ₃ S	HC ₂ N	NH ₃	HC ₅ NC
	SiC ₃	C ₄ H	C ₄ Si	H ₂ C ₃
	C ₅ N	CH ₃ CN	H ₂ C ₄	C ₅ H
	C ₆ H	CH ₃ C ₂ H	HCO ⁺	SiH ₄
	C ₂ H ₂	C ₅	CH ₄	C ₂ H ₄
	C ₆ H ₆	H ₂ O	H ₂ CO [2]	C ₃ O [3]
	C ₆₀ [4]	C ₇₀ [4]		
	S-star	CO	SiS	SiO
HCN		ZrO	LaO	YO
SH		HCl	H ₂ O [5]	CO ₂ [5]

Table 1.1: A selection of molecules which have been detected in the CSE of AGB and post-AGB stars or (p)PNe. Table adapted from Olofsson (2004) except as indicated. [1] Tenenbaum et al. (2007) [2] Ford et al. (2004) [3] Tenenbaum et al. (2006) [4] Cami et al. (2010) [5] Smolders et al. (2012)

ical reactions (Woods et al., 2002, 2003).

Other large molecular species to form in these environments include the fullerenes, C₆₀ and C₇₀ which were first detected in the outflow of the young PN Tc 1, where these species were estimated to constitute ~3% of the available carbon (Cami et al., 2010). Since this first detection, C₆₀ has been detected in the outflows of other evolved stars, including post-AGB stars (Gielen et al., 2011; Roberts et al., 2012); additional PNe (García-Hernández et al., 2010, 2011a; Bernard-Salas et al., 2012; Otsuka et al., 2013) and R Coronae Borealis (RCB) stars (Clayton et al., 2011; García-Hernández et al., 2011b). It has also been detected in the ISM (Sellgren et al., 2010; Rubin et al., 2011) and young stellar objects (Roberts et al., 2012), which indicates that this molecule appears to survive the harsh conditions in the ISM as well.

As with the PAHs, there is still considerable debate regarding the formation mechanism for these species. While it is generally thought that fullerenes form in the CSEs of evolved carbon-

rich stars during the transition from the AGB to PN stage of their lives (Zhang & Kwok, 2011; Cami et al., 2010), three possible mechanisms have been suggested. They include formation in hydrogen-poor environments; the photochemical processing of hydrogenated amorphous carbon (HACs); and the destruction of PAHs at high temperatures.

The molecular inventory for O-rich CSEs does not typically contain such large species. Instead, the CSE of O-rich stars contain primarily diatomic molecules and only a few small polyatomic molecules, some of which were not anticipated in an O-rich CSE such as CO_2 (Cami et al., 2000; Ryde et al., 1999; Justtanont et al., 1998), SO_2 (Yamamura et al., 1999).

The strength of some of the molecular bands of these stars can sometimes indicate the C/O ratio in an AGB star. For instance, in O-rich stars where the C/O ratio is approaching unity, the TiO and H_2O bands will appear weaker, while the LaO and YO bands will remain approximately the same (Merrill, 1952).

For completeness, we also mention that some molecules (e.g. OH, H_2O , SiO) are observed to exhibit maser activity (van Loon et al., 2001).

Non-Equilibrium Chemistry In Table 1.1 we note that some carbon-containing molecules appear in oxygen-rich environments and vice versa. This is often due to the presence of non-equilibrium chemistry. This is expected to occur in the shocked regions several stellar radii above the photospheres in the inner winds of AGB stars. As a result, the relative abundances of carbon and oxygen appear to be less important; instead, these regions of the CSE often appear relatively similar regardless of the photospheric C/O (Decin et al., 2008; Cherchneff, 2006; Duari et al., 1999).

Furthermore, at large distances from the parent star, photons from the ISM begin to penetrate the CSE. This radiation can break up CO (especially ^{13}CO), which provides the CSE additional free carbon and oxygen atoms. Thus, the CSE of O-rich stars begin to show carbonaceous molecular species (e.g. Ziurys et al., 2009) or the CSE of C-stars can show oxygen bearing molecules (e.g. Tenenbaum et al., 2006; Ford et al., 2004).

1.2.3 Dust

The dust minerals expected to form in a given star are theoretically determined by dust condensation sequences (e.g. Tielens et al., 1998; Grossman & Larimer, 1974). These sequences describe how at different temperatures, various dust minerals nucleate and grow, at least if the densities are high enough. If the densities are too low for an intermediate step to occur, the reactions are said to *freeze out* at this step. The result is that the composition of the dust should depend on the mass loss rate, since the mass loss rates will determine the circumstellar

Stellar chemistry	Dust Species
O-rich	$\text{Mg}_{(1-x)}\text{Fe}_x\text{O}$
	Al_2O_3
	MgAl_2O_4
	Silicates (crystalline and amorphous)
	Crystalline water-ice
	Metallic iron
C-star	SiC
	MgS
	Amorphous carbon

Table 1.2: Here is a table with some of the dusts found in the CSE of AGB stars from Cami (2002); Blommaert et al. (2005).

densities.

There is some qualitative confirmation for these dust condensation sequences, but at the same time, they can only explain part of the observations. For example, some stars are dominated by oxide dust while others show copious amounts of silicates—the last step in that particular sequence. At the same time, some unexpected minerals have been detected (e.g. MgFeO) which were not predicted by these sequences.

Another issue which is not fully resolved is the presence of crystalline silicates. Silicates are thought to be formed above the so-called glass temperature and dust forming above this temperature should only exist in crystalline form. However, most of the silicates detected are amorphous. Large amounts of crystalline silicates are only found in the cool and dense CSE of OH/IR stars (tip-AGB stars without an optical component) or objects where a long-lived disk is present (e.g. Kemper et al., 2001; Molster et al., 1999).

1.3 Spectroscopic Analysis of CSEs

Evolved stars are very luminous and their CSEs are relatively cool and dusty. As a result, their spectral energy distributions (SEDs) peak in the infrared; they are thus best observed at infrared and longer wavelengths. For our purposes we are primarily interested in the near-infrared (0.75 to 5 μm) and mid-infrared (5 to 25 μm) spectral regions of these objects.

It is in these regions of the spectrum that we can observe features from warm ($T \approx 100 - 1000$ K) molecules. At these wavelengths, it is also possible to observe features and thermal radiation from dust. At longer wavelengths such as the far-infrared (25 to 350 μm) and sub-millimetre wavelength ranges, features from cool ($T < 100$ K) molecules are often observed

as well.

Molecular Spectroscopy

While atoms emit and absorb radiation through electronic transitions, molecules have two additional means of becoming (de-)excited upon absorbing or emitting radiation: through their rotational and vibrational modes. Molecules can be rotationally de-excited by emission of low-energy photons in the far-infrared and submillimetre wavelength ranges (the low energies for these transitions make them excellent probes of cold material). They can also emit near- and mid-infrared photons and become de-excited through vibrational transitions, which are accompanied by rotational transitions and often referred to as rovibrational transitions. Since photons of higher energies are required for these rovibrational transitions, these types of features are prominent in warmer gas.

Molecules vibrate in several types of so-called *normal vibrational modes*. These modes describe the motion of atoms within a molecule relative to each other. They include bending modes, where the angle between atoms changes; stretching modes, where the bond length between two atoms changes; rocking modes, where the angle between groups of atoms changes; twisting modes, where the plane between groups of atoms changes; and wagging modes, where the angle between the planes of different groups of atoms change.

These vibrational modes occur at characteristic energies particular to a given molecular species. These rovibrational transitions can appear as bands or individual lines (depending on the spacing of the lines and the resolving power of the instrument used to observe these transitions). Furthermore, they may form *combination bands* when two different vibrational modes interact. Together, these features serve as useful probes of the CSE.

Perhaps the most obvious use for molecular bands and lines is in the identification of molecular species present in these environments. This is possible because every molecule absorbs and emits energy at specific (and unique) wavelengths. Observing a number of molecular lines (or multiple molecular bands) thus makes it possible to determine which species are forming in these CSE.

In addition, the rotational lines within a rovibrational band are very sensitive to changes in temperature and column density. They are thus excellent probes of the physical conditions in the CSE. For instance, at different temperatures, the relative populations in different energy levels are different. At higher temperatures, higher rotational energy levels can be occupied, thus rovibrational transitions can occur to or from these higher rotational states. Furthermore, higher vibrational modes—which require even more energy to become excited than the rotational levels—are also more excited at higher temperatures. This too can have a noticeable effect on the spectrum as different vibrational bands become stronger depending on the temper-

ature. Thus, the appearance of the rovibrational bands of molecules can be used to determine the temperatures of their environments.

The column densities of molecular emitters can also be determined by the appearance of a molecular band. The higher the column density, the deeper the absorption (or the more flux in emission). However, high temperatures can also result in deeper absorption profiles (or stronger emission, as described further in Appendix A), so it is sometimes possible to confuse the effect of an increased temperature and an increased column density.

Determining the temperature and abundances of molecules in the CSE is useful for characterizing CSEs themselves, but arguably more importantly, a knowledge of the relative abundances is important for learning about the chemistry in these environments. When a full inventory of the molecular species in the outflow of an object is obtained, it can be compared to chemical models for those environments, providing important tests and constraints for these models.

Dust

For completeness, we mention that dust can also have spectral features in the infrared in addition to producing a thermal continuum. Dust particles have vibrational modes, but lack rotational structure within their vibrational bands. Different minerals will show different vibrational spectra in the infrared. However, there are many parameters (e.g. grain size, grain shape, impurities, temperature) which influence the spectral shapes and intensities in non-unique ways.

1.4 Open Problems

As we have described, low- and intermediate-mass stars play a significant role in the enrichment of the ISM through mass loss from their exteriors. Furthermore, the mass lost by stars on the AGB results in the formation of CSEs in which very interesting molecular and dust species are formed and processed. Although currently many of the general aspects of stellar evolution and the mass-loss processes which eventually return this material to the ISM are understood, there are still many problems left to solve.

Some of the most important problems in astrochemistry centre on the formation of large molecular species—such as PAHs and fullerenes—and dust grains in the CSE of evolved and carbon-rich stars. While we know that large molecules form in these environments, the chemical pathways involved are uncertain. In addition, the processes leading to dust formation and how the dust is processed in these environments are also uncertain.

Another significant issue is the effect of a binary companion on the evolution of low- and intermediate-mass stars in particular. While some work has been done on the high-mass stars in binary systems as well as in modeling extreme end states of low-mass stars such as the helium white dwarfs, there has not been much work done toward understanding what occurs in the less extreme cases of mass transfer in low-mass stars.

1.5 This Thesis

In this thesis, we focus primarily on a few issues surrounding the CSE chemistry including the processing of material in long-lived disks and on the impact of a binary companion on stellar evolution. In particular, we focus on two unusual evolved objects, the carbon-rich pPN SMP LMC 11 and the evolved binary HR 4049.

We primarily rely on data from the *Spitzer* Space Telescope (Werner et al., 2004). Thus, we begin with an overview of the data reduction steps we take before we can begin our analysis of the data in Chapter 2.

Next, in Chapter 3, we analyze the mid-infrared spectrum of SMP LMC 11. This spectrum is especially rich in molecular features, showing deep and broad absorption from C_2H_2 and a variety of other carbonaceous compounds, including C_6H_6 . We find that the gas in this environment is warm and dense and suggest that it may be located in a torus rather than a spherical outflow. Furthermore, a detailed comparison of our results to chemical models in these environments shows that the chemistry in this CSE is very different from the model predictions. We suggest that this may be the result of missing chemical pathways in these models.

In Chapter 4, we examine the mid-infrared spectrum of the evolved binary HR 4049. We find that the gas, which resides in a massive ($M_{\text{disk}} \gtrsim 8 \times 10^{-3} M_{\odot}$) circumbinary disk is warm and dense. Furthermore, there is evidence for the ongoing processing of the dust in the disk in the significant increase in CO_2 emission we observe between the observations from the Short Wavelength Spectrometer on board the Infrared Space Observatory (ISO-SWS) and those by *Spitzer*-IRS. We also find that these results are consistent with a radially extended disk. Finally, we suggest that the high optical depths of the gas in the system not only trap stellar radiation, warming the disk, but that this gas may also contribute significantly to the SED of the disk.

Our final project, described in Chapter 5, focuses on the high-resolution near-infrared spectrum of HR 4049. Here, we analyze the CO and H_2O absorption at $2.3 \mu\text{m}$ as well as the combined emission-absorption spectrum of these species at $4.6 \mu\text{m}$. We also perform a kinematical analysis of the gas, and find that these observations are consistent with a radially extended disk, in agreement with the mid-infrared observations. We also determine that the gas in the disk is

warm and may extend beyond the disk toward the binary system, which causes the significant emission at $4.6 \mu\text{m}$. We also find evidence for a much colder component of gas in the disk, which may exist in the bipolar lobes.

Finally, we summarize the conclusions from these projects and describe future work which could be done to further our understanding of the processes occurring in these systems in Chapter 6.

The analyses of these data also involve significant modelling of the spectral features. We thus describe the synthesis of model spectra from line lists as well as the statistical methods we employ to compare these models to our data in Appendix A.

Bibliography

- Adams W.S., MacCormack E., 1935, *Contributions from the Mount Wilson Observatory / Carnegie Institution of Washington* 505, 1
- Althaus L.G., Córscico A.H., Isern J., García-Berro E., 2010, *Astron. Astrophys. Rev.* 18, 471
- Bernard-Salas J., Cami J., Peeters E., et al., 2012, *ApJ* 757, 41
- Bernard-Salas J., Peeters E., Sloan G.C., et al., 2006, *ApJL* 652, L29
- Blanco V.M., Blanco B.M., McCarthy M.F., 1980, *ApJ* 242, 938
- Bloecker T., 1995a, *A&A* 299, 755
- Bloecker T., 1995b, *A&A* 297, 727
- Blommaert J.A.D.L., Cami J., Szczerba R., Barlow M.J., 2005, *Space Science Reviews* 119, 215
- Bowen G.H., Willson L.A., 1991, *ApJL* 375, L53
- Busso M., Gallino R., Wasserburg G.J., 1999, *ARA&A* 37, 239
- Cami J., 2002, Molecular gas and dust around evolved stars. Ph.D. thesis, AA(University of Amsterdam)
- Cami J., Bernard-Salas J., Peeters E., Malek S.E., 2010, *Science* 329, 1180
- Cami J., Yamamura I., 2001, *A&A* 367, L1
- Cami J., Yamamura I., de Jong T., et al., 2000, *A&A* 360, 562
- Cannon R.D., 1970, *MNRAS* 150, 111
- Cernicharo J., Barlow M.J., Gonzalez-Alfonso E., et al., 1996, *A&A* 315, L201
- Cernicharo J., Decin L., Barlow M.J., et al., 2010, *A&A* 518, L136, printed:in IRC+10216 category
- Cernicharo J., Heras A.M., Tielens A.G.G.M., et al., 2001, *ApJL* 546, L123, printed: category CRL 618

- Charbonnel C., 1995, *ApJL* 453, L41
- Cherchneff I., 2006, *A&A* 456, 1001
- Cherchneff I., 2011, *A&A* 526, L11
- Cherchneff I., Barker J.R., Tielens A.G.G.M., 1992, *ApJ* 401, 269
- Clayton G.C., De Marco O., Whitney B.A., et al., 2011, *AJ* 142, 54
- Cordier D., Pietrinferni A., Cassisi S., Salaris M., 2007, *AJ* 133, 468
- Cordiner M.A., Millar T.J., 2009, *ApJ* 697, 68
- Cox N.L.J., Kerschbaum F., van Marle A.J., et al., 2012, *A&A* 537, A35
- De Beck E., Lombaert R., Agúndez M., et al., 2012, *A&A* 539, A108
- de Marco O., 2009, *PASP* 121, 316
- De Marco O., Passy J.C., Frew D.J., Moe M., Jacoby G.H., 2013, *MNRAS* 428, 2118
- Decin L., Cherchneff I., Hony S., et al., 2008, *A&A* 480, 431
- Decin L., Hony S., de Koter A., et al., 2006, *A&A* 456, 549
- Deutsch A.J., 1956, *ApJ* 123, 210
- Duari D., Cherchneff I., Willacy K., 1999, *A&A* 341, L47
- Ford K.E.S., Neufeld D.A., Schilke P., Melnick G.J., 2004, *ApJ* 614, 990
- Fowler W.A., 1984, *Reviews of Modern Physics* 56, 149
- Frenklach M., Feigelson E.D., 1989, *ApJ* 341, 372
- García-Hernández D.A., Iglesias-Groth S., Acosta-Pulido J.A., et al., 2011a, *ApJL* 737, L30
- García-Hernández D.A., Kameswara Rao N., Lambert D.L., 2011b, *ApJ* 739, 37
- García-Hernández D.A., Manchado A., García-Lario P., et al., 2010, *ApJL* 724, L39
- Gielen C., Cami J., Bouwman J., Peeters E., Min M., 2011, *A&A* 536, A54
- Gilden D.L., 1984, *ApJ* 283, 679
- Groenewegen M.A.T., Wood P.R., Sloan G.C., et al., 2007, *MNRAS* 376, 313
- Grossman L., Larimer J.W., 1974, *Reviews of Geophysics and Space Physics* 12, 71
- Gustafsson B., Höfner S., 2004, *Asymptotic Giant Branch Stars*, chap. Atmospheres of AGB Stars, pp. 149–245. Springer-Verlag

- Han Z., Eggleton P.P., Podsiadlowski P., Tout C.A., 1995, *MNRAS* 277, 1443
- Herwig F., 2004, *ApJ* 605, 425
- Höfner S., Gautschy-Loidl R., Aringer B., Jørgensen U.G., 2003, *A&A* 399, 589
- Hrivnak B.J., Lu W., Bohlender D., et al., 2011, *ApJ* 734, 25
- Iben, Jr. I., 1974, *ARA&A* 12, 215
- Iben, Jr. I., Livio M., 1993, *PASP* 105, 1373
- Iben, Jr. I., Renzini A., 1983, *ARA&A* 21, 271
- Iben, Jr. I., Tutukov A.V., 1996, *ApJS* 105, 145
- Iben I.J., 1964, *ApJ* 140, 1631
- Iben I.J., 1965, *ApJ* 142, 1447
- Iben I.J., 1967, *ARA&A* 5, 571
- Justtanont K., Feuchtgruber H., de Jong T., et al., 1998, *A&A* 330, L17
- Karakas A.I., Lattanzio J.C., Pols O.R., 2002, *Publications of the Astron. Soc. of Australia* 19, 515
- Kemper F., Waters L.B.F.M., de Koter A., Tielens A.G.G.M., 2001, *A&A* 369, 132
- Larson R.B., 2003, *Reports on Progress in Physics* 66, 1651
- Lattanzio J.C., Boothroyd A.I., 1997, In: E. K. Zinner & T. J. Bernatowicz (ed.), *American Institute of Physics Conference Series*, vol. 402 of *American Institute of Physics Conference Series*, pp. 85–114
- Latter W.B., 1991, *ApJ* 377, 187
- Leão I.C., de Laverny P., Mékarnia D., de Medeiros J.R., Vandame B., 2006, *A&A* 455, 187
- Lepine J.R.D., Ortiz R., Epchtein N., 1995, *A&A* 299, 453
- Loup C., Forveille T., Omont A., Paul J.F., 1993, *A&AS* 99, 291
- Mathis J.S., Lamers H.J.G.L.M., 1992, *A&A* 259, L39
- Mattsson L., Wahlin R., Höfner S., Eriksson K., 2008, *A&A* 484, L5
- Mauron N., Huggins P.J., Cheung C.L., 2013, *A&A* 551, A110
- McClure R.D., Fletcher J.M., Nemeč J.M., 1980, *ApJL* 238, L35
- Merrill S.P.W., 1952, *ApJ* 116, 21

- Moe M., De Marco O., 2006, *ApJ* 650, 916
- Molster F.J., Yamamura I., Waters L.B.F.M., et al., 1999, *Nature* 401, 563
- Olofsson H., 2004, Asymptotic Giant Branch Stars, chap. Circumstellar Envelopes, pp. 325–410. Springer-Verlag
- Omont A., Ganesh S., Alard C., et al., 1999, *A&A* 348, 755
- Otsuka M., Kemper F., Hyung S., et al., 2013, *ApJ* 764, 77
- Paczynski B., 1976 73, 75
- Ramstedt S., Schöier F.L., Olofsson H., Lundgren A.A., 2006, *A&A* 454, L103
- Rey S.C., Yoon S.J., Lee Y.W., Chaboyer B., Sarajedini A., 2001, *AJ* 122, 3219
- Roberts K.R.G., Smith K.T., Sarre P.J., 2012, *MNRAS* 421, 3277
- Rubin R.H., Simpson J.P., O'Dell C.R., et al., 2011, *MNRAS* 410, 1320
- Ryde N., Eriksson K., Gustafsson B., 1999, *A&A* 341, 579
- Sahai R., Trauger J.T., Watson A.M., et al., 1998, *ApJ* 493, 301
- Schwarzschild M., Härm R., 1962, *ApJ* 136, 158
- Sellgren K., Werner M.W., Ingalls J.G., et al., 2010, *ApJL* 722, L54
- Sloan G.C., Matsunaga N., Matsuura M., et al., 2010, *ApJ* 719, 1274
- Smith V.V., Lambert D.L., 1990, *ApJS* 72, 387
- Smith V.V., Suntzeff N.B., 1989, *AJ* 97, 1699
- Smolders K., Acke B., Verhoelst T., et al., 2010, *A&A* 514, L1
- Smolders K., Neyskens P., Blommaert J.A.D.L., et al., 2012, *A&A* 540, A72
- Snedden C., Pilachowski C.A., Vandenberg D.A., 1986, *ApJ* 311, 826
- Snow T.P., Witt A.N., 1995, *Science* 270, 1455
- Stahler S., Palla F., 2004, *The Formation of Stars*. Wiley-VCH
- Taam R.E., Sandquist E.L., 2000, *ARA&A* 38, 113
- Takada-Hidai M., 1990, *PASP* 102, 139
- Takeda Y., Parthasarathy M., Aoki W., et al., 2002, *PASJ* 54, 765
- Tang X.D., Rehm K.E., Ahmad I., et al., 2010, *Phys. Rev. C* 81, 045809

- Tenenbaum E.D., Apponi A.J., Ziurys L.M., et al., 2006, *ApJL* 649, L17
- Tenenbaum E.D., Woolf N.J., Ziurys L.M., 2007, *ApJL* 666, L29
- Tielens A.G.G.M., 1983, *ApJ* 271, 702
- Tielens A.G.G.M., 2008, *ARA&A* 46, 289
- Tielens A.G.G.M., Waters L.B.F.M., Molster F.J., Justtanont K., 1998, *Ap&SS* 255, 415
- van Loon J.T., Zijlstra A.A., Bujarrabal V., Nyman L.Å., 2001, *A&A* 368, 950
- Van Winckel H., Waelkens C., Waters L.B.F.M., 1995, *A&A* 293, L25
- Vassiliadis E., Wood P.R., 1993, *ApJ* 413, 641
- Vassiliadis E., Wood P.R., 1994, *ApJS* 92, 125
- Waelkens C., Van Winckel H., Bogaert E., Trams N.R., 1991, *A&A* 251, 495
- Wallerstein G., Knapp G.R., 1998, *ARA&A* 36, 369
- Waters L.B.F.M., Trams N.R., Waelkens C., 1992, *A&A* 262, L37
- Weaver T.A., Woosley S.E., 1993, *Phys. Rep.* 227, 65
- Weiss A., Charbonnel C., 2004, *Memorie della Societa Astronomica Italiana* 75, 347
- Werner M.W., Roellig T.L., Low F.J., et al., 2004, *ApJS* 154, 1
- Willson L.A., 2000, *ARA&A* 38, 573
- Wood P.R., 1979, *ApJ* 227, 220
- Wood P.R., 2009, In: S. J. Murphy & M. S. Bessell (ed.), *Astronomical Society of the Pacific Conference Series*, vol. 404 of *Astronomical Society of the Pacific Conference Series*, pp. 255–261
- Woods P.M., Millar T.J., Herbst E., Zijlstra A.A., 2003, *A&A* 402, 189
- Woods P.M., Millar T.J., Zijlstra A.A., Herbst E., 2002, *ApJL* 574, L167
- Woosley S.E., Heger A., Weaver T.A., 2002, *Rev. Mod. Phys.* 74, 1015
- Woosley S.E., Weaver T.A., 1986, *ARA&A* 24, 205
- Yamamura I., de Jong T., Onaka T., Cami J., Waters L.B.F.M., 1999, *A&A* 341, L9
- Yamamura I., Dominik C., de Jong T., Waters L.B.F.M., Molster F.J., 2000, *A&A* 363, 629
- Zhang Y., Kwok S., 2011, *ApJ* 730, 126
- Ziurys L.M., Tenenbaum E.D., Pulliam R.L., Woolf N.J., Milam S.N., 2009, *ApJ* 695, 1604

It faut bien s'arrêter quelque part,
et pour que la science soit possible,
il faut s'arrêter quand on a trouvé
la simplicité.

Henri Poincaré

Chapter 2

Spitzer data reduction

Much of the work in this thesis involves infrared spectra from the Infrared Spectrograph (IRS Houck et al., 2004) on board the *Spitzer* Space Telescope (Werner et al., 2004). While we describe the data reduction process very broadly in the relevant research chapters of this thesis (Chapters 3 and 4), we consider it useful to provide further details of the data reduction process.

Here, we begin by briefly describing the IRS and how observations are carried out in Section 2.1. Then we describe how we obtain a rough spectrum using SMART (Higdon et al., 2004; Lebouteiller et al., 2010) in Section 2.2. Finally, we describe how we polish these rough spectra and prepare them for further analysis in Section 2.3.

2.1 Spitzer-IRS Observations

The IRS has four observing modules, two have high spectral resolution ($R = \lambda/\Delta\lambda = 600$), the short high (SH) and long high (LH) and two with low spectral resolution ($R \approx 60 - 130$), the short low (SL) and long low (LL). We provide a summary of the spectral resolution and wavelength coverage for each of the observing modes in Table 2.1.¹ There are also two imaging arrays on the SL detector, blue (13.3 to 18.7 μm) and red (18.5 to 26.0 μm), which can be used to help point the telescope with greater accuracy.

The low resolution modules are both grating spectrographs each divided into two orders (SL1 from 7.4 to 14.5 μm and SL2: 5.2 to 7.7 μm ; LL1 from 19.5 to 38.0 μm and LL2 from 14.0 to 21.3 μm), while the high resolution modules are cross-dispersed échelle spectrographs each with 9 orders numbered 11 (at the long wavelength end) to 20 (at the short wavelength end). In the high resolution modules, all orders observe the source simultaneously, while the low resolution modes have one order on the source while the other observes an offset position.

¹The interested reader may also refer to the IRS Instrument Handbook available at <http://irsa.ipac.caltech.edu/data/SPITZER/docs/irs/irsinstrumenthandbook/> for further details.

Mode	Resolution	Wavelength range (μm)
SL	60 to 127	5.2 to 14.5
LL	57 to 126	14.0 to 38.0
SH	600	9.9 to 19.6
LH		18.7 to 37.2

Table 2.1: The names, resolutions and wavelength ranges for the observing modes of Spitzer-IRS.

The Spitzer-IRS observations used in this thesis all use the staring mode astronomical observing template (AOT). In this mode, the object is placed 1/3 and 2/3 of the way along the length of the slit and the telescope nods between these positions. This increases the signal-to-noise (S/N) ratio by taking multiple observations and reduces issues due to cosmic rays or bad pixels on the detector. Each of these nods constitutes a single data collection event (DCE). In a single astronomical observation request (AOR) there are typically three pairs of DCEs, although for SMP LMC 11 (described in Chapter 3) which was observed as part of a Guaranteed Time Observer (GTO) program, there was only one for the high resolution observations.

Often, background observations are taken as well by observing a local off-source position around the same time that the on-source observations are obtained. For point sources observed with the high-resolution modules, additional observations are required to obtain a background observation. For point sources observed with the low-resolution modules, background observations are taken automatically by the off-source position as well as the part of the on-source order which is not filled by the source. Subtracting this background can remove spectral features due to materials which are along the line of sight to the object, but not associated with the object itself (e.g. interstellar dust). When the background is featureless, subtracting the background can also increase the S/N by removing rogue pixels—pixels which are anomalously bright either by having a high dark current or photon responsivity.

After the data has been collected and before it gets to the user, it is processed through the pipeline. Here, the raw FITS files are turned into basic calibrated data (bcd). This process includes estimating the uncertainties on each pixel, converting the data numbers to electrons, flagging cosmic ray events, correcting the pixels for saturation, subtracting the dark current, correcting for linear response in the detectors. In addition, the velocity of the spacecraft during the observations is calculated and the header for the bcd FITS files are generated with this information.

2.2 Using SMART

To reduce spectra from Spitzer-IRS, we use the Spectral Modeling Analysis and Reduction Tool, SMART (Higdon et al., 2004; Lebouteiller et al., 2010). We begin by creating a project and adding the bcds we have for our object in the window.

The first step we take in reducing spectra from Spitzer-IRS is cleaning the bcds using `IRSCLEAN`. This removes rogue pixels from the data.

Rogue pixels can also be removed through background subtraction since they are instrumental features, though they are time-dependent on long timescales. However, in the absence of background observations or in the case where background subtraction alone does not remove all of the rogue pixels from the data, then cleaning the data is a necessary step. For our observations, we used the campaign rogue pixel masks and cleaned all the data.

Once we have cleaned all the bcds, we combine the bcds from each DCE using an automatic procedure which takes a weighted mean for each pixel. At this point if we have background observations, we subtract those from the combined DCEs.

Then we extract the spectrum. For the high resolution data, we do this using the full aperture extraction since we are looking at point sources. For the low resolution data, we use the optimal extraction plugin (AdOpt, Lebouteiller et al., 2010). The optimal extraction plugin detects the sources in the data then determines the point spread function (PSF) for each source. It also defines the background and can subtract it from the spectrum automatically.

Once we have a spectrum for each nod position which appears reasonable, we export the spectra and continue our analysis with custom IDL routines.

2.3 Custom Routines

When we have completed all the steps using SMART, we have something that looks like what we see in Figure 2.1. Here, there are not only large amounts of noise at the edges of the orders, but we note that there are also mismatches between the fluxes of each order.

There may also be fringes in the data. These sometimes arise in bright sources and can be an issue, especially in the high resolution and LL modes (the fringes in SL are not spectrally resolved). To remove fringes, we use the `IRSFRINGE` function. We typically set a few different tolerance levels in `IRSFRINGE` and compare our defringed versions of the spectrum to each other as well as the original spectrum and we also compare the nod positions to each other. If the results seem reasonable (e.g. the fringes appear to be removed, but the spectral features are not), then we proceed to the next steps.

To correct for the noisy order edges and flux jumps between the orders, we begin by care-

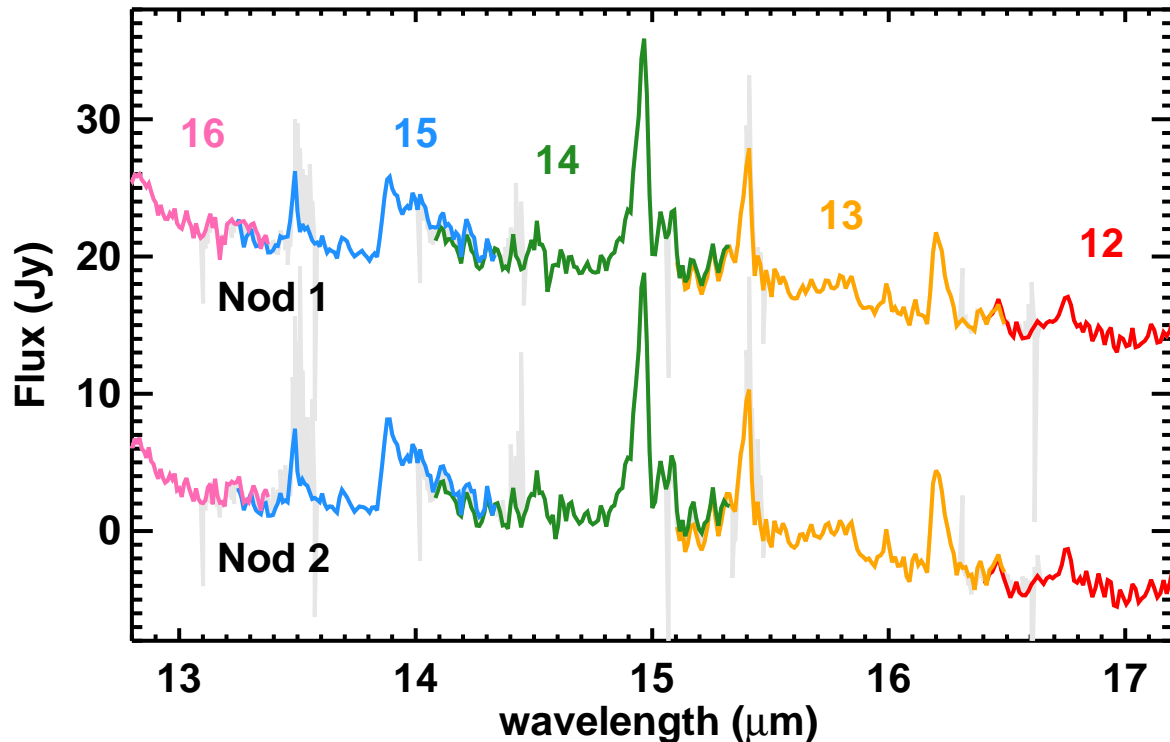


Figure 2.1: A portion of the rough SH spectrum of HR 4049 with both nod positions. The entire raw spectrum for each nod is shown in gray. The portions of the spectrum we would keep from each order are represented by a different colour and labelled according to their order number. Here, Nod 2 is offset by 20 Jy below its actual flux for clarity.

fully comparing the regions of the spectrum where two orders overlap (or “overlap regions”). For parts of these overlap regions, the spectral features appear to be very similar, but toward the very edges of the orders, they become extremely noisy. We trim each order by defining where they become noisy then removing these regions.

Once we have removed the noisy regions from the edge of each order, we begin to scale all the orders to remove the flux jumps between them. For the high resolution orders, we pick one of the orders on the end (either order 11 or 20). Here, the choice of which order to scale to is entirely arbitrary, but we tend to select whichever results in the least scaling.

To scale the orders, we compare the overlap region and calculate the median flux for each order in that region and define a scaling factor so they match. For example, if we are comparing the overlap region between orders 11 and 12 and we find median values of f_{11} and f_{12} for the flux in each overlap region, we will scale order 12 by multiplying it with the scaling factor $F_{11/12} = f_{11}f_{12}^{-1}$. Once we have scaled the flux of order 12 to match the edge of order 11, we move on to match the flux of order 13 to that of the scaled order 12 and so on.

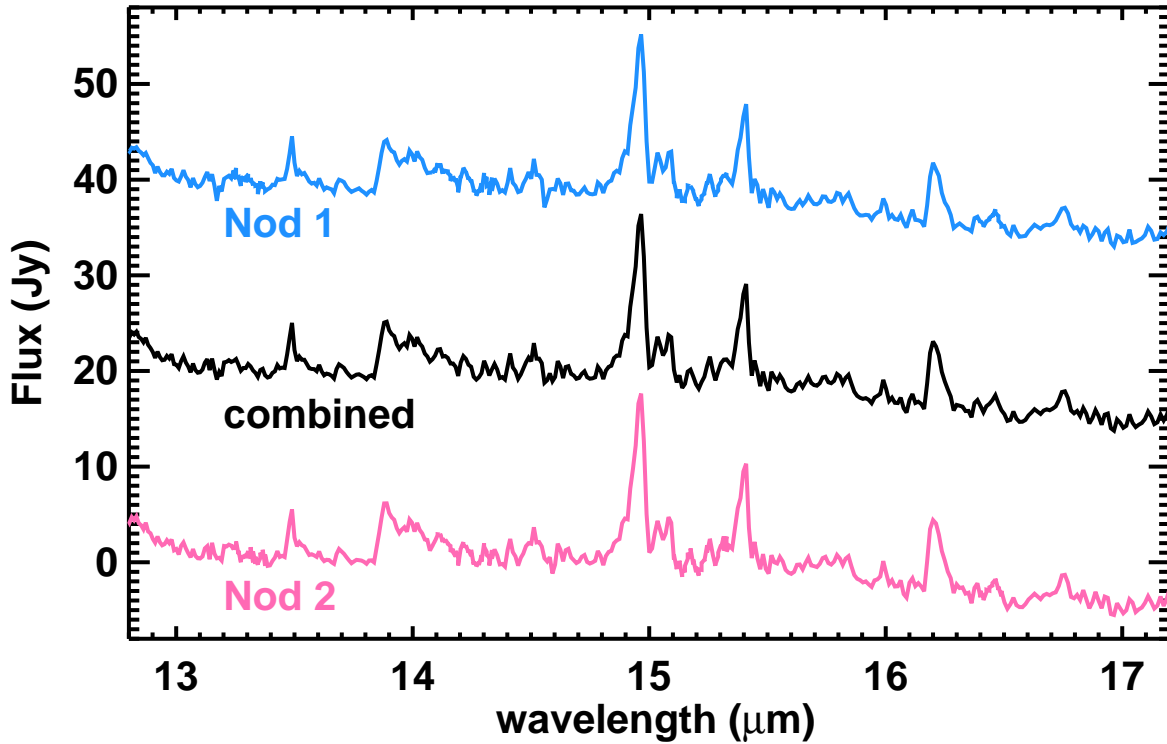


Figure 2.2: The same spectral region as shown in Figure 2.1. Here, we show both nods with the orders scaled (offset upwards and downward by 20 Jy for nods 1 and 2 respectively) compared to the final spectrum.

When this is done, we compare the nods and overlap regions again and as long as there are not any issues (e.g. the features in each nod correspond to one another), we combine them using a weighted mean (\bar{x} , Bevington & Robinson, 2003):

$$\bar{x} = \frac{\sum \left(\frac{x_i}{\sigma_i^2} \right)}{\sum \frac{1}{\sigma_i^2}}, \quad (2.1)$$

where x_i represents one flux measurement at a particular wavelength (e.g. the flux from one nod position or one order in an overlap region) and σ_i is its uncertainty. We also calculate uncertainties on the new data points using:

$$\sigma^2 = \frac{1}{\sum \frac{1}{\sigma_i^2}}. \quad (2.2)$$

We present an example of the result of trimming and scaling the orders as well as combining the different nods in Figure 2.2.

If there are large discrepancies between nods, we take note of them, but typically do not take any action unless there is a clear issue since it is not always obvious which nod position is correct. In an overlap region, however, we have four observations (two from each nod) so if one observation appears significantly different than the other three, we may assign higher uncertainties on it (giving it less weight) or omit it from the calculation of the weighted mean entirely.

If there is a clear problem in one of the nod positions such as an unresolved spike—a feature consisting of just a single point—we remove it from the observations by interpolating between the data points on either side and assign this point a large uncertainty before calculating the weighted mean at this wavelength.

2.3.1 Finishing Touches and Notes

When we scale the fluxes of different components of the spectrum, we can change the overall flux of the spectrum. As a result, we typically compare our final spectrum to the flux measurements from the Infrared Astronomical Satellite (IRAS) and scale our measurements accordingly.

Furthermore, the data reduction steps described so far carry through the uncertainty estimates on the fluxes from the pipeline. However, the pipeline may underestimate the uncertainty on the flux. Therefore, we attempt to find a region of the spectrum which is free from molecular features then, fit it with a straight line and calculate the standard deviation between the data and that line to use as the uncertainties on the flux measurements when we compare our observations to models.

Finally, when we have completed our analysis of a spectrum, if there are any unusual features in the data which we could not characterize with our models, we may revisit the earlier reduction steps. This can include anything from comparing the two nod positions again to re-extracting the data and comparing the results from individual DCEs or attempting different defringing techniques. If the feature persists, then we are more confident that it is a real feature than if it does not.

We also note that for the Spitzer spectra we present in this thesis, the observations of HR 4049 did not require as much intervention as that of SMP LMC 11. This is likely due to the much larger flux of HR 4049 as compared to SMP LMC 11 ($F_{\nu} \approx 5 - 50$ Jy versus $F_{\nu} \approx 0.5$ Jy, respectively) as well as the greater number of DCEs available.

Bibliography

Bevington P.R., Robinson D.K., 2003, Data reduction and error analysis for the physical sciences

Higdon S.J.U., Devost D., Higdon J.L., et al., 2004, *PASP* 116, 975

Houck J.R., Roellig T.L., van Cleve J., et al., 2004, *ApJS* 154, 18

Lebouteiller V., Bernard-Salas J., Sloan G.C., Barry D.J., 2010, *PASP* 122, 231

Werner M.W., Roellig T.L., Low F.J., et al., 2004, *ApJS* 154, 1

Chapter 3

Circumstellar Chemistry of SMP LMC 11

Appeared as:

“The Rich Circumstellar Chemistry of SMP LMC 11”

S.E. Malek, J. Cami & J. Bernard-Salas

The Astrophysical Journal 744, 16, 2012

Abstract: Carbon-rich evolved stars from the asymptotic giant branch to the planetary nebula phase are characterized by a rich and complex carbon chemistry in their circumstellar envelopes. A peculiar object is the preplanetary nebula SMP LMC 11, whose *Spitzer* Infrared Spectrograph spectrum shows remarkable and diverse molecular absorption bands. To study how the molecular composition in this object compares to our current understanding of circumstellar carbon chemistry, we modeled this molecular absorption. We find high abundances for a number of molecules, perhaps most notably benzene. We also confirm the presence of propyne ($\text{CH}_3\text{C}_2\text{H}$) in this spectrum. Of all the cyanopolyynes, only HC_3N is evident; we can detect at best a marginal presence of HCN. From comparisons to various chemical models, we can conclude that SMP LMC 11 must have an unusual circumstellar environment (a torus rather than an outflow).

3.1 Introduction

As stars with initial masses between 0.8 and 8–9 M_{\odot} approach the end of their lives, they reach the asymptotic giant branch (AGB) stage. The AGB is characterized by alternate hydrogen and helium shell burning, dredge-up events and extreme mass-loss rates (up to $10^{-4} M_{\odot} \text{ yr}^{-1}$; Iben & Renzini, 1983). This high mass loss causes the star to evolve further, leaving the AGB. When a star leaves the AGB it may become what is known as a preplanetary nebula (pPN) during a relatively short-lived (lasting $\sim 10^3$ – 10^4 yr; Vassiliadis & Wood, 1993) transitional period before becoming a planetary nebula (PN).

The material lost by a star during its time on the AGB goes into the circumstellar environment (CSE) before it is dispersed into the interstellar medium (ISM). The CSE is a relatively cool region (with temperatures lower than the effective temperatures of AGB stars, where $T_{\text{eff}} \approx 3000$ K), which allows the formation of molecules and dust beginning on the AGB and continuing into the (p)PN stages.

One of the first and most stable molecules to form in the CSE is CO. As a result, the relative amounts of carbon and oxygen in the CSE largely determine future chemistry. Stars begin their lives with more oxygen than carbon ($C/O < 1$), but depending on the initial stellar mass and metallicity, an AGB star may undergo sufficient dredge-up events and become carbon-rich ($C/O > 1$), resulting in what is known as a carbon star (or a carbon-rich star).

The chemistry of carbon stars can result in an assortment of molecules due to the ability of carbon to form a variety of chemical bonds. For example, more than 60 molecules have been detected in the CSE of the prototypical carbon-rich AGB star IRC+10216 (e.g. Cernicharo et al., 1996).

The carbon chemistry in the CSE of AGB stars and (p)PNe is also of particular interest because a group of molecules known as polycyclic aromatic hydrocarbons (PAHs) are thought to form here (Latter, 1991). These molecules are ubiquitous in the universe with up to 10%–15% of cosmic carbon contained in PAHs (Snow & Witt, 1995).

In the current models of PAH formation, benzene (C_6H_6) formation is considered a bottleneck step (Frenklach & Feigelson, 1989; Cherchneff et al., 1992).

Not much is known about the formation of benzene in the CSEs of evolved stars, although there are chemical models describing its formation in the inner shocked regions of the CSE surrounding AGB stars (Cherchneff et al., 1992) as well as through photochemical reactions in the CSE of pPNe (Woods et al., 2002, 2003).

While PAHs are ubiquitous in the universe (including carbon-rich PNe), benzene is not often found in evolved stars; it has been found in just two objects thus far: CRL 618 (Cernicharo et al., 2001b) and SMP LMC 11 (Bernard-Salas et al., 2006, hereafter Paper I). This suggests that it is either difficult to form or that it reacts quickly once formed.

In this paper, we will discuss the latter object, SMP LMC 11, which is a carbon-rich pPN in the Large Magellanic Cloud. It is described as a low-excitation pPN (Sanduleak et al., 1978; Morgan, 1984) and has a bipolar outflow (Shaw et al., 2006). It also shows a rather high expansion velocity (122 km s^{-1} ; Dopita et al., 1988) with multiple velocity components.

Here we present a detailed analysis of the molecular absorption bands in the mid-infrared spectrum of SMP LMC 11 (first presented in Paper I) and show that our results are inconsistent with current models for the chemistry in evolved carbon-rich CSEs.

We begin this paper with a description of the observations and data reduction in Section

3.2, then we describe the dust continuum in Section 3.3. We follow this with an inventory of the molecular bands in the spectrum and the method we use to model these bands in Section 3.4. We then present our results from our model fits in Section 3.5. Next, we discuss the implications of our results for the evolutionary status, chemical evolution and geometry of SMP LMC 11 in Section 3.6. Finally, we present our conclusions in Section 3.7.

3.2 Observations and Data Reduction

SMP LMC 11 was observed with the *Spitzer Space Telescope* (Werner et al., 2004) Infrared Spectrograph (IRS; Houck et al., 2004) as part of the GTO program on 2005 June 6 (program ID 103, AOR key 4947712). Here we present a new reduction of the spectrum with the latest calibration files (pipeline version S18.18). We obtained the basic calibrated data (BCD) files for SMP LMC 11 and processed the data for the short high (SH, $R = 600$, $\lambda = 9.9\text{--}19.6\ \mu\text{m}$), short low (SL, $R = 60\text{--}127$, $\lambda = 5.2\text{--}14.5\ \mu\text{m}$) and long low (LL, $R = 57\text{--}126$, $\lambda = 14.0\text{--}38.0\ \mu\text{m}$) modes.

We cleaned the data using `IRSCLEAN` with the campaign rogue pixel mask and extracted it in `SMART v8.2.1` (Higdon et al., 2004); we extracted the SH data using full aperture extraction, and the SL and LL data with the manual optimal extraction mode (Lebouteiller et al., 2010). Next we defringed the LL mode and trimmed the edges of the orders for all modules to remove edge effects. We eliminated flux jumps between the orders by comparing the overlap regions and scaling the orders (for the SH, orders were scaled to match order 20, for the low-resolution data SL2 was scaled to SL1 and both were scaled to the LL data), then we averaged the flux from the two nod positions. Since we were unsure of the reliability of the initial uncertainty estimates, we instead estimated the uncertainties on the flux values by measuring the standard deviation in a featureless region of the SH spectrum between 16.53 and $17.44\ \mu\text{m}$; we found a standard deviation of $0.0122\ \text{Jy}$, corresponding to a signal-to-noise (S/N) of 47 in this range.

Finally, to facilitate comparison to molecular models, we shifted the spectrum to the rest frame using a radial velocity of $263.5\ \text{km s}^{-1}$ (Morgan & Parker, 1998) and the relative motion of *Spitzer* at the time of the observations ($V_{\text{LSR}} = 12.5\ \text{km s}^{-1}$). The full low-resolution spectrum is shown in Figure 3.1.

3.3 The dust continuum

Figure 3.1 shows the *Spitzer*–IRS continuum as well as the Two Micron All Sky Survey (2MASS; Skrutskie et al., 2006) H –, J – and K –band fluxes (Cutri et al., 2003). From those data, it seems clear that there is no appreciable stellar continuum that could contribute to the

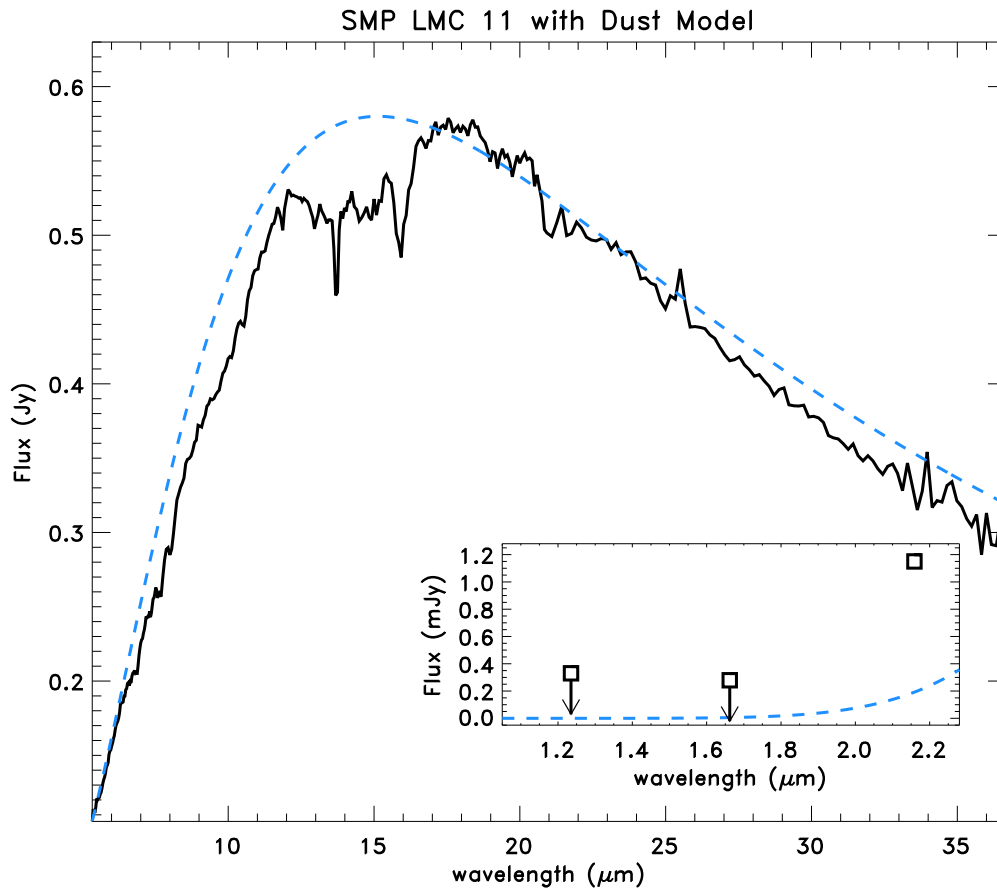


Figure 3.1: *Spitzer*–IRS low-resolution spectrum (SL and LL combined) of SMP LMC 11 (black) and a dust model (dashed blue line). The inset shows the 2MASS fluxes with the dust model.

mid-IR emission. We thus conclude that the flux in the entire IRS spectrum is dominated by dust emission.

The region beyond $17\ \mu\text{m}$ has a few apparent features near 19 and $21\ \mu\text{m}$ in the LL data. However, as these features are absent from a quick reduction of the long high (LH, $R = 600$, $\lambda = 18.7\text{--}37.2\ \mu\text{m}$) data, we consider these to be artifacts. Thus, the dust emission does not show clear spectral features, and thus is presumably caused by amorphous carbon dust.

Since it is precisely this dust emission that is then absorbed by molecular bands (especially in the $10\text{--}17\ \mu\text{m}$ region, see Figure 3.1), we require some idea about the properties of this dust continuum before we can model the molecular bands. A single blackbody curve cannot properly reproduce the overall shape of the dust continuum, suggesting that there is some stratification in the dust layers. From our point of view, we can see through the outer (and colder) dust layers up the point where the dust becomes optically thick; at that point, the dust

temperature is T_d^{\max} . We thus approximated the dust emission by a weighted sum of blackbody spectra at temperatures between T_d^{\max} and an arbitrarily chosen minimum temperature T_d^{\min} of 25 K in steps of 25 K. Assuming optically thin dust in radiative equilibrium with the hottest (optically thick) dust, we then determined the appropriate weights for each temperature bin consistent with a constant-velocity outflow at a constant mass-loss rate (i.e., we determined the mass in each layer). We find that the best model is one with a maximum dust temperature of about 425 K (see Figure 3.1). However, even in such a case, we overestimate the dust emission at the longer wavelengths; this suggests that there is less cold dust than expected for a constant-velocity outflow at a constant mass-loss rate. Nonetheless, the cold dust does not matter much for the analysis of the molecular bands; for the modeling presented in this paper, we assume that the molecules are absorbing 425 K blackbody radiation.

We also note that our dust temperature estimate is higher than that in Paper I, but our estimate should be more reliable than their graybody fit.

3.4 Molecular bands

3.4.1 Molecular Inventory

Superposed on the dust emission are many absorption features due to various molecular species (see Figure 3.2). We will restrict our discussion to wavelengths shorter than $17 \mu\text{m}$, where most of the absorption occurs.

Here, we describe the molecular bands in great detail and determine the physical conditions by modeling these bands.

Acetylene (C_2H_2) is often the dominant molecular absorber in the infrared spectra of carbon-rich pPNe. In the spectrum of SMP LMC 11, C_2H_2 provides by far the strongest absorption. The Q -branch for the ν_5 bending mode is obvious as a very deep absorption feature at $13.7 \mu\text{m}$; additionally, the P - and R -branches of C_2H_2 cause much of the broad and deep absorption that is obvious between 12 and $16 \mu\text{m}$ (see Figure 3.1). Such broad and deep C_2H_2 absorption is also seen in some other carbon-rich objects, such as the carbon star IRAS 04496-6958 (Speck et al., 2006), for example. In addition, acetylene exhibits a much weaker combination band ($\nu_4 + \nu_5$) at $7.5 \mu\text{m}$ which is blended with other features in the spectrum of SMP LMC 11.

Larger acetylene chains are less commonly observed in the CSE of pPNe (Fonfría et al., 2011). In the spectrum of SMP LMC 11 though diacetylene (C_4H_2) is another major contributor to the molecular absorption in the spectrum. The ν_8 bending mode of this species appears at $15.9 \mu\text{m}$ and the $\nu_6 + \nu_8$ combination band is clearly visible at $\sim 8 \mu\text{m}$. Small amounts of the corresponding ν_{11} bending mode of triacetylene (C_6H_2) might be present in the red wing of the

15.9 μm feature.

In contrast, HCN—which often shows up in carbon star spectra alongside the C_2H_2 band at 14 μm —at best barely contributes to the absorption in this spectrum. It is thus surprising that HC_3N is present and shows a clear and deep absorption at 15.03 μm from its bending mode. There is no evidence for any longer cyanopolynes; for instance, there is no absorption at 15.57 μm from the ν_7 band of HC_5N .

Nearly unique for pPNe (with one other detection thus far in CRL 618; see Cernicharo et al., 2001b), the spectrum also shows significant benzene absorption (as noted in Paper I). It has its deepest absorption at 14.85 μm , where the ν_4 bending mode absorbs more than 15% of the total continuum flux. Additionally, strong absorption is clearly present at the wavelengths where other strong benzene bands are expected: another bending mode (ν_{14}) at 9.6 μm and a ring stretching and deforming mode (ν_{13}) at 6.72 μm .

In the blue wing of the C_4H_2 band, near 15.78 μm , some additional absorption could be due to the ν_8 bending mode of propyne ($\text{CH}_3\text{C}_2\text{H}$, also sometimes called methylacetylene) at 15.78 μm , as suggested in Paper I. Furthermore, there is also some absorption visible in the spectrum from the ν_4 band of CH_4 at 7.7 μm as well as the ν_7 band of C_2H_4 at 10.53 μm . Finally, we could not determine the origin of the absorption feature near 10.38 μm , although we suspect a molecular origin for this feature.

3.4.2 Modeling the molecular absorption

We modeled the molecular absorption using the same methods that are used to build the SpectraFactory database (Cami et al., 2010). These model calculations start from line lists detailing the frequencies and intensities of the individual molecular transitions.

Line lists for C_2H_2 (including the H^{13}CCH isotopologue), HCN, CH_4 , and C_2H_4 are taken from the HITRAN 2008 database (Rothman et al., 2009); the line lists for C_4H_2 , C_6H_6 , HC_3N , and $\text{CH}_3\text{C}_2\text{H}$ are from the GEISA database (Jacquinet-Husson et al., 2008).

As we could not find reliable line lists for all species or bands, we calculated some line lists from molecular constants and PGOPHER v 7.1.108 (Western, 2010). The GEISA line list for benzene contains only data for the fundamental ν_4 band. Thus, in order to model benzene absorption at the shorter wavelengths in the SL data, we calculated line lists for the ν_{13} and ν_{14} bands using molecular constants from Dang-Nhu & Plíva (1989). Similarly, the GEISA line list for C_4H_2 does not contain data for the transitions of the $\nu_6 + \nu_8$ combination band at $\sim 8 \mu\text{m}$; we thus calculated a line list using molecular constants found in Arié & Johns (1992), Guelachvili et al. (1984), and Khelifi et al. (1995). Finally, we calculated a C_6H_2 list using data from McNaughton & Bruget (1991).

From these line lists, we calculated optical depths assuming a population in local thermodynamic equilibrium and a Gaussian intrinsic line profile with a width of 10 km s^{-1} , which is typical of outflows of evolved stars. We carried out radiative transfer through isothermal, plane-parallel molecular slabs in front of a 425 K blackbody background (see Section 3.3) and smoothed and rebinned the resulting models to match the resolving power of the observations—600 for the SH module and 90 for the SL data.

We compared the resulting models to the observations (normalized by a cubic spline continuum) and calculated χ_v^2 , the reduced χ^2 statistic. However, we note that there may be some systematic errors as well. For instance, it is important to realize that the current line lists for C_2H_2 do not allow us to reproduce the broad and deep absorption in the 12–16 μm (see Speck et al., 2006, for a discussion).

To find the best model, we calculated models at different temperatures ranging from 200 to 400 K with a step size of 25 K, and similarly at column densities between $N = 10^{15}$ and $N = 10^{19} \text{ cm}^{-2}$ in steps of $\log N = 0.1$ and then calculated the χ_v^2 value for each model. For wavelength ranges containing absorption due to several species, we properly treated line overlap by summing the optical depth profiles for each contributing molecule prior to performing the radiative transfer calculations when we fit several species simultaneously. We thus simultaneously modeled the absorption of the C_2H_2 isotopologues and HCN between 12 and 14 μm and similarly also combined C_4H_2 , C_6H_2 , $\text{CH}_3\text{C}_2\text{H}$ and HC_3N in the 15–16.5 μm range. We fit benzene to the spectrum between 14.2 and 15 μm and C_2H_4 from 10.5 to 11 μm . Where overlap appeared across the modeled regions, we added the optical depth values determined from earlier fits to the new regions (e.g., the best-fit optical depths for C_2H_2 and HCN were added to the optical depth for the C_4H_2 , C_6H_2 , HC_3N , and $\text{CH}_3\text{C}_2\text{H}$ fits) and then performed the radiative transfer calculations. We expect that small errors may be introduced using this method, but due to the small difference in temperature between the layers, this effect should not be large.

Using the results from fitting the SH observations, we predicted the absorption in the SL data for benzene, C_2H_2 , and C_4H_2 . The CH_4 absorption was fit by itself between 7.5 and 7.9 μm , but the optical depth profiles for the $\nu_6 + \nu_8$ band of C_4H_2 as well as the C_2H_2 band at 7.5 μm as determined in the SH data were added to the total optical depth profile prior to calculating the radiative transfer calculations for the CH_4 fits.

3.5 Results

The best fits for the SH and SL data are shown in Figure 3.2; the corresponding parameters are listed in Table 3.1. As can also be seen from the residuals in Figure 3.2, our models reproduce

Molecule	$\log N$	T (K)	
C_2H_4	$17.30^{+0.05}_{-0.50}$	350	$+50$ -50
C_2H_2	$18.10^{+0.05}_{-0.05}$		
$H^{13}CCH$	$16.90^{+0.10}_{-0.10}$	375	$+25$ -50
HCN	$16.50_{-1.50}$		
C_6H_6	$17.80^{+0.40}_{-1.00}$	350	$+50$ -50
C_4H_2	$17.10^{+0.05}_{-0.05}$		
CH_3C_2H	$17.00^{+0.10}_{-0.05}$	325	$+12.5$ -25
HC_3N	$16.40^{+0.10}_{-0.05}$		
CH_4	$17.80^{+0.70}_{-0.20}$	250	$+150$ -12.5

Table 3.1: Temperatures and Column Densities for the Best Model Fits to Our Data as well as Nominal 1σ Uncertainties.

the observations quite well ($\chi^2_\nu \approx 0.84$ over the entire fitting region). Our best fits indicate that the molecules are found in a range of temperatures from 250–375 K; however, some of the temperature stratification may be artificial due to the large uncertainties on our temperature determinations.

3.5.1 Benzene

To fit the ν_4 bending mode of benzene at $14.85 \mu\text{m}$, we require a high column density ($\log N = 17.80$) consistent with the deep absorption in the spectrum. Our model reproduces the depth of the absorption feature well, but does not match the width and profile shape. This discrepancy is probably due to the absence of hot bands in our molecular model. Hot bands are generally slightly offset compared to the fundamental mode, and thus tend to broaden the absorption band. At the relatively high temperature of benzene found here, we certainly expect some contribution from the hot bands; at 300 K, only 54% of the molecules should be in the ground state (Kauppinen et al., 1980). However, hot bands are not included in the GEISA line list for benzene. As a result, our model fit is much narrower than it should be.

Using the benzene parameters found from fitting the ν_4 band, we predicted the appearance of the bands at 9.6 and $6.7 \mu\text{m}$. As seen in Figure 3.2, while there are absorption features at these wavelengths consistent with benzene, our predictions do not fit these bands particularly well. At $9.6 \mu\text{m}$, we can see that the predicted absorption is much deeper than the observed band, although the band shape is similar.

The feature at $6.7 \mu\text{m}$ is more unusual: while there is an overall absorption feature in the spectrum of SMP LMC 11 at this wavelength, the feature is much broader than our model and shows what could be a small emission bump right at the central wavelength of the benzene

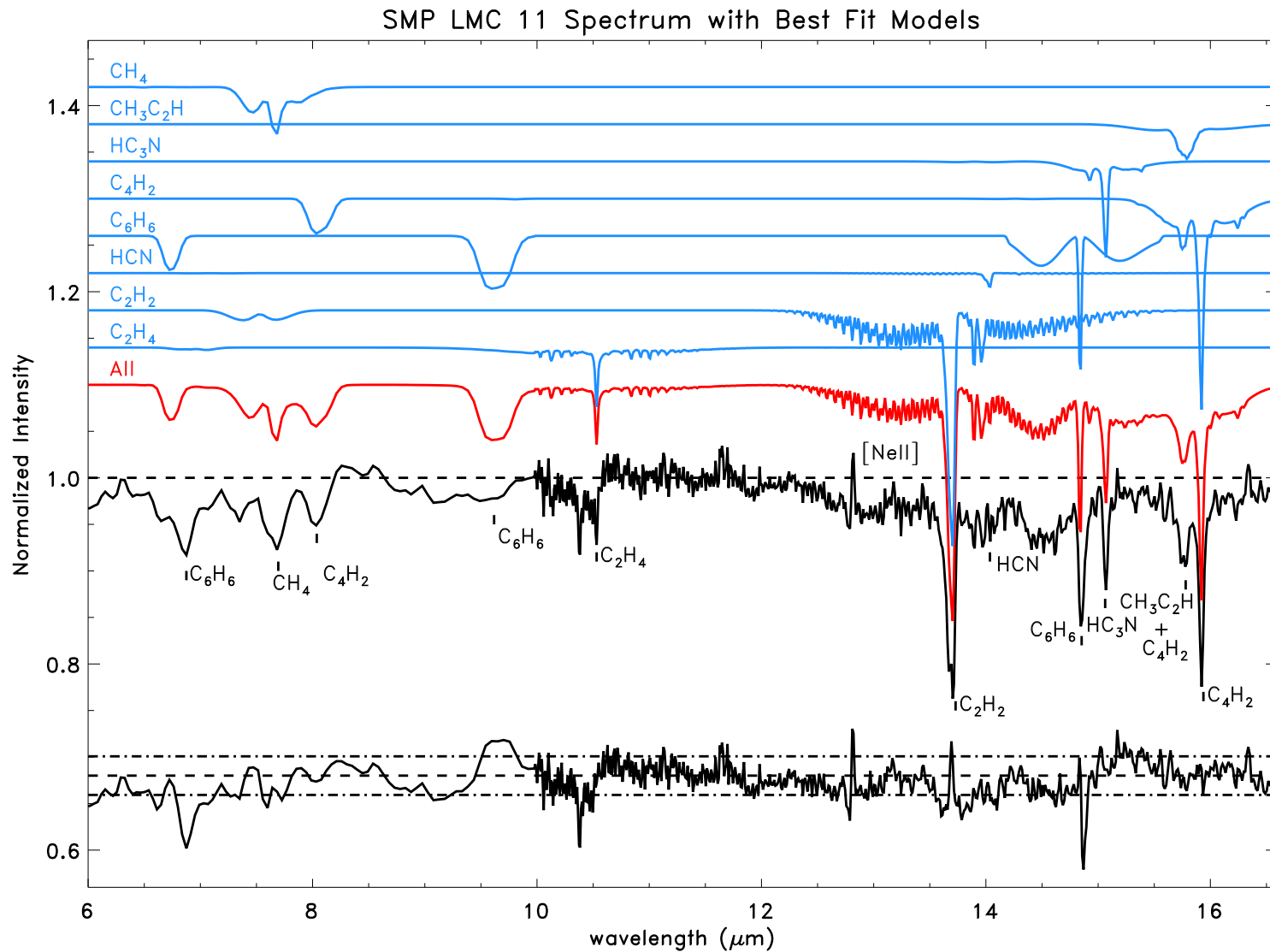


Figure 3.2: Normalized SL and SH spectra for SMP LMC 11 from 6 to 16.6 μm with our best-fit models and residuals. The combined best fit is shown offset above the spectrum in red and the individual best fits for each molecule are offset above this in blue. The residuals are shown offset below the spectrum and the dot-dashed lines indicate the error ranges.

absorption. Just as for the $14.85 \mu\text{m}$ band, the broader observed feature could be a consequence of the absence of hot bands in our model. Indeed, we note that the absorption in the spectrum appears to be approximately twice as broad as in the model, with a similar red degraded wing (see Figure 3.3). Thus, we consider benzene the carrier for the overall absorption feature at $6.7 \mu\text{m}$. The nature of the small emission bump is not clear. If this is a real emission feature, it seems unlikely that it would be due to benzene, since we do not see any similar emission at the other benzene absorption bands.

3.5.2 Acetylene Chains

The C_2H_2 absorption at $13.7 \mu\text{m}$ is the deepest and broadest absorption feature in the spectrum. Accordingly, we find the highest column density for this feature ($\log N = 18.10$) of the molecular bands we fit. Since we ignored the deep and broad absorption between 12 and $16 \mu\text{m}$ which is at least partly due to C_2H_2 , this is clearly a lower limit of the true column density. In addition to the main isotopologue, we detect a fairly high column density of H^{13}CCH ($\log N = 16.90$) yielding a $N_{12\text{C}_2\text{H}_2}/N_{\text{H}^{13}\text{CCH}}$ ratio of 16 and a $^{12}\text{C}/^{13}\text{C}$ ratio of 33. This is in the low end of the range for carbon-rich objects as determined by Milam et al. (2009), who found $^{12}\text{C}/^{13}\text{C}$ ratios between 25 and 90. However, since we underestimate the column density of the main isotopologue, this is most certainly an absolute lower limit to the $^{12}\text{C}/^{13}\text{C}$ ratio. Similarly, from the column densities of C_2H_2 and C_4H_2 , we find a ratio of $\text{C}_2\text{H}_2/\text{C}_4\text{H}_2$ of 10, which would again be a lower limit.

We find that the identification of the ν_{11} band of C_6H_2 in this spectrum is uncertain. Using reasonable defringing techniques, the apparent absorption feature near $16.1 \mu\text{m}$ disappears (see Figure 3.4). Further, when the molecular constants from McNaughton & Bruget (1991) are used to calculate a model line list, we find that the calculated band center appears $0.02 \mu\text{m}$ longer of the apparent absorption in the spectrum. A comparison between our calculated model and the previously identified C_6H_2 absorption in CRL 618 (Cernicharo et al., 2001b) in Figure 3.4 indicates that our calculated model is at least correct in peak position, so we consider it possible that the apparent C_6H_2 absorption is not real.

If we assume that the peak near $16.07 \mu\text{m}$ is due to C_6H_2 and shift our model of this band accordingly, the best fit is obtained at $\log N = 15.60_{-0.60}^{+0.70}$, which does not reproduce the shape of the band. In order to fit the band shape, a $\log N$ of 16.30 is required. However, since we have to assume that the position of our band as well as our continuum choice is incorrect to obtain this result, it seems unlikely that this feature is actually C_6H_2 .

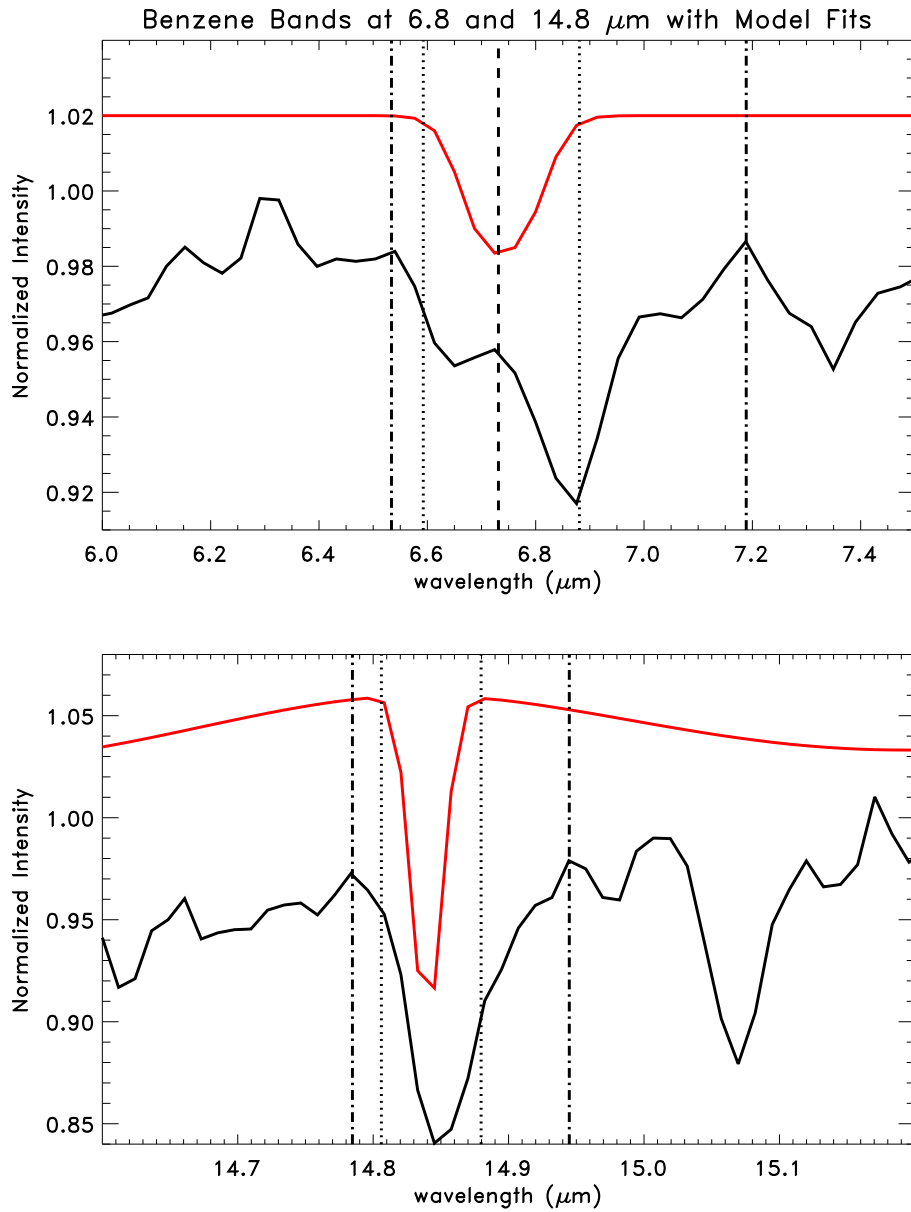


Figure 3.3: Benzene bands at 6.8 (top) and 14.8 μm (bottom), the spectra are in black while the benzene models are in red. The dot-dashed vertical lines show the extent of the main absorption in the spectra, the dotted lines show the width of the model absorption for the entire band (at 6.8 μm) and for the Q -branch (at 14.8 μm). The dashed line in the top figure shows the center of the absorption, coincident with the emission at the center of the 6.8 μm band.

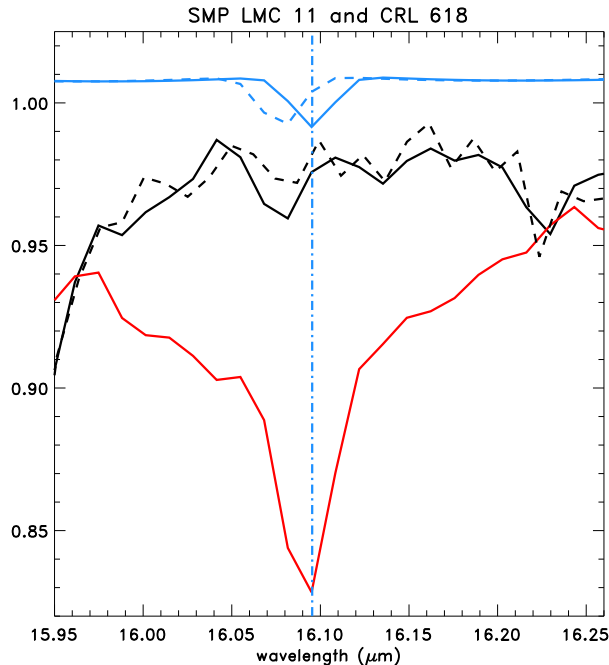


Figure 3.4: Normalized spectra of SMP LMC 11 (black) and CRL 618 (red) are shown with the C_6H_2 models. The model calculated using molecular constants from McNaughton & Bruget (1991) is shown in the solid blue lines, while the modified model is in dashed blue lines. The band center for the model calculated with molecular constants from McNaughton & Bruget (1991) is highlighted with a blue dot-dashed line. The dashed black line indicates an alternate fringing method for SMP LMC 11 wherein the appearance of the $16.07 \mu m$ feature is greatly diminished.

3.5.3 Cyanopolyynes

Although there is no obvious absorption from HCN at $14 \mu m$, our modeling attempts suggest that the overall fit is slightly better if HCN is included; in fact, we find a similar (low) column density for HCN as we do for the much stronger HC_3N . To verify whether the addition of HCN *significantly* improves the fit, we performed an F -test for an additional term (see Bevington & Robinson, 2003). We find that for HCN, $F_\chi = 0.993$, and the probability of achieving this value for F_χ with the addition of a random factor in our model is 32%. Thus, HCN does not significantly improve the fit at this wavelength range and the column density we find should therefore be considered an upper limit. Thus, the upper limit for $HCN/HC_3N \approx 1$.

We do not detect any absorption at the position of the bending mode of HC_5N at $15.57 \mu m$. Since the band strengths for the bending modes of HC_5N ($268.2 \text{ cm}^{-2}\text{atm}^{-1}$; Bénilan et al., 2007) and HC_3N ($245.1 \text{ cm}^{-2}\text{atm}^{-1}$; Jolly et al., 2007) are fairly similar and since the modes should have a similar profile, this suggests that HC_5N is simply not present in SMP LMC 11.

From the measured equivalent width of the band ($0.007 \mu\text{m}$) and the S/N of ~ 85 in this part of the spectrum, we estimate an upper limit of $\log N = 15.4$ to the column density for HC_5N , yielding a lower limit to the $\text{HC}_3\text{N}/\text{HC}_5\text{N}$ ratio of 10.

3.5.4 Other Species

Our best-fit model shows a clear contribution from $\text{CH}_3\text{C}_2\text{H}$ at a relatively high column density, blended with the C_4H_2 absorption band. Again, we performed an F -test and found that in this case, adding $\text{CH}_3\text{C}_2\text{H}$ does indeed significantly improve the fit: we find $F_\chi = 53$ and the probability of observing this F_χ value with the addition of a random factor is $\sim 10^{-8}\%$. This absorption cannot be due to isotopologues of C_4H_2 either, as these absorb at longer wavelengths than the main isotopologue peak (at 15.95 and $15.93 \mu\text{m}$ for $\text{H}^{13}\text{CCCCH}$ and $\text{HC}^{13}\text{CCCH}$, respectively; Jolly et al., 2010). We thus conclude that $\text{CH}_3\text{C}_2\text{H}$ is indeed present in the spectrum of SMP LMC 11. Note that this species was also observed in the pPN CRL 618 at millimeter wavelengths, and that it was suggested to contribute to the absorption at infrared wavelengths too (Cernicharo et al., 2001a). Here, however, we find a higher column density.

Finally, we also find good fits and fairly high column densities for the CH_4 absorption at $7.7 \mu\text{m}$ and the C_2H_4 absorption at $10.53 \mu\text{m}$.

Judging from the residuals and low overall χ^2 , we have accounted for most of the molecular absorption. Thus, any additional molecular bands apart from those already noted must be either weak or perhaps shallow and broad.

3.6 Discussion

The rich molecular spectrum of SMP LMC 11 seems to offer a unique astrophysical laboratory to study chemical pathways in carbon-rich environments, including the formation of benzene. Indeed, although the CSE of SMP LMC 11 shares some properties with CRL 618—the only other pPN in which benzene is detected—there are some significant differences that offer clues to the conditions required for the efficient formation of benzene and other carbonaceous molecules.

3.6.1 Circumstellar geometry

The first aspect we consider is the geometry of the CSE and the physical conditions of the material within. The continuum emission in the *Spitzer*–IRS observations is due to dust and provides the background intensity against which the molecular gas absorbs. Thus, the molecular gas is either mixed in with the dust or located further from the star. Additionally, the dust

must be optically thick at infrared wavelengths to explain the overall shape of the combined SL and LL spectrum. Moreover, optically thick dust is consistent with the featureless shape of the dust continuum which can be represented reasonably well with blackbody curves (see also Section 3.3).

It is clear that the physical conditions in the CSE of SMP LMC 11 are somewhat different from those in CRL 618: the CSE of SMP LMC 11 is denser and warmer than that of CRL 618. We find a typical dust temperature of 425 K, whereas the dust temperature of CRL 618 is 98–110 K (Fonfría et al., 2011). Similarly, the molecular excitation temperatures are slightly higher—250–400 K versus 200–250 K—and we also find higher column densities (e.g. $N(\text{C}_2\text{H}_2) = 2 \times 10^{17} \text{ cm}^{-2}$ in CRL 618, Cernicharo et al., 2001b, versus $\geq 10^{18} \text{ cm}^{-2}$ in SMP LMC 11).

If the CSEs of both CRL 618 and SMP LMC 11 were simple outflows, the higher temperatures in SMP LMC 11 would indicate that the dust is located closer to the star and thus that SMP LMC 11 turned off the AGB more recently. Indeed, the dust and molecular gas temperatures in SMP LMC 11 are more typical of a late AGB star than a pPN for which dust temperatures of 150–300 K are expected (Kwok, 2000). However, as seen in Figure 3.2, the *Spitzer*–IRS spectrum of SMP LMC 11 also exhibits weak emission from [Ne II], which is typically one of the first excitation lines seen in young PNe. This clearly indicates that the central star is much hotter than a typical AGB star and is thus in the pPN stage. This apparent contradiction is easily reconciled if we consider that the [Ne II] line does not originate from the same region as the molecular absorption and the dust. Indeed, since the dust is optically thick, the gas from which the [Ne II] originates cannot be located in a direct line of sight toward the central star: the dust hides the innermost region from view and no ionizing radiation can be expected to penetrate this thick dust layer. Thus, the [Ne II] line must originate from a region which is geometrically distinct from the location of the dust and the molecular gas and which is not obscured by dust.

The current results suggest that the molecular gas and dust surrounding SMP LMC 11 is located in a thick torus that we see fairly edge-on, as previously suggested in Paper I. In such a geometry, the gas that causes the [Ne II] emission would then be in a bipolar outflow. The properties of the central object thus correspond to those of a pPN, but the circumstellar material does not correspond to a pPN outflow and evolves on its own timescale since it resides in a massive disk. Such a disk with optically thick dust would also shield the circumstellar material from the intense radiation of the central object. Note that a radially constrained dusty torus could also explain why a dust model with a constant-velocity outflow at a constant mass-loss rate overestimates the flux at the longer wavelengths.

Thus, from the geometrical point of view, SMP LMC 11 is very similar to CRL 618 for

which a similar geometry involving a dense torus (in addition to a bipolar outflow) is observationally established (see, e.g., Burton & Geballe, 1986). Such massive, vertically extended and long-lived disks are often seen around binary systems containing an evolved star such as the Red Rectangle (see, e.g., Jura et al., 1995; Waters et al., 1998), for example. However, it is not clear what is the primary cause for the higher temperatures in SMP LMC 11. This could simply indicate that the torus is closer to the central star than for CRL 618, either because the CSE is younger, or because it is expanding slower than that of CRL 618 (which is expanding at a rate of 20 km s^{-1} ; see, e.g., Herpin & Cernicharo, 2000). However, one could also attribute the different temperatures to differences in the optical thickness of the dust between the two objects. In either case, the molecular excitation seems constrained to a fairly small range in temperatures.

3.6.2 The chemistry in SMP LMC 11

In terms of the molecular composition, the most striking difference between SMP LMC 11 and CRL 618 is the much stronger absorption that we find for benzene. The center of the benzene band at $14.85 \mu\text{m}$ is about three times deeper in SMP LMC 11 than in CRL 618. It may be somewhat surprising then that we find a column density that is 130 times larger than what was found for CRL 618 (Cernicharo et al., 2001b); however, we believe that this difference is due to the fact that we used more recent line lists. Additionally, not only is benzene itself much more abundant in SMP LMC 11, it is also enhanced compared to most other species, especially compared to acetylene. If we take the lower limit for the column density of C_2H_2 at face value, we find that there is about twice as much C_2H_2 as there is benzene; for CRL 618, the ratio found between these molecules was about 40 (Cernicharo et al., 2001b).

The relative abundances of the acetylene chains might offer some hints about the chemistry leading to efficient benzene formation. Woods et al. (2002, 2003) found that the interstellar benzene formation route (McEwan et al., 1999) was not efficient in environments such as CRL 618. Instead, they proposed a much more efficient route in such environments starting from acetylene and HCO^+ . The same model also predicts high column densities of C_4H_2 and C_6H_2 that are similar to one another. In fact, this matches the abundances in CRL 618 to within a factor 4–6. In the spectrum of SMP LMC 11 however, we cannot reliably establish the presence of C_6H_2 in the spectrum. This suggests that there is yet another formation route to benzene in these warm and dense environments, or possibly some additional reactions that need to be considered. These reactions might involve fast and efficient ring-closing reactions that deplete C_6H_2 or an additional route to benzene formation that starts from the abundant C_2H_2 and C_4H_2 which then decreases the efficiency of the formation of C_6H_2 .

It is equally interesting to consider the benzene loss reactions. Chemical models for environments comparable to those studied here show that the main destruction route for benzene is a further reaction with CN to form benzonitrile (C_6H_5CN , Woods et al., 2003). This molecular species has strong absorption bands at 13.2 and 14.4 μm , which we do not observe in the spectrum of SMP LMC 11. Although the CN in these reactions is expected to originate from the photodissociation of HCN which is again at best marginally present in the spectrum of SMP LMC 11. Benzene destruction could thus be inhibited by the absence of the CN parent species.

The cyanopolyynes also present an interesting case. As shown in Cherchneff & Glassgold (1993), for example, the primary routes to the formation of cyanopolyynes in pPNe environments are through reactions between members of the acetylene family and the CN radical which itself is produced from HCN in photochemical reactions. Reactions between CN and C_2H_2 then result in HC_3N , while reactions with C_4H_2 yield HC_5N . Since both C_2H_2 and C_4H_2 are abundant in the spectrum of SMP LMC 11, we would thus expect fairly large abundances of the longer cyanopolyynes as well. However, while we clearly detect a strong absorption band due to HC_3N , we do not find much evidence for the parent molecule, HCN, nor for the longer cyanopolyynes. HC_5N , for instance, should have a strong bending mode at 15.57 μm (Bénilan et al., 2007) which does not appear in the spectrum (see Figure 3.2).

Such abundance patterns are very different from those observed in CRL 618 and cannot be accommodated by the chemical models for these environments (e.g. Cherchneff & Glassgold, 1993; Woods et al., 2003). Even if one would consider that HCN could be completely depleted by HC_3N formation, one would expect to see efficient formation of HC_5N as well since this involves the same mechanism and large amounts of C_4H_2 are available for this process. This observation then suggests that for the cyanopolyynes, some of the chemical pathways that are possible in pPNe environments might be missing from the models.

3.6.3 Pathways to PAHs?

The formation of benzene is often studied in the context of PAHs, for which they are the basic unit. In the formation pathways for PAHs, the formation of benzene is considered to be the bottleneck (see, e.g., Allamandola et al., 1989). We searched for any features due to neutral naphthalene and pyrene (two of the smallest PAHs consisting of two and three aromatic rings, respectively) but did not find any evidence for these species. However, since PAH formation cannot occur at the low temperatures in SMP LMC 11—typically 900–1100 K is required (Frenklach & Feigelson, 1989; Allamandola et al., 1989; Cherchneff et al., 1992), this should not be surprising.

It is interesting to consider what might happen to the benzene as the central star and CSE

evolve further. All other things being equal, the increasingly hotter central object would heat up the CSE. If the torus expands (as is the case for CRL 618), then the circumstellar material will become diluted and more transparent, which would clearly increase the importance of photochemistry. It is not immediately clear what the result of this increased photochemistry would be, but it is certainly possible that the conditions created are ideal for further processing of the circumstellar benzene into PAHs. If so, this might represent an important PAH formation pathway, provided that the torus contains enough mass to represent a significant carbon reservoir. Note that for objects like the Red Rectangle, the circumbinary disks are indeed found to be massive. However, in that particular object, PAHs are clearly found in the bipolar outflows (Waters et al., 1998) and not in the torus.

Although the molecular composition of the CSE of SMP LMC 11 is certainly unique thus far, we do not believe that the environment represented by this object is necessarily exceptional. CRL 618 is the only other source where benzene is detected, and it also shows different abundances for the polyynes and the cyanopolyynes. However, the two environments are very similar in many of their physical properties. Given the short expected timescales for the evolution from the tip of the AGB to the PN phase, it is reasonable to expect the evolution of CSEs to be fast. The two objects could then represent cases where either the initial conditions (of the torus, for example) were slightly different or, alternatively, they could represent slightly different steps in the evolution of the torus. It would certainly be interesting to study how the physical conditions of a (slowly expanding) dense torus change in this short evolutionary phase and how the chemistry in this environment will evolve.

3.7 Conclusions

We presented an analysis of the rich molecular absorption in the *Spitzer*-IRS spectrum of SMP LMC 11. We have compared it to chemical models for carbon-rich pPNe and to CRL 618, the only other pPN in which benzene is detected to date. The geometrical configuration in both objects is fairly similar and includes a dense, warm torus of material in which a rich molecular gas resides. However, the absolute and relative chemical abundances of the carbonaceous species in SMP LMC 11 do not match models and are also quite different from those in CRL 618. In particular, benzene is very abundant, making SMP LMC 11 an important environment to consider in the study of benzene and possibly also in PAH formation. Current chemical models can reproduce some of the molecular absorption, but not all of it. In particular, the absence of C_6H_2 and HC_5N seems to require additional ring-closing reactions that deplete those species. Alternatively, new chemical pathways have to be found for the formation of C_4H_2 and HC_3N that do not result in abundant formation of C_6H_2 and HC_5N . We encourage a

more detailed study of the chemical pathways which could explain these anomalies.

Bibliography

- Allamandola L.J., Tielens A.G.G.M., Barker J.R., 1989, *ApJS* 71, 733
- Arié E., Johns J.W.C., 1992, *J. Mol. Spectrosc.* 155, 195
- Bénilan Y., Jolly A., Trolez Y., Raulin F., Guillemin J.C., 2007, *J. Mol. Spectrosc.* 245, 109
- Bernard-Salas J., Peeters E., Sloan G.C., et al., 2006, *ApJL* 652, L29
- Bevington P.R., Robinson D.K., 2003, Data reduction and error analysis for the physical sciences
- Burton M.G., Geballe T.R., 1986, *MNRAS* 223, 13P
- Cami J., van Malderen R., Markwick A.J., 2010, *ApJS* 187, 409
- Cernicharo J., Barlow M.J., Gonzalez-Alfonso E., et al., 1996, *A&A* 315, L201
- Cernicharo J., Heras A.M., Pardo J.R., et al., 2001a, *ApJL* 546, L127
- Cernicharo J., Heras A.M., Tielens A.G.G.M., et al., 2001b, *ApJL* 546, L123, printed: category CRL 618
- Cherchneff I., Barker J.R., Tielens A.G.G.M., 1992, *ApJ* 401, 269
- Cherchneff I., Glassgold A.E., 1993, *ApJL* 419, L41
- Cutri R.M., Skrutskie M.F., van Dyk S., et al., 2003, 2MASS All Sky Catalog of point sources.
- Dang-Nhu M., Plíva J., 1989, *J. Mol. Spectrosc.* 138, 423
- Dopita M.A., Meatheringham S.J., Webster B.L., Ford H.C., 1988, *ApJ* 327, 639
- Fonfría J.P., Cernicharo J., Richter M.J., Lacy J.H., 2011, *ApJ* 728, 43, printed: category CRL 618
- Frenklach M., Feigelson E.D., 1989, *ApJ* 341, 372
- Guelachvili G., Craig A.M., Ramsay D.A., 1984, *J. Mol. Spectrosc.* 105, 156
- Herpin F., Cernicharo J., 2000, *ApJL* 530, L129
- Higdon S.J.U., Devost D., Higdon J.L., et al., 2004, *PASP* 116, 975

- Houck J.R., Roellig T.L., van Cleve J., et al., 2004, *ApJS* 154, 18
- Iben, Jr. I., Renzini A., 1983, *ARA&A* 21, 271
- Jacquinet-Husson N., Scott N.A., Chédin A., et al., 2008, *J. Quant. Spectrosc. Radiat. Transfer* 109, 1043
- Jolly A., Benilan Y., Fayt A., 2007, *J. Mol. Spectrosc.* 242, 46
- Jolly A., Fayt A., Benilan Y., et al., 2010, *ApJ* 714, 852
- Jura M., Balm S.P., Kahane C., 1995, *ApJ* 453, 721
- Kauppinen J., Jensen P., Brodersen S., 1980, *Journal of Molecular Spectroscopy* 83, 161
- Khelifi M., Paillous P., Delpech C., et al., 1995, *Journal of Molecular Spectroscopy* 174, 116
- Kwok S., 2000, *The Origin and Evolution of Planetary Nebulae*
- Latter W.B., 1991, *ApJ* 377, 187
- Lebouteiller V., Bernard-Salas J., Sloan G.C., Barry D.J., 2010, *PASP* 122, 231
- McEwan M.J., Scott G.B.I., Adams N.G., et al., 1999, *ApJ* 513, 287
- McNaughton D., Bruget D.N., 1991, *Journal of Molecular Spectroscopy* 150, 620
- Milam S.N., Woolf N.J., Ziurys L.M., 2009, *ApJ* 690, 837
- Morgan D.H., 1984, *MNRAS* 208, 633
- Morgan D.H., Parker Q.A., 1998, *MNRAS* 296, 921
- Rothman L.S., Gordon I.E., Barbe A., et al., 2009, *J. Quant. Spectrosc. Radiat. Transfer* 110, 533, cite for HITRAN 2008
- Sanduleak N., MacConnell D.J., Philip A.G.D., 1978, *PASP* 90, 621
- Shaw R.A., Stanghellini L., Villaver E., Mutchler M., 2006, *ApJS* 167, 201
- Skrutskie M.F., Cutri R.M., Stiening R., et al., 2006, *AJ* 131, 1163
- Snow T.P., Witt A.N., 1995, *Science* 270, 1455
- Speck A.K., Cami J., Markwick-Kemper C., et al., 2006, *ApJ* 650, 892
- Vassiliadis E., Wood P.R., 1993, *ApJ* 413, 641
- Waters L.B.F.M., Cami J., de Jong T., et al., 1998, *Nature* 391, 868
- Werner M.W., Roellig T.L., Low F.J., et al., 2004, *ApJS* 154, 1

Western C.M., 2010, PGOPHER, a program for simulating rotational structure. University of Bristol, <http://pgopher.chm.bris.ac.uk/>

Woods P.M., Millar T.J., Herbst E., Zijlstra A.A., 2003, *A&A* 402, 189

Woods P.M., Millar T.J., Zijlstra A.A., Herbst E., 2002, *ApJL* 574, L167

You can check out any time you
like, but you can never leave.

Eagles, Hotel California

Chapter 4

A Detailed Study of the Mid-Infrared Spectrum of HR 4049

Submitted to:

The Astrophysical Journal

Abstract We present a detailed analysis of the mid-infrared spectrum of the peculiar evolved object HR 4049. The full Spitzer-IRS high-resolution spectrum shows a wealth of emission with prominent features from CO₂ and H₂O and possible contributions from HCN and OH. We model the molecular emission and find that it originates from a massive ($M \gtrsim 8 \times 10^{-3} M_{\odot}$), warm ($T \approx 500$ K) and radially extended gas disk that is optically thick at infrared wavelengths. We also report less enrichment in ¹⁷O and ¹⁸O than previously found and a comparison of the Spitzer observations to earlier data obtained by ISO-SWS reveals that the CO₂ flux has more than doubled in 10 years time, indicating active and ongoing chemical evolution in the circumbinary disk. If the gas originates from interaction between the stellar wind and the dust, this suggests that the dust is oxygen-rich in nature. We expect that the molecular gas plays a crucial role in the thermal properties of the circumbinary disk by allowing visible light to heat the dust and then trapping the infrared photons emitted by the dust. This strong greenhouse effect results in higher temperatures and a more homogeneous temperature structure in the disk.

4.1 Introduction

HR 4049 is considered the prototype for a class of evolved objects with peculiar properties. Their effective temperatures and luminosities suggest that they are in the post-asymptotic giant branch (post-AGB) phase of their evolution, but their evolutionary path may be severely affected by the presence of a companion (see Van Winckel et al., 1995, for a review). Indeed, their unusual properties all seem to result from stellar evolution in a binary system.

Like many of the members of this class, HR 4049 shows a significant infrared (IR) excess and ultraviolet (UV) deficit (Lamers et al., 1986), suggesting the presence of a massive circumbinary disk. This disk is the result of mass loss in the binary system and plays a significant role in its unusual properties. For instance, the photospheric abundances of HR 4049 show an extreme depletion in refractory elements (e.g. $[\text{Fe}/\text{H}] = -4.8$, Waelkens et al., 1991b) while showing nearly solar abundances for volatiles (e.g. $[\text{S}/\text{H}] = -0.2$, $[\text{C}/\text{H}] = -0.2$, $[\text{N}/\text{H}] = 0.0$, $[\text{O}/\text{H}] = -0.3$ Takada-Hidai, 1990; Waelkens et al., 1991b). This peculiar depletion pattern is the result of dust formation in the disk followed by accretion of the gas which is now devoid of refractory elements (Mathis & Lamers, 1992; Waters et al., 1992). The circumbinary disk also causes HR 4049 to display photometric variability which is tied to its orbital period (Waelkens et al., 1991b).

Due to its importance in defining the characteristics of HR 4049, the dust component of the circumbinary disk has been the subject of a number of studies (e.g. Waelkens et al., 1991a; Dominik et al., 2003; Acke et al., 2013), revealing unusual dust properties. The infrared spectrum of HR 4049 does not show the dust features typically associated with circumstellar material around evolved stars (e.g. silicates or SiC) and thus the nature of the dust remains a mystery. Instead, the infrared excess is well-represented by a single temperature ($T \approx 1150$ K) blackbody from the onset of dust emission in the near-IR to submillimeter (submm) wavelengths. At the same time, the dust re-emits a significant fraction of the total stellar luminosity ($L_{\text{IR}} \approx L_*/3$), from which Dominik et al. (2003) deduced that HR 4049 is surrounded by an extremely optically thick and vertically extended disk with a hot inner wall. In this so-called “wall model”, the inner rim of the disk is 10 AU from the center of the binary system with a scale height of 3 AU and a temperature of 1150 ± 150 K.

However, Acke et al. (2013) found that the wall model was inconsistent with interferometric observations of HR 4049 which showed a radially extended disk. Instead, they proposed an optically thin dust disk composed of minerals without strong dust features—amorphous carbon being the most probable. In their model, the dust is slightly further from the center of the system and extends to much larger scale heights. Their model does not fit the spectral energy distribution (SED) beyond $20 \mu\text{m}$, so they included a dust component composed of large grains at 200 K.

One potential clue to the nature of the dust (and the evolutionary status of the system) is the presence of strong emission features due to polycyclic aromatic hydrocarbons (PAHs, see Waters et al., 1989; Tielens, 2008) as well as from nano-diamonds at 3.43 and $3.53 \mu\text{m}$ (Geballe et al., 1989; Guillois et al., 1999) and C_{60} (Roberts et al., 2012). Such species are often found in the environments surrounding evolved, carbon-rich objects, which suggests that HR 4049 was at some point a carbon star.

However, the IR spectrum also reveals a plethora of molecular bands from species that are more characteristic of oxygen-rich environments, but are very unusual nonetheless: Cami & Yamamura (2001) detected and identified the emission features due to all possible isotopologues of CO₂ containing ¹³C, ¹⁷O and ¹⁸O. Using optically thin models, they found that the gas was extremely enriched in ¹⁷O and ¹⁸O (with ¹⁶O/¹⁷O = 8.3 ± 2.3 and ¹⁶O/¹⁸O = 6.9 ± 0.9). Subsequently, Hinkle et al. (2007) analyzed the first overtone and fundamental bands of CO in the near-IR spectrum and found no enrichment in ¹⁷O and ¹⁸O. Although they detected CO isotopologues containing ¹⁷O and ¹⁸O in the fundamental, they did not observe these isotopologues in the overtone. They attributed the discrepancy between their oxygen abundances and those detected by Cami & Yamamura (2001) to the optically thick nature of the CO₂ emission in the mid-IR observations.

A detailed study of the gas has been difficult thus far due to the low sensitivity of the observations taken with the Short Wavelength Spectrometer on board the Infrared Space Observatory (ISO-SWS, de Graauw et al., 1996) as well as limitations in earlier line lists describing the transition energies and probabilities of the molecular species present in this spectrum. However, a good understanding of the gas composition should yield clues to the evolutionary history of this system as well as to the processing that occurs in these environments.

Here, we present observations from the Infrared Spectrograph (IRS, Houck et al., 2004) aboard the *Spitzer* Space Telescope (Werner et al., 2004) which have a higher signal-to-noise (S/N) ratio as well as better spectral resolution. As well, due to improvements in available line lists, we will be able to include the effects of optical depth in our spectral models.

In addition to the CO₂ bands, we analyze the other spectral features in the Spitzer-IRS and ISO-SWS spectra. We provide an inventory of the gas components and compare the observations to molecular model spectra to obtain excitation temperatures, column densities and optical depths. In turn, these numbers provide quantitative information on the gas disk which we compare to earlier studies of the dust in this object. We then compare our results from these analyses to the CO observations in the near-IR spectrum from Phoenix on Gemini in Malek & Cami (in preparation, hereafter Paper II).

This paper is organized as follows. In Section 4.2, we describe the observational data and reduction steps. We describe our modeling technique in Section 4.3 and present our results of this analysis in Section 4.4. Then we describe how these results fit with the other observations of the system in Section 4.5 and finally, we present our conclusions in Section 4.6.

4.2 Observations and Data Reduction

4.2.1 Spitzer-IRS

HR 4049 was observed at high spectral resolution ($R = 600$) using the Infrared Spectrograph (IRS, Houck et al., 2004) aboard the Spitzer Space Telescope (Werner et al., 2004) in the short high (SH, $\lambda = 9.9$ to $19.6 \mu\text{m}$) mode (AOR key 4900608; program ID 93; PI D. Cruikshank) and the long high (LH, $\lambda = 18.7$ to $37.2 \mu\text{m}$) mode (AOR key 23711232; program ID 40896; PI J. Cami). For the LH data, we also obtained background observations (AOR key 23711488).

We used the SMART data reduction package (v8.2.2, Higdon et al., 2004) as well as custom IDL routines to carry out the data reduction. Starting from the basic calibrated data (bcd), we first cleaned all data with IRSCLEAN using the campaign rogue pixel mask. When we examined the LH background observations, we found the background flux levels were fairly low (typically less than 1% of the target flux with some small unresolved spikes up to 5% of the target flux) and featureless. We thus subtracted this background from the target observations. We then combined the cleaned data collection events for each observation using a weighted average. Next, we extracted the spectra from the SH data and the background subtracted LH data using full aperture extraction in SMART v8.2.2 (Higdon et al., 2004).

We then defringed the extracted spectra and trimmed the edges of the orders. Flux differences between adjacent orders were typically on the order of 5% among the SH orders and only one LH order showed a notable flux difference. We scaled adjacent orders to the median flux in the overlap region, using order 11 ($\lambda_c = 18.7 \mu\text{m}$ for SH and $\lambda_c = 35.4 \mu\text{m}$ for LH) as the reference. We then compared the spectra in overlap regions as well as the two nod positions while checking for consistency, averaged them using a weighted mean, and rebinned the resulting final spectrum.

We compared the long wavelength end of the SH spectrum and the short wavelength end of the LH spectrum and calculated a weighted mean for the overlap region. Finally, we scaled the Spitzer-IRS spectrum to the Infrared Astronomical Satellite (IRAS) flux measurement at $25 \mu\text{m}$ (using a scale factor of 1.5). The final spectrum is presented in Fig. 4.1.

4.2.2 ISO-SWS

HR 4049 was observed twice with the Short Wavelength Spectrometer (SWS, de Graauw et al., 1996) aboard the Infrared Space Observatory (ISO, Kessler et al., 1996): on December 27th, 1995 (AOT 1, speed 1) and again on May 6th, 1996 (AOT 1, speed 2); both observations correspond to a resolving power of ~ 300 . Here, we use the speed 2 ISO-SWS data that was also presented by Cami & Yamamura (2001) and Dominik et al. (2003).

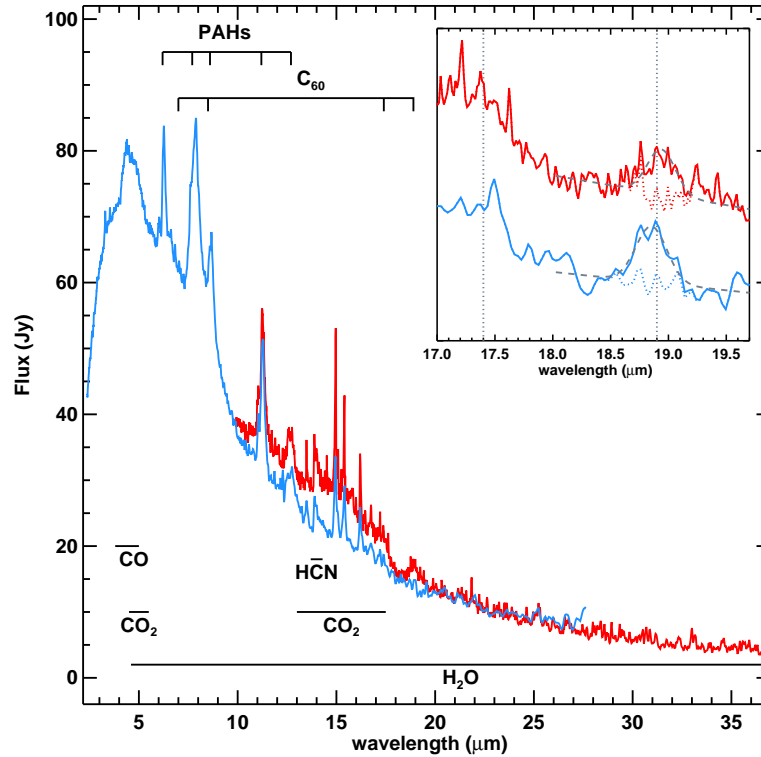


Figure 4.1: The Spitzer-IRS (red) and speed 2 ISO-SWS (blue) observations of HR 4049 are shown. The polycyclic aromatic hydrocarbon (PAH) bands at 6.2, 7.7, 8.6, 11.2 and 12.7 μm are highlighted as well as the positions of the C_{60} bands at 7.0, 8.5, 17.4 and 18.9 μm . The regions of the spectrum showing emission from CO, CO_2 , H_2O , and HCN are also highlighted. The inset shows the 17 to 19.5 μm region of the Spitzer-IRS (red) and speed 1 ISO-SWS spectra (blue) highlighting the locations of the 17.4 and 18.9 μm C_{60} bands and showing the best-fit Gaussians to the 18.9 μm bands (dashed grey lines) with the corresponding residuals for the fitting region (dotted lines).

We compare the speed 2 ISO-SWS spectrum to the Spitzer-IRS observations in Fig. 4.1. At the longer wavelengths, the spectra agree well with one another; however, the Spitzer-IRS data exhibit a significant increase in the flux levels between 10 and 18 μm .

4.3 Analysis

Fig. 4.1 shows the full Spitzer-IRS spectrum with emission from a variety of molecular species indicated. There are prominent features from large molecules such as polycyclic aromatic hydrocarbons (PAHs, Waters et al., 1989) and C_{60} (Roberts et al., 2012). We have also indicated the broad emission features from CO_2 at 15 μm , the HCN feature at 14 μm and the region of

the spectrum where we observe H₂O emission. There is also emission from CO and CO₂ at 4.6 and 4.2 μm respectively in the ISO-SWS spectrum.

4.3.1 Modeling the Spitzer Spectrum

To determine the properties of the gas in the mid-IR spectrum of HR 4049 and fully characterize the molecular emission, we created model spectra and compared them to the observational data. We used the same methods employed to build the SpectraFactory database (Cami et al., 2010b). For each model, we began with line lists detailing the frequencies and intensities of individual molecular transitions. We calculated optical depth profiles from the line lists assuming a population in local thermodynamic equilibrium (LTE) and a Gaussian intrinsic line profile with a width of 3 km s⁻¹. We summed the optical depth profiles for the different molecular species (including isotopologues) and then performed the proper radiative transfer calculations through an isothermal slab and smoothed the resulting model spectrum to match the SH resolution ($R = 600$).

We used a 1150 K blackbody for the continuum and applied a non-negative least-squares (NNLS) algorithm (Lawson & Hanson, 1974) with the continuum and the molecular emission models as parameters. Note that we treated the continuum and molecular emission components as additive terms, so the continuum is not being absorbed by the molecular layer and the two components represent different lines of sight. Then we compared our model to the observational data between 13.27 and 18 μm (to cover the CO₂ emission) and calculated χ^2_ν , the reduced χ^2 statistic for each model to determine the quality of the fit.

We experimented with several different models to determine the best range for each of our parameters then selected the parameters for each model using an adaptive mesh algorithm. In our final fits, we varied the temperature of the molecular layer between 200 and 1000 K in increments of 100 K and column densities between 10¹⁶ and 10²² cm⁻² in increments of $\log N = 0.2$ for all molecules in this region. Additionally, we varied $\log(^{12}\text{C}/^{13}\text{C})$ from 0 to 2; $\log(^{16}\text{O}/^{18}\text{O})$, $\log(^{16}\text{O}/^{17}\text{O})$, and $\log(^{14}\text{N}/^{15}\text{N})$ from 0 to 3 in increments of 0.2.

While we began fitting only CO₂ and its isotopologues, we later included H₂O and HCN in our model spectra. In addition, we noted a small linear trend in our residuals from 13 to 17.5 μm . We do not know the origin of this trend, but we incorporated a linear component in our NNLS routine to compensate for this residual.

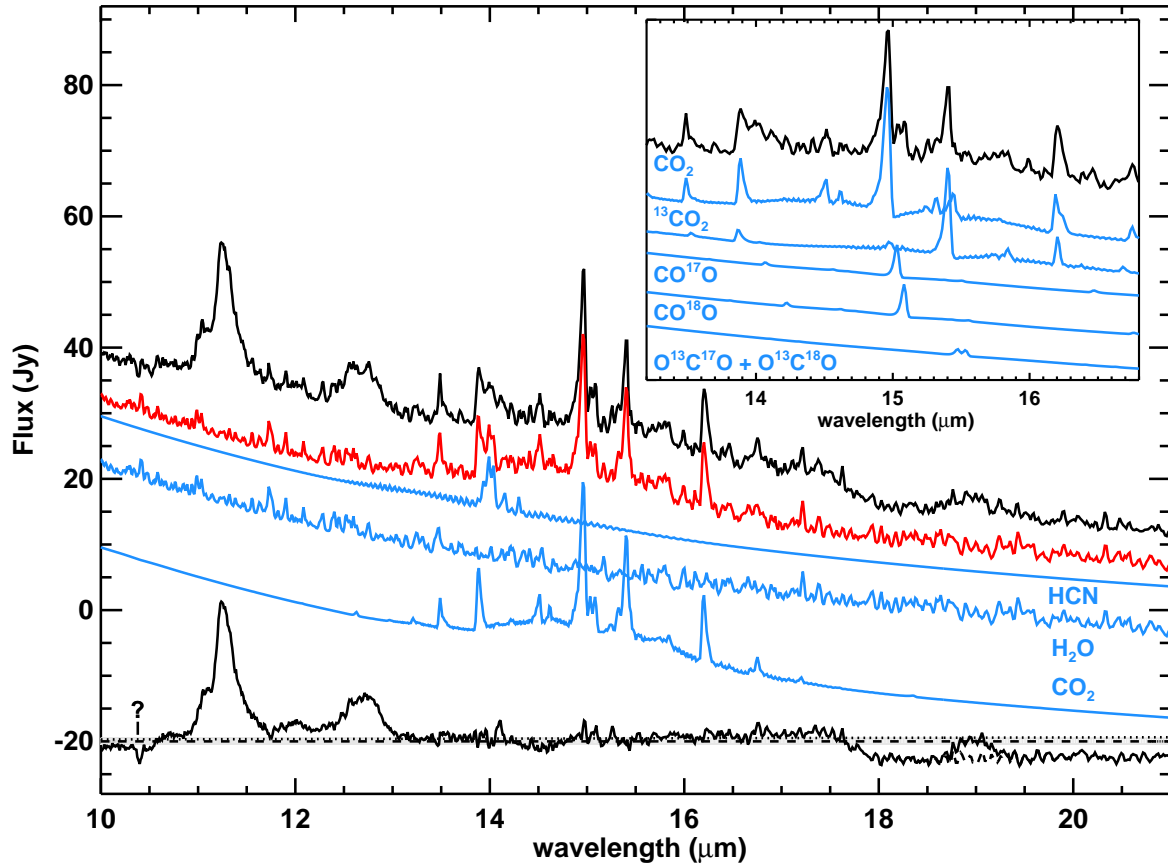


Figure 4.2: The Spitzer-IRS spectrum between 10 and 20 μm (black) with the best fit model for all the molecules (red) offset below the spectrum and models of the individual molecules below that (blue) in descending order: HCN, H_2O , and CO_2 . The residual without the linear component is shown at the bottom of the figure in black with the error values on the data indicated in light grey. We also fit a Gaussian to the C_{60} feature at 19 μm in the residual and show the effect of removing this Gaussian in dashed lines. The inset shows a breakdown of the CO_2 isotopologues between 13 and 17 μm .

4.4 Results

We present our parameters for our best fit model in Table 4.1 and the 10 to 20 μm region of the Spitzer-IRS spectrum with our best fit model in Fig. 4.2. We focus on the H_2O emission at LH wavelengths in Fig. 4.3 and we compare the models to the full spectrum Spitzer-IRS and our predictions at ISO-SWS wavelengths in Fig. 4.4. We find a χ^2_{ν} of 3.5 and a good representation of the molecular emission features within our fitting region.

When we compare the predictions from our model at longer and shorter wavelengths to the spectrum, we find that the spectral features are also fit remarkably well. The majority of

λ_{fit} (μm)	Spitzer-IRS 13.7–18	ISO-SWS 2.4–5.8; 9.5–10.5; 14–22
Temperature (K)	500 ± 50	600 ± 50
$\log N$ (CO_2)	19.0 ± 0.1	17.8 ± 0.1
$\log N$ (H_2O)	$21.6^{+0.1}_{-0.2}$	19.4 ± 0.1
$\log N$ (HCN)	17.8 ± 0.1	...
$\log N$ (CO)	...	22.0 ± 0.1
$^{12}\text{C}/^{13}\text{C}$	6^{+2}_{-1}	$1.6^{+2}_{-0.4}$
$^{16}\text{O}/^{17}\text{O}$	160^{+90}_{-35}	40^{+23}_{-9}
$^{16}\text{O}/^{18}\text{O}$	160^{+40}_{-60}	16^{+4}_{-3}
$^{14}\text{N}/^{15}\text{N}$	13^{+3}_{-8}	...

Table 4.1: Temperatures, column densities, and isotope ratios for the best model fits to the data as well as the nominal 3σ uncertainties.

the molecular features in the LH spectrum, for example, appear to be from H_2O emission. In addition, the spikes on the PAH features at 11.2 and 12.7 μm disappear and some of the smaller PAH features become evident.

4.4.1 CO_2

The Spitzer-IRS spectrum shows prominent emission from the CO_2 isotopologues observed by Cami & Yamamura (2001) in addition to others (e.g. the $\text{O}^{13}\text{C}^{17}\text{O}$ and $\text{O}^{13}\text{C}^{18}\text{O}$ peaks which Cami & Yamamura (2001) were unable to separate due to the lower spectral resolution of ISO-SWS). To model the emission from CO_2 , we used line lists from the 1000 K Carbon Dioxide Spectroscopic Database (CDSD, Tashkun et al., 2003) including the $^{13}\text{CO}_2$, CO^{17}O , CO^{18}O , $\text{O}^{13}\text{C}^{17}\text{O}$, and $\text{O}^{13}\text{C}^{18}\text{O}$ isotopologues.

Though our single layer LTE model reproduces the majority of the CO_2 features very well, (see Fig. 4.2), we find that the best fit model tends to slightly overestimate the flux relative to the local continuum between 14.2 and 14.7 μm while underestimating the flux between 16.7 and 17.6 μm (which may be due to some contribution from C_{60} at the long wavelength end). We also find high optical depths across most of our fit region with this model.

There are also small spikes which may be due to some slight temperature stratification in the CO_2 layer. For example, we note some residual flux at 16.64 μm which could be due to the transition between the $4\nu_2^4$ and $3\nu_2^1$ levels, which suggests the presence of additional hotter

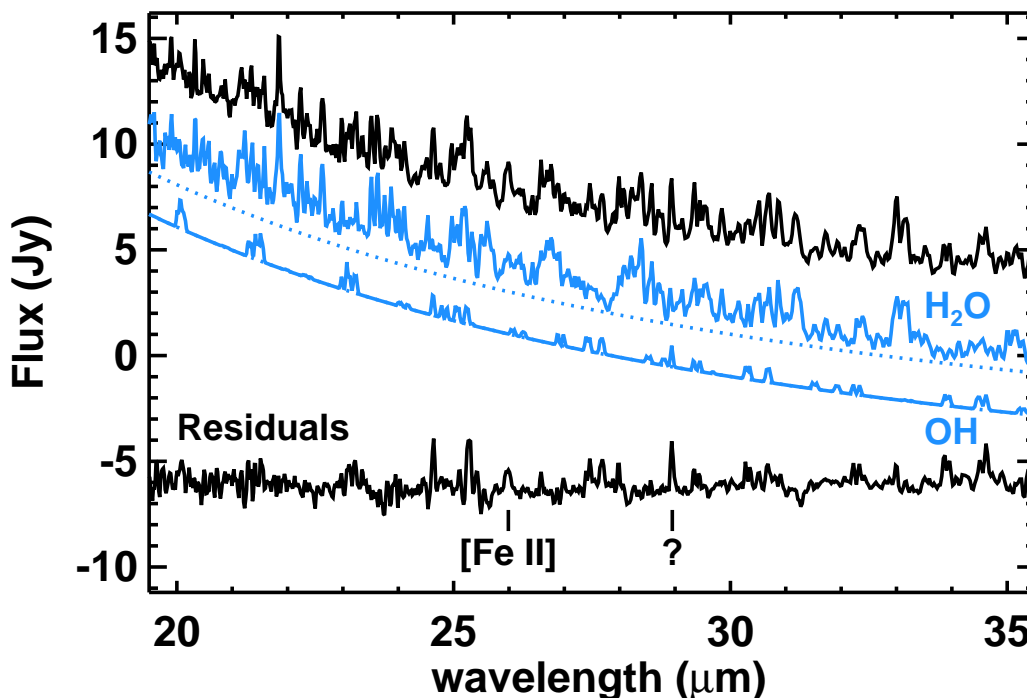


Figure 4.3: The Spitzer-IRS spectrum of HR 4049 (black) with the best fit model for H₂O and a model for OH at the same temperature and column density offset below the spectrum (blue). The dotted blue lines indicate the blackbody continuum under the H₂O and OH models.

gas. We also observe a small residual peak at 14.98 μm near the main CO₂ band, which is a combination of the ν_2 bending mode at 14.98 μm ($1\nu_2^1$ to the ground state) and subsequent hot bands which are each shifted slightly to the blue; the presence of residual emission at 14.98 μm thus suggests the presence of some colder CO₂. The high optical depths of the gas could make the appearance of the bands more sensitive to these types of temperature variations; however, these residuals are relatively small, suggesting that most of the emission originates from a relatively thermally homogeneous layer.

We also note some small residual emission at 15.04 and 15.10 μm , which could be due to additional emission from the main ν_2 bands of the OC¹⁷O and OC¹⁸O isotopologues respectively.

4.4.2 H₂O and OH

After including all CO₂ isotopologues in our models, many weaker emission features remained in the residuals of this region. We noticed that several features are consistent with emission

from water vapor. Thus, we re-calculated our models including optical depth profiles for H₂O using line lists from Partridge & Schwenke (1997, including the H₂¹⁷O, and H₂¹⁸O isotopologues).

We find an extremely high column density for H₂O and a much better correspondence to the results than for CO₂, not only in the region we chose to fit, but also at longer and shorter wavelengths in the Spitzer-IRS spectrum. Upon careful examination of the residuals in Fig. 4.2, one may note that the spikes atop the 11.2 and 12.7 μm PAH features disappear almost completely and remarkably, the 12 μm PAH feature becomes apparent though it was previously hidden by H₂O emission. Furthermore, the 18.9 μm C₆₀ feature becomes much more prominent and clear when H₂O emission is removed. In Figs. 4.3 and 4.4, it is also clear that H₂O accounts for the bulk of the features in the LH spectrum since the residuals contain relatively few remaining spectral features. This observation also confirms the earlier detection of water in HR 4049 in the near-IR by Hinkle et al. (2007).

Since OH was also detected by Hinkle et al. (2007) at ~3μm, and since it has many features in this wavelength range, we included it in our models between 13.24 and 18 μm. However, we were unable to detect OH in this region of the spectrum. We were also unable to fit any OH using only H₂O and OH between 20 and 35 μm. In Fig. 4.3, we show a comparison between model spectra of H₂O and OH using the same temperatures and column densities at LH wavelengths. We note that while there appear to be many features in our residuals which are consistent with emission from OH, it is not possible to reliably fit the OH features due to extensive contamination from H₂O.

4.4.3 HCN

When all the CO₂ and H₂O isotopologues are included in our models, there is still significant residual emission at 14.04 μm, where the CH bending mode of HCN is often seen in evolved stars. Indeed, the SpectraFactory catalogue (Cami et al., 2010b) reveals a clear HCN molecular band at this wavelength, thus we include it in our model calculations using line lists from the HITRAN 2008 database (Rothman et al., 2009, including the H¹³CN and HC¹⁵N isotopologues).

We determine a column density for HCN which is much lower than that of CO₂ and H₂O ($\log N = 17.8$), which suggests that it is less abundant. We included isotopologues of HCN containing ¹³C and ¹⁵N which appear slightly to the red of the main isotopologue and are thus able to find ¹⁴N/¹⁵N of 13_{-5}^{+3} . With only one band containing this isotope though, we do not consider our ratio here to be especially reliable.

4.4.4 Fullerenes

Since its detection in the young planetary nebula Tc 1 by Cami et al. (2010a), C_{60} has been reported in other evolved binary systems (Gielen et al., 2011b) and it was recently reported in HR 4049 by Roberts et al. (2012), who detected the 17.4 and 18.9 μm features.

Indeed, the 18.9 μm feature is clear (and also present in the ISO-SWS speed 1 observations, see the inset of Fig. 4.1) and when we subtract our best fit H_2O model, the feature becomes much more prominent (see Fig. 4.2). Fitting the 18.9 μm C_{60} feature in the residual spectrum with a Gaussian, we determine a FWHM of 0.40 μm and a central wavelength of 18.98 μm . This is a much narrower band than found by Roberts et al. (2012), who reported a FWHM of 0.64 μm . This difference may be due to the presence of the water features, which makes the band appear broader.

The 17.4 μm feature is buried in the optically thick CO_2 emission, so we cannot measure it accurately. Additionally, since no observations were taken by the IRS short low (SL; $R = 90$ to 127, $\lambda = 5.2$ to 14.5 μm) mode, the 7 and 8.5 μm features for C_{60} would only appear in the ISO-SWS spectrum. However, we do not see them, which could be due to a combination of the sensitivity of ISO-SWS and the often weak nature of these features.

4.4.5 PAHs

The spectral region covered by the Spitzer-IRS observations covers only the 11.2 and 12.7 μm PAH features. These bands also appear in the ISO-SWS spectrum alongside features at 6.2, 7.7 and 8.6 μm . The PAH features in the ISO-SWS spectrum of HR 4049 were described in detail by Beintema et al. (1996) and Molster et al. (1996) and are class B (Peeters et al., 2002).

Examining the residual spectra (see Fig. 4.2 especially), we note that some of the less prominent PAH features become clear when the H_2O emission is removed from the spectrum. For instance, the 12 μm feature from CH out-of-plane duo-modes and the weak, broad feature at 10.7 μm from PAH cations (Hony et al., 2001) are not clear in the original spectrum, but stand out in the residual. In addition, we find that the profiles of the already prominent PAH features become clearer when the H_2O emission is removed.

4.4.6 Residual Features

There are a few interesting features in the residual spectrum. For instance, we note a small absorption feature at 10.38 μm . This feature was previously observed in the carbon-rich pre-planetary nebula SMP LMC 11 by Malek et al. (2012), who suggested that this feature is molecular in nature, but they were unable to identify the carrier.

As described above, a few of the residual features in the LH spectrum may be due to OH emission. However, we also observe an emission feature at $25.99 \mu\text{m}$ which could be due to a fine-structure line from [Fe II] (see Fig. 4.3). To confirm that this feature is real, we examined the background observations and determined that this region of the spectrum was featureless. Then we examined both nod positions in the background-subtracted spectrum and noted that it appeared in both.

This transition is from the $J=7/2$ to $J=9/2$ (ground) level in the a^6D state. The next transition would appear at $35.35 \mu\text{m}$ ($J=5/2$ to $J=7/2$), but we do not observe a clear feature from this line. Instead, we observe a large and broad spike which appears to be from noise (S/N decreases toward the end of the LH spectrum). If we assume that the [Fe II] is at the same temperature as the molecular layer (500 K), we can estimate the strength of the expected emission at $35.35 \mu\text{m}$. Using the method described in Justtanont et al. (1999), we find that the $35.35 \mu\text{m}$ line should be 80% as strong as the $25.99 \mu\text{m}$ line, which could be hidden by this spike in the noise.

Plateau Emission In addition to the small emission features in our residuals, we note that we are unable to properly reproduce the continuum beyond $\sim 17.6 \mu\text{m}$. Indeed, examining Figs. 4.2 and 4.4, we see that we systematically overestimate the continuum emission at LH wavelengths. As well, we note that one of the major differences between the Spitzer-IRS and ISO-SWS spectra in Fig. 4.1 is the presence of emission from a continuum-like “plateau” under the CO_2 emission in the Spitzer spectrum between about 13 and $17.5 \mu\text{m}$.

We are unable to properly fit this emission plateau using our models. If we force the dust continuum to represent the LH continuum more accurately, we find that our models cease to reproduce the narrow emission bands from CO_2 . If we instead fit the narrow emission features, we overestimate the dust continuum at LH wavelengths. We have chosen to use a model which reproduces the narrow CO_2 features, but we note that the dust continuum from our best fit model is much higher than it should be as a result.

Part of this plateau emission is likely due to the presence of C_{60} . However, since the residual flux is much wider than the $17.4 \mu\text{m}$ C_{60} feature, this will not account for all of this plateau. In addition, the carrier of this plateau emission appears to have formed between the observations by ISO and Spitzer since this is perhaps the most obvious difference between the two spectra. We therefore considered two possible sources for this plateau emission.

First, we considered the possibility that this could be due to broad PAH emission from C-C-C bending modes, which has been observed to form a continuum between 15 and $20 \mu\text{m}$ (e.g. Van Kerckhoven et al., 2000; Boersma et al., 2010). These PAH plateaus also often show narrow features at 16.4, 17.4 and $18.9 \mu\text{m}$ along with a weak $15.8 \mu\text{m}$ feature (Tielens et al., 1999; Moutou et al., 2000). However, we do not see any obvious PAH features to the red of the

12.7 μm feature. Therefore, we consider it unlikely that this plateau is due to PAH emission.

Another possible candidate for this plateau emission is CO_2 . While our CO_2 models predict some continuum-like emission, it is not enough to match the plateau we observe. We do find high optical depths for CO_2 ($\tau_{\text{max}} \approx 160$ for the main isotopologue using a line width of 3 km s^{-1} , this would decrease to $\tau_{\text{max}} \approx 52$ for 10 km s^{-1}) as well as some evidence for temperature stratification in the residuals and possibly recent CO_2 formation which could result in some non-LTE emission. We therefore consider that the plateau emission could be due to CO_2 emission that our models are unable to fit properly. We will explore this possibility further in Section 4.5.4. We note that a similar plateau was also observed in IRAS 06338 (Gielen et al., 2011b) and was attributed to optically thick CO_2 emission.

4.4.7 ISO Spectrum

CO_2 , H_2O and HCN potentially all have features at the shorter wavelengths covered by ISO-SWS in addition to the features we observe in the Spitzer-IRS spectrum. We thus decided to compare the predictions from our model at these wavelengths to the ISO-SWS spectrum. We extended our model spectra to shorter wavelengths and smoothed the spectrum covered only by the ISO-SWS spectrum to a resolution of 300 to match these data. We present our prediction for these bands in the main plot of Fig. 4.4.

These predictions do not appear to fit the ISO-SWS spectrum on first sight. However, some of the features do appear to be reproduced. Examining the CO_2 feature at $4.2 \mu\text{m}$, we note that this band is heavily blended with the much broader CO emission band at $4.6 \mu\text{m}$. It appears, however, that the CO_2 feature within this broader band is reproduced reasonably well.

If we examine our predictions for the H_2O spectrum, there is a broad emission feature between 5 and $8 \mu\text{m}$. It is difficult to assess how well this broad band reproduces the spectrum in these regions due to the presence of the CO emission feature and the PAH features. However, our model predicts a fairly strong H_2O feature at $6.62 \mu\text{m}$ which is much weaker in the ISO-SWS spectrum.

Finally, although HCN also has an overtone mode at $\sim 7 \mu\text{m}$, our models do not predict it at these temperatures and column densities.

Since the ISO-SWS spectrum has a much larger wavelength coverage, it covers additional molecular bands (such as the $4.2 \mu\text{m}$ CO_2 feature) and species (CO at $4.6 \mu\text{m}$), so we decided to fit this spectrum as well. We used the same techniques described for fitting the Spitzer-IRS spectrum, but we included CO in our model (using line lists from Goorvitch, 1994, including the ^{13}CO , C^{17}O and C^{18}O isotopologues) and excluded HCN. We fit the spectrum in several regions to include as many molecular features as possible while excluding features we cannot

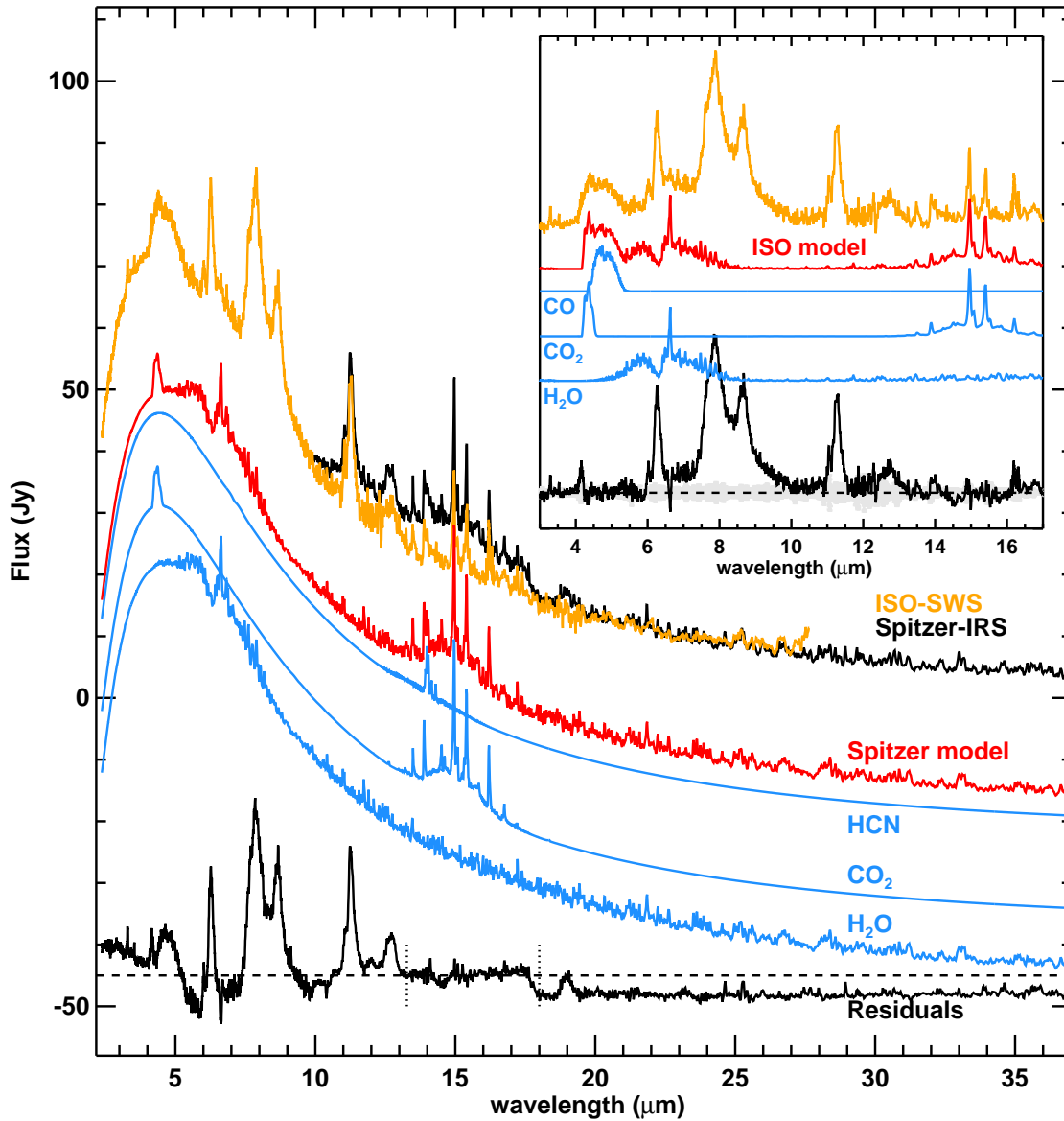


Figure 4.4: Main plot: Spitzer-IRS spectrum (black) and ISO-SWS spectrum (orange) for HR 4049 with the best fit model (red) to the Spitzer-IRS spectrum and individual components for CO_2 , H_2O , and HCN offset below the spectrum (blue) as well as the residuals (black). The vertical dotted lines indicate the region of the spectrum used to fit the model to the Spitzer-IRS data. The model outside of these wavelength ranges (including the ISO-SWS spectrum) is the prediction based on these best fit parameters. Inset: Model fit to the ISO-SWS spectrum, with the best fit model (red) and individual components for CO, CO_2 and H_2O offset below the spectrum (blue). The residuals for this model are shown in black and the uncertainties in the data are shown in light grey.

fit (e.g. the PAHs). Thus, we used three fitting regions, first, between 2.4 and 5.8 μm , then from 9.5 to 10.5 μm and finally from 14 to 22 μm .

The parameters for our best fit are presented in Table 4.1 and this model is compared to the 3 to 17 μm region of the ISO-SWS spectrum in the inset of Fig. 4.4. In our direct fit to the ISO-SWS spectrum, we find that the fit in the 4 μm region is greatly improved with the addition of CO and a more appropriate scaling factor for the continuum. However, we note that there are still issues in the H₂O emission at 6.62 μm where we fit a large emission spike which does not appear in the spectrum. In addition, there are some residuals at $\sim 16 \mu\text{m}$.

Time dependence When we compare the ISO-SWS and Spitzer observations, we find that there is a dramatic increase in emission between 10 and 18 μm . If we subtract a 1150 K blackbody continuum from each spectrum and integrate the remaining flux between 13.4 and 16.8 μm , we find that the flux from molecular emission has more than doubled in this region between the time of the ISO and Spitzer observations (from $\sim 2 \times 10^{-26} \text{ W m}^2$ to $\sim 5 \times 10^{-26} \text{ W m}^2$).

4.5 Discussion

The better quality of the Spitzer-IRS data and current line lists allow a much more in-depth analysis of the gas than was previously possible. As we shall see, many of the results of this analysis have important consequences for the properties of the circumbinary disk.

4.5.1 Isotopic Ratios

We remind the reader that Cami & Yamamura (2001) assumed optically thin emission from CO₂ and determined that HR 4049 was extremely enriched in ¹⁷O and ¹⁸O (¹⁶O/¹⁷O = 8.3 ± 2.3 ; ¹⁶O/¹⁸O = 6.9 ± 0.9). In a subsequent study of the near-IR CO bands, Hinkle et al. (2007) found isotopic ratios consistent with solar values and they suggested that the ratios determined by Cami & Yamamura (2001) were incorrect because the CO₂ emission in HR 4049 is actually optically thick. Based on our models, we are able to confirm the suggestion by Hinkle et al. (2007) that the CO₂ is optically thick, but we determine a ratio of 160^{+90}_{-35} for ¹⁶O/¹⁷O and 160^{+40}_{-60} for ¹⁶O/¹⁸O, indicating some enrichment in ¹⁷O and ¹⁸O relative to solar values (¹⁶O/¹⁷O = 2700, ¹⁶O/¹⁸O = 479, Anders & Grevesse (1989); Scott et al. (2006)). In addition, these isotopes are enriched relative to typical AGB stars (where both are on the order of a 10² to 10³, see Harris & Lambert, 1984; Harris et al., 1985b, 1987, 1988; Smith & Lambert, 1990). Indeed, the enrichment of ¹⁷O and ¹⁸O in HR 4049 appears to be similar to that of the Ba star

HD 101013 ($^{16}\text{O}/^{17}\text{O} = 100_{-50}^{+100}$, $^{16}\text{O}/^{18}\text{O} = 60_{-30}^{+100}$, Harris et al., 1985a).

There are also recent detections of OC ^{18}O in two other binary post-AGB objects: EP Lyr and HD 52961 which both show enrichment in ^{18}O ($^{16}\text{O}/^{18}\text{O}$ of 19 for EP Lyr and 100 for HD 52961, Gielen et al., 2009). As well as a study of ^{18}O enrichment in R Coronae Borealis stars in which $^{16}\text{O}/^{18}\text{O}$ ratios less than one were found (Clayton et al., 2007).

We also note that the values we find here for the enrichment of ^{17}O and ^{18}O are more suitable to the scenario proposed by Lugaro et al. (2005) who suggested that the isotopic ratios for oxygen in HR 4049 could be due to nova nucleosynthesis; though HR 4049 lacks the UV flux for a typical white dwarf companion (Monier & Parthasarathy, 1999). However, due to the high optical depths we find, our values are poorly determined and our uncertainties on these values are likely to be larger than we find from our models. We also suggest that there may be similar issues with the $^{16}\text{O}/^{18}\text{O}$ values in the other post-AGB objects for the same reason.

Our best fit models appear to indicate an enrichment in ^{13}C , with $^{12}\text{C}/^{13}\text{C}$ of 6_{-1}^{+2} . This relatively low value agrees with an early termination of the AGB due to accelerated mass loss along the orbital plane of the binary (Iben & Livio, 1993). This has been observed in other binary post-AGB objects such as EP Lyr (Gielen et al., 2008). Although we note that optically thick CO_2 emission also makes this ratio uncertain.

4.5.2 Gas Distribution and Disk Structure

From our models, we find that not only is the CO_2 emission optically thick, but the gas is optically thick across the entire spectrum (e.g. $\tau > 10$ for H_2O across the entire Spitzer-IRS spectrum). This has some very important ramifications. For instance, when the gas is optically thick, the flux will scale with the emitting area, thus we are able to estimate the spatial extent of the gas using our models.

When we calculate our models, we obtain a scale factor (f) which relates I_ν from our radiative transfer calculations to F_ν . We are able to relate this scale factor to the surface area (A) of the emitting layer such that $f = A/4D^2$, where D is the distance to HR 4049.

From our model fit to the Spitzer-IRS data, we find a value of 1.60×10^9 for f . If we use a distance of 640 pc for HR 4049 (as described by Acke et al., 2013), this scale factor corresponds to a projected area of 1117 AU^2 . If we perform the same analysis using our best fit to the ISO-SWS spectrum (with $f = 1.57 \times 10^9$), we find a projected area of 1097 AU^2 , which agrees reasonably well with the emitting region we estimate from our Spitzer-IRS data. Since the scale factors we determine have not changed much between the ISO and Spitzer observations despite the differences in column densities between the two models, this also supports our claim of optically thick gas.

If we then assume an inclination angle of 60° (which is agreed upon by both current models for the disk), we find an actual emitting surface of 1290 AU^2 for our molecular emission. If we consider how this surface area would fit into the current disk models, we note that this would not fit on the inner rim of the wall model.

This suggests that the gas belongs to a radially extended disk instead. If we assume that the gas exists some distance from the centre of the binary system, we can estimate the maximum extent of the disk. Were the gas to originate 10 AU from the binary (as the dust in the wall model, Dominik et al., 2003), it would extend to a distance of 23 AU. If the gas begins at 15 AU from the binary (based on the interferometric observations by Acke et al., 2013), it would extend to 25 AU, a distance which agrees well with the maximum radial extent of the disk determined from the interferometric observations by Acke et al. (2013).

It would be reasonable to suppose that the gas is mixed in with any dust in the circumbinary disk of HR 4049. As described by Dominik et al. (2003), dust grains in a gas-rich disk tend to settle toward the midplane of the disk, so the gas we observe could form a sort of atmosphere on the outside of the disk. There could also be more gas inside the disk which we are unable to observe since this atmosphere is optically thick. However, the gas on the inside of the disk could contribute to the opacity of the disk by providing some continuum-like emission similar to that we observe in our models.

As the LTE models reproduce the emission spectrum well and the gas appears to be reasonably warm (500 K), we find that we cannot reconcile our observations to a wall-type model for the dust. The wall model contains cold dust beyond the inner rim of the disk (Dominik et al., 2003), which would result in cold gas in this region. Instead, we observe a large region of warm gas, so we find this sort of model improbable.

It would also be difficult to reconcile our observations to the disk model presented by Acke et al. (2013) in which the dust is optically thin. Acke et al. (2013) include gas in their disk to determine the scale height, however CO_2 and H_2O are both excellent at trapping infrared radiation, especially at high column densities like those we observe in this disk and these effects are not included in their model.

Since these molecules are largely transparent at optical wavelengths, the stellar radiation will warm the dust grains. These grains will then re-emit this radiation in the infrared which will be absorbed and re-emitted by the gas in the disk, effectively trapping the radiation inside the disk. This will not only have the effect of warming the disk overall, but it will also keep the temperature relatively homogeneous throughout the disk. Thus the disk could have the sort of narrow temperature range suggested by Dominik et al. (2003), who determined that the SED of HR 4049 can be fit either by a 1150 K black body or by the sum of several equally weighted black bodies within a range of $880 \text{ K} \leq T \leq 1325 \text{ K}$.

However, in LTE, a gas cannot appear in emission in front of a hotter background source. Thus, we will explore alternate excitation mechanisms which could result in bands which emit in a way which appears similar to LTE in Section 4.5.4.

Furthermore, our findings that the PAH emission features are not obscured by the gas is consistent with the interferometric observations by Acke et al. (2013), which indicated that the region of PAH emission extends beyond the disk and into bipolar lobes. Were the PAHs confined to the disk, we should expect that the small PAH features, such as the one at $12 \mu\text{m}$ would not become apparent upon removal of our models.

4.5.3 Total Gas Mass

Using the projected size for the emitting region and our column densities, we can estimate the masses of the molecular species we observe in this system. Then, combining these with photospheric abundances, we can estimate a lower limit for the total mass of the gas in the circumbinary environment of HR 4049.

From our model fit to the Spitzer-IRS data, we calculate a mass of $9.19 \times 10^{-8} M_{\odot}$ for CO_2 , $1.50 \times 10^{-5} M_{\odot}$ for H_2O and $3.56 \times 10^{-9} M_{\odot}$ for HCN . Similarly, for the ISO-SWS model, we find masses of $5.69 \times 10^{-9} M_{\odot}$ for CO_2 , $9.28 \times 10^{-8} M_{\odot}$ for H_2O and $5.74 \times 10^{-5} M_{\odot}$ of CO .

Since the gas is oxygen-rich, we use the carbon abundance determined by Waelkens et al. (1991b, $\log N_C/N_H = 8.41 - 12$) along with the number of carbon-containing molecules and determine a lower limit for the total gas mass of $7.98 \times 10^{-3} M_{\odot}$ in the disk. This estimate is higher than the mass estimated by Dominik et al. (2003), who estimated $2.85 \times 10^{-4} M_{\odot}$ for the total mass of the disk. This could indicate a higher gas to dust ratio in the disk (they use a value of 100) or the presence of even more dust in this system than predicted by the wall model. If we compare our estimate for the gas mass to the dust mass from Acke et al. (2013, in which $M_{\text{dust}} = (1.0 \pm 0.4) \times 10^{-8} M_{\odot}$), we find a gas-to-dust ratio of approximately 10^6 . This appears unreasonably high, however this is the estimated mass for only the small grains in the disk, which are responsible for the near- and mid-IR SED as well as the optical extinction. Their model includes a cold dust component to reproduce the flux at far-IR and submm wavelengths, which could contain more mass.

Since the gas is optically thick, this estimate will not include all the gas in the system (e.g. any gas beyond the optically thick layer or on the side of the disk inclined away from us is not included). In addition, since the majority of the gas included in our estimate is CO which only appears in the ISO-SWS spectrum, this may not describe the current gas mass since, as we will describe presently, it appears there is significant ongoing gas formation in HR 4049.

4.5.4 Time Evolution

It is somewhat surprising to see that the CO₂ flux has increased by a factor of 2.5 between the ISO-SWS and Spitzer-IRS observations (see Section 4.4.7). Since we scaled the Spitzer-IRS observations to match the IRAS flux point at 25 μm, we considered that this could be an issue in our comparison of these observations. However, the ISO-SWS spectrum was also scaled to the same point so this is unlikely to change our observation. Furthermore, it is not just the flux that has changed under the CO₂ emission features, but also the shape of the “continuum” and features in this region. Thus, it appears that the change in the emission features is real.

We compared the phase between the two observations using the phase information from Bakker et al. (1998). The SH observations were taken at a phase (ϕ) of 0.844, while the ISO-SWS speed 2 observations were taken at $\phi = 0.041$, near the photometric minimum. There are also ISO-SWS speed 1 observations available, which were taken at a similar phase as the Spitzer-IRS observations ($\phi = 0.0738$).

We thus compared the two ISO-SWS observations to see if there was a change in this region of the spectrum which could be attributed to phase. When we did so, we found that the spectra of the speed 1 and speed 2 ISO-SWS observations were roughly the same within the uncertainty measurements on the fluxes.

Thus, we conclude that the amount of emitting CO₂ gas we can observe has increased between the observations of by ISO-SWS and those by Spitzer-IRS. If the gas were optically thin, this would imply that CO₂ has been forming at a rate of $3.68 \times 10^{-9} M_{\odot} \text{ yr}^{-1}$ assuming a constant formation rate. We note that this represents a considerable and rapid increase in CO₂ in the system, however, as we discovered, the CO₂ emission in the mid-IR spectrum is not optically thin so this represents a lower limit to the increase in CO₂. In addition, we cannot know whether the formation has been continuous between the observations so this is a relatively crude estimate for the formation rate.

While Bakker et al. (1996) reported a mass-loss rate from HR 4049 of $(6 \pm 4) \times 10^{-7} M_{\odot} \text{ yr}^{-1}$, the amount of carbon and oxygen in the stellar winds is insufficient to permit the formation of so much new material. Therefore, we consider that the CO₂ we observe is forming from the interaction between the stellar wind and the dust disk.

The ongoing formation of oxygen-rich gas thus requires that the dust contains an oxygen-rich component (e.g. silicates) and the absence of features from these dust species in the spectrum would therefore be due to obscuration of these features by optically thick gas; or by the dust being optically thick or perhaps being composed of large dust grains which have a smooth opacity. If the dust is primarily oxygen-rich, then HR 4049 would also be consistent with other post-AGB binaries in this regard (e.g. Gielen et al., 2011a).

While this may appear to be inconsistent with the fact that small grains are required to

explain the optical and UV extinction, it was noted by Dominik et al. (2003) that the extinction at short wavelengths and the IR excess do not need to be caused by the same population of dust grains. Thus, although the optical and UV extinction is described well by a population of small grains of amorphous carbon or metallic iron as described by Acke et al. (2013), these grains cannot be the only dust component in the disk since they cannot allow the formation of the oxygen-rich gas we observe here.

The presence of small carbonaceous grains in the upper region of the disk could thus contribute to the extinction at short wavelengths, while a population of oxygen-rich grains could contribute to part of the IR emission.

The evidence for ongoing formation of gas in the circumbinary disk of HR 4049 also suggests that the molecules are not actually in LTE, and the emission we observe may be due to pumping—either *radiative* pumping or *formation* pumping. In both cases, pumping results in a large fraction of molecules in highly excited vibrational states, either through absorption of higher energy photons (near-IR or even UV) or alternatively as a direct result of the formation of the molecules which leaves them in the excited states. After being pumped, they cascade down by fluorescent emission of the IR photons we observe. Pumping would thus always produce emission at mid-IR wavelengths even when in front of hot dust. Superficially, such emission spectra could resemble LTE models; their main difference would be the presence of many bands from higher vibrational levels. This could help explain the plateau emission as a forest of CO₂ emission lines from higher energies.

It is also possible that the CO₂ and H₂O could be radiatively pumped by absorbing stellar radiation, though this has yet to be directly observed. Note that these species have strong electronic absorption bands at UV wavelengths which could be the source of the pumping through absorption of stellar radiation. Given the high column densities of these species, it would be interesting to investigate whether this could be a contributing source of the observed UV deficit in HR 4049 (Lamers et al., 1986). Formation pumping is certainly an appealing alternative, but is not well studied. While models exist for the formation pumping of H₂ after formation on dust grain surfaces (e.g. Gough et al., 1996; Takahashi & Uehara, 2001), but to our knowledge no such models exist for CO₂ or H₂O.

Finally, we note that while it appears that gas has been forming in the disk of HR 4049, the overall emitting surface does not seem to have changed significantly (remaining at ~ 1300 AU²). This agrees very well with the idea that the disk is relatively stable and long-lived (also supported by the unchanging CO overtone absorption observed between the observations of Lambert et al. (1988) and those by Hinkle et al. (2007)).

Dominik et al. (2003) described how a gas-rich disk (such as the one we describe) would tend to settle toward the midplane and expand outward. Using a gas-to-dust ratio of 100 and an

initial scale height of 4 AU, they estimated that the scale height of the disk would decrease by half in 150 years. This effect could be mitigated by a higher gas-to-dust ratio and we suggest that the gas-to-dust ratio is likely to be greater than 100 in this environment. Indeed, if the dust is being slowly destroyed by stellar wind and gas is being formed, this ratio is likely to be increasing.

4.6 Conclusion

The Spitzer-IRS observations clearly reveal that the molecular gas in the circumbinary disk of HR 4049 is optically thick at infrared wavelengths and that the emission originates from a radially extended disk. The gas causes a strong greenhouse effect that plays a significant role in determining the thermal structure in the disk. Including the effect of optical depth, we determine that there is less of an enrichment in ^{17}O and ^{18}O than previously reported. Additionally, changes in the observed flux between ISO and Spitzer observations suggest ongoing chemical processing of oxygen-rich dust.

Bibliography

- Acke B., Degroote P., Lombaert R., et al., 2013, *A&A* 551, A76
- Anders E., Grevesse N., 1989, *Geochimica et Cosmochimica Acta* 53, 197
- Bakker E.J., Lambert D.L., Van Winckel H., et al., 1998, *A&A* 336, 263
- Bakker E.J., van der Wolf F.L.A., Lamers H.J.G.L.M., et al., 1996, *A&A* 306, 924
- Beintema D.A., van den Ancker M.E., Molster F.J., et al., 1996, *A&A* 315, L369
- Boersma C., Bauschlicher C.W., Allamandola L.J., et al., 2010, *A&A* 511, A32
- Cami J., Bernard-Salas J., Peeters E., Malek S.E., 2010a, *Science* 329, 1180
- Cami J., van Malderen R., Markwick A.J., 2010b, *ApJS* 187, 409
- Cami J., Yamamura I., 2001, *A&A* 367, L1
- Clayton G.C., Geballe T.R., Herwig F., Fryer C., Asplund M., 2007, *ApJ* 662, 1220
- de Graauw T., Haser L.N., Beintema D.A., et al., 1996, *A&A* 315, L49
- Dominik C., Dullemond C.P., Cami J., van Winckel H., 2003, *A&A* 397, 595
- Geballe T.R., Noll K.S., Whittet D.C.B., Waters L.B.F.M., 1989, *ApJL* 340, L29
- Gielen C., Bouwman J., van Winckel H., et al., 2011a, *A&A* 533, A99
- Gielen C., Cami J., Bouwman J., Peeters E., Min M., 2011b, *A&A* 536, A54
- Gielen C., van Winckel H., Matsuura M., et al., 2009, *A&A* 503, 843
- Gielen C., van Winckel H., Min M., Waters L.B.F.M., Lloyd Evans T., 2008, *A&A* 490, 725
- Goorvitch D., 1994, *ApJS* 95, 535
- Gough S., Schermann C., Pichou F., et al., 1996, *A&A* 305, 687
- Guillois O., Ledoux G., Reynaud C., 1999, *ApJL* 521, L133
- Harris M.J., Lambert D.L., 1984, *ApJ* 285, 674

- Harris M.J., Lambert D.L., Hinkle K.H., Gustafsson B., Eriksson K., 1987, *ApJ* 316, 294
- Harris M.J., Lambert D.L., Smith V.V., 1985a, *ApJ* 292, 620
- Harris M.J., Lambert D.L., Smith V.V., 1985b, *ApJ* 299, 375
- Harris M.J., Lambert D.L., Smith V.V., 1988, *ApJ* 325, 768
- Higdon S.J.U., Devost D., Higdon J.L., et al., 2004, *PASP* 116, 975
- Hinkle K.H., Brittain S.D., Lambert D.L., 2007, *ApJ* 664, 501
- Hony S., Van Kerckhoven C., Peeters E., et al., 2001, *A&A* 370, 1030
- Houck J.R., Roellig T.L., van Cleve J., et al., 2004, *ApJS* 154, 18
- Iben, Jr. I., Livio M., 1993, *PASP* 105, 1373
- Justtanont K., Tielens A.G.G.M., de Jong T., et al., 1999, *A&A* 345, 605
- Kessler M.F., Steinz J.A., Anderegg M.E., et al., 1996, *A&A* 315, L27
- Lambert D.L., Hinkle K.H., Luck R.E., 1988, *ApJ* 333, 917
- Lamers H.J.G.L.M., Waters L.B.F.M., Garmany C.D., Perez M.R., Waelkens C., 1986, *A&A* 154, L20
- Lawson C.L., Hanson R.J., 1974, Solving least squares problems
- Lugaro M., Pols O., Karakas A.I., Tout C.A., 2005, *Nuclear Physics A* 758, 725
- Malek S.E., Cami J., Bernard-Salas J., 2012, *ApJ* 744, 16
- Mathis J.S., Lamers H.J.G.L.M., 1992, *A&A* 259, L39
- Molster F.J., van den Ancker M.E., Tielens A.G.G.M., et al., 1996, *A&A* 315, L373
- Monier R., Parthasarathy M., 1999, *A&A* 341, 117
- Moutou C., Verstraete L., Léger A., Sellgren K., Schmidt W., 2000, *A&A* 354, L17
- Partridge H., Schwenke D., 1997, "*Journal of Chemical Physics*" 106, 4618
- Peeters E., Hony S., Van Kerckhoven C., et al., 2002, *A&A* 390, 1089
- Roberts K.R.G., Smith K.T., Sarre P.J., 2012, *MNRAS* 421, 3277
- Rothman L.S., Gordon I.E., Barbe A., et al., 2009, *J. Quant. Spectrosc. Radiat. Transfer* 110, 533, cite for HITRAN 2008
- Scott P.C., Asplund M., Grevesse N., Sauval A.J., 2006, *A&A* 456, 675
- Smith V.V., Lambert D.L., 1990, *ApJS* 72, 387

- Takada-Hidai M., 1990, *PASP* 102, 139
- Takahashi J., Uehara H., 2001, *ApJ* 561, 843
- Tashkun S.A., Perevalov V., Teffo J.L., D. L.N., 2003, *Journal of Quantitative Spectroscopy and Radiative Transfer* 82, 165
- Tielens A.G.G.M., 2008, *ARA&A* 46, 289
- Tielens A.G.G.M., Hony S., van Kerckhoven C., Peeters E., 1999, In: Cox P., Kessler M. (eds.), *The Universe as Seen by ISO*, vol. 427 of *ESA Special Publication*, p. 579
- Van Kerckhoven C., Hony S., Peeters E., et al., 2000, *A&A* 357, 1013
- Van Winckel H., Waelkens C., Waters L.B.F.M., 1995, *A&A* 293, L25
- Waelkens C., Lamers H.J.G.L.M., Waters L.B.F.M., et al., 1991a, *A&A* 242, 433
- Waelkens C., Van Winckel H., Bogaert E., Trams N.R., 1991b, *A&A* 251, 495
- Waters L.B.F.M., Lamers H.J.G.L.M., Snow T.P., et al., 1989, *A&A* 211, 208
- Waters L.B.F.M., Trams N.R., Waelkens C., 1992, *A&A* 262, L37
- Werner M.W., Roellig T.L., Low F.J., et al., 2004, *ApJS* 154, 1

Chapter 5

A Detailed study of the Near-Infrared Spectrum of HR 4049

To be submitted to:

The Astrophysical Journal

Abstract: HR 4049 is a peculiar evolved binary which is surrounded by a circumbinary disk. Mid-infrared observations show that the disk is rich in molecular gas and radially extended. To study the properties of this disk, we re-analyzed a set of near-infrared observations at high spectral resolution obtained with Gemini-Phoenix. These data cover absorption lines originating from the first overtone of CO and H₂O in the 2.3 μm region as well as more complex emission-absorption profiles from H₂O and the fundamental mode of CO near 4.6 μm . By using an excitation diagram and from modeling the spectrum, we find that most of the CO overtone and H₂O absorption originates from hot gas ($T_{\text{ex}} \approx 1000 \text{ K}$) with high column densities, consistent with mid-IR data. The strong emission in the wavelength range of the CO fundamental furthermore suggests that there is a significant quantity of gas in the inner cavity of the disk. In addition, there is a much colder component in the line of sight to the disk. A detailed analysis of the overtone line profiles reveals variations in the line widths which are consistent with a radially extended disk in Keplerian rotation with the hotter gas located closer to the central star. Finally, we estimate the mass of the primary to be $\sim 0.34 M_{\odot}$ and discuss the implications for its evolutionary status.

5.1 Introduction

HR 4049 is considered the prototype for a class of evolved binaries with peculiar properties. The effective temperatures and luminosities of the members of this class suggest that they are in the post-asymptotic giant branch (post-AGB) phase of their evolution, but their evolutionary

path is thought to be severely affected by the presence of a close companion (see Van Winckel et al., 1995, for a review).

Like the other members of its class, HR 4049 shows a significant infrared (IR) excess and a time-variable optical and ultraviolet (UV) deficit (Lamers et al., 1986), which suggests the presence of a massive circumbinary disk. In addition, its photosphere shows a severe depletion in refractory elements, but it has roughly solar abundances in volatiles. This unusual depletion pattern is generally attributed to the formation of dust (incorporating refractory elements) in a circumbinary disk, followed by the re-accretion of the depleted gas onto the star (Mathis & Lamers, 1992; Waters et al., 1992).

Due to the important role the circumbinary disk plays in determining the properties of HR 4049, it has been extensively studied (e.g. Waelkens et al., 1991; Dominik et al., 2003; Acke et al., 2013). While the IR excess is a clear indication of the presence of dust in a stable disk around the system, it has been difficult to determine the nature of the dust in the disk. Indeed, it is not even clear whether the dust in the disk is oxygen-rich or carbon-rich. While the IR spectrum shows the clear presence of gas that is typically associated with oxygen-rich environments (e.g. CO₂, H₂O, OH; Cami & Yamamura, 2001; Hinkle et al., 2007; Malek & Cami, submitted to ApJ, hereafter Paper I) there is no trace of corresponding oxygen-rich dust features such as silicates or oxides. Instead, the spectral energy distribution (SED) of the disk resembles a 1150 K blackbody down to sub-millimeter wavelengths (Dominik et al., 2003), while also showing strong emission features due to polycyclic aromatic hydrocarbons (PAHs) which originate not from the disk, but from what appears to be bipolar lobes (Acke et al., 2013).

The 1150 K blackbody SED can be reproduced by a “wall model”, in which the circumbinary disk is vertically extended and the dust is very optically thick, effectively producing a radiating inner wall at a temperature of 1150 ± 150 K, with a scale height of ~ 3 AU at the inner wall distance of 10 AU (Dominik et al., 2003). Because of the high opacity, the dust beyond the inner rim is cold and does not contribute to the IR excess. However, the wall model has been challenged by recent interferometric observations that show a more extended distribution of material emitting strongly in the IR than the wall model can accommodate (Acke et al., 2013). Instead, these authors suggest emission from optically thin dust with smooth opacity profiles.

In Paper I, we present a detailed analysis of the molecular emission in the mid-IR spectrum and conclude that neither of these models is fully consistent with the properties of the molecular gas (in particular CO₂, H₂O and CO). Indeed, while we find that the gas originates from a radially extended, disk, we also determine that it is very optically thick across most of the mid-IR. Radiative trapping by this optically thick gas then results in a more homogeneous temperature structure than previously considered for the disk.

Additional clues to the geometry and properties of the disk can be inferred from observa-

tions in the near-IR at high spectral resolution. Hinkle et al. (2007) presented such observations, examining three regions of the near-IR spectrum of HR 4049 at 2.3, 3.0 and 4.6 μm . They detect many CO, OH and H₂O lines and identify distinct components in the system. They propose that absorption in the CO overtone originates from gas in Keplerian rotation along the inner rim of the disk in the wall model. Furthermore, they suggest that the gas is slowly streaming out over the edge of the wall and over the disk, causing the more complex emission-absorption line profiles in the 4.6 μm region. Finally, they found evidence for a cold gas component.

Clearly, the near-IR observations contain a lot of information about the the properties, geometry and kinematics of the gas disk. It is thus important to investigate whether we can reconcile these data with the disk model inferred from mid-IR observations. Therefore, we re-examine the near-IR data presented by Hinkle et al. (2007). This paper is organized as follows. In Section 5.2 we briefly describe the observational data. We describe our re-analysis of the spectrum in Section 5.3 then we discuss these results in Section 5.4 and present our conclusions in Section 5.5.

5.2 Observations

We present the high-resolution ($R \approx 50,000$) near-IR (λ from 1 to 5 μm) observations carried out with the Phoenix spectrograph (Hinkle et al., 2003) from the National Optical Astronomy Observatory (NOAO) on Gemini South. These data primarily targeted CO fundamental and overtone lines and were discussed by Hinkle et al. (2007), to whom we refer for a description of the observational details and data reduction.

For each individual data segment, we took note of remaining telluric lines, then performed a heliocentric velocity correction and normalized the data to the continuum. Next, we used a weighted mean (adopting the signal-to-noise, S/N, ratios provided by Hinkle et al., 2007) to merge all the individual segments into a single, final spectrum. Finally, we re-binned the resulting spectrum onto a constant resolution wavelength grid for later comparison to our model spectra.

5.3 Analysis

We begin our analysis of these data with the CO overtone lines in the 2.3 μm region. There are several good reasons for this. First, in this range, the spectrum reveals simple, pure absorption profiles with relatively little blending between the lines. For a given column density, these lines will furthermore have a much lower optical depth than the fundamental lines, offering the best prospects to reliably determine the temperatures and column densities using these

lines. Finally, since the gas in this region of the spectrum is absorbing continuum radiation, its location is constrained: it must be directly along the line of sight to the dusty disk and/or the central star; note though that the stellar continuum will only contribute $\sim 25\%$ of the flux at this wavelength. We will then use our results from the $2.3 \mu\text{m}$ range to better interpret the emission-absorption spectrum at $4.6 \mu\text{m}$.

5.3.1 The $2.3 \mu\text{m}$ Region

The combined spectrum of HR 4049 in the $2.3 \mu\text{m}$ range is shown in Fig. 5.1. We remind the reader that Hinkle et al. (2007), who used these data to produce an excitation diagram for CO, found that the absorption originates from two distinct layers of CO gas in local thermodynamic equilibrium (LTE): a warm layer ($T = 530 \text{ K}$, $N = 1.65 \times 10^{17} \text{ cm}^{-2}$) and a cold one ($T = 40 \text{ K}$, $N = 4.58 \times 10^{18} \text{ cm}^{-2}$).

We first created a plane-parallel slab model in which 1200 K blackbody radiation (representing the dust) is absorbed by the warm layer of CO gas which is in turn absorbed by the cold layer of CO gas using these parameters. We used the CO line list from Goorvitch (1994) and adopted a Gaussian line profile¹ with a full width at half maximum (FWHM) of 10 km s^{-1} . However, when we compared this model to the observations (see the dashed line below the spectrum in Fig. 5.1), we found that the model reproduces neither the depths nor the relative strength ratios of the individual ro-vibrational lines. It is not clear what the origin of this discrepancy is, though this could possibly result from using different line lists. At any rate, an independent analysis of the CO overtone lines is appropriate.

Excitation Diagram First, we constructed our own excitation diagram for the CO first overtone lines. We fit Gaussians to each CO line and integrated these to determine the equivalent width (W_λ). Then we determined the population of each level using

$$N = 1.13 \times 10^{20} W_\lambda / (f_{J'J''} \lambda^2) \quad (5.1)$$

where N is the column density (in cm^{-2}), $f_{J'J''}$ is the oscillator strength for a rovibrational transition (obtained from the CO line list by Goorvitch, 1994), λ is the central wavelength of the transition and both W_λ and λ are measured in \AA (Spitzer, 1978).

We present the resulting excitation diagram in Fig. 5.2. Qualitatively, our results are similar to those obtained by Hinkle et al. (2007), in the sense that our excitation diagram is consistent with two layers of optically thin CO in LTE—a warm and a cold one. However, we find very

¹Note that Hinkle et al. (2007) suggest 16 km s^{-1} ; however, this results in lines that are too broad; see also Sect. 5.3.3.

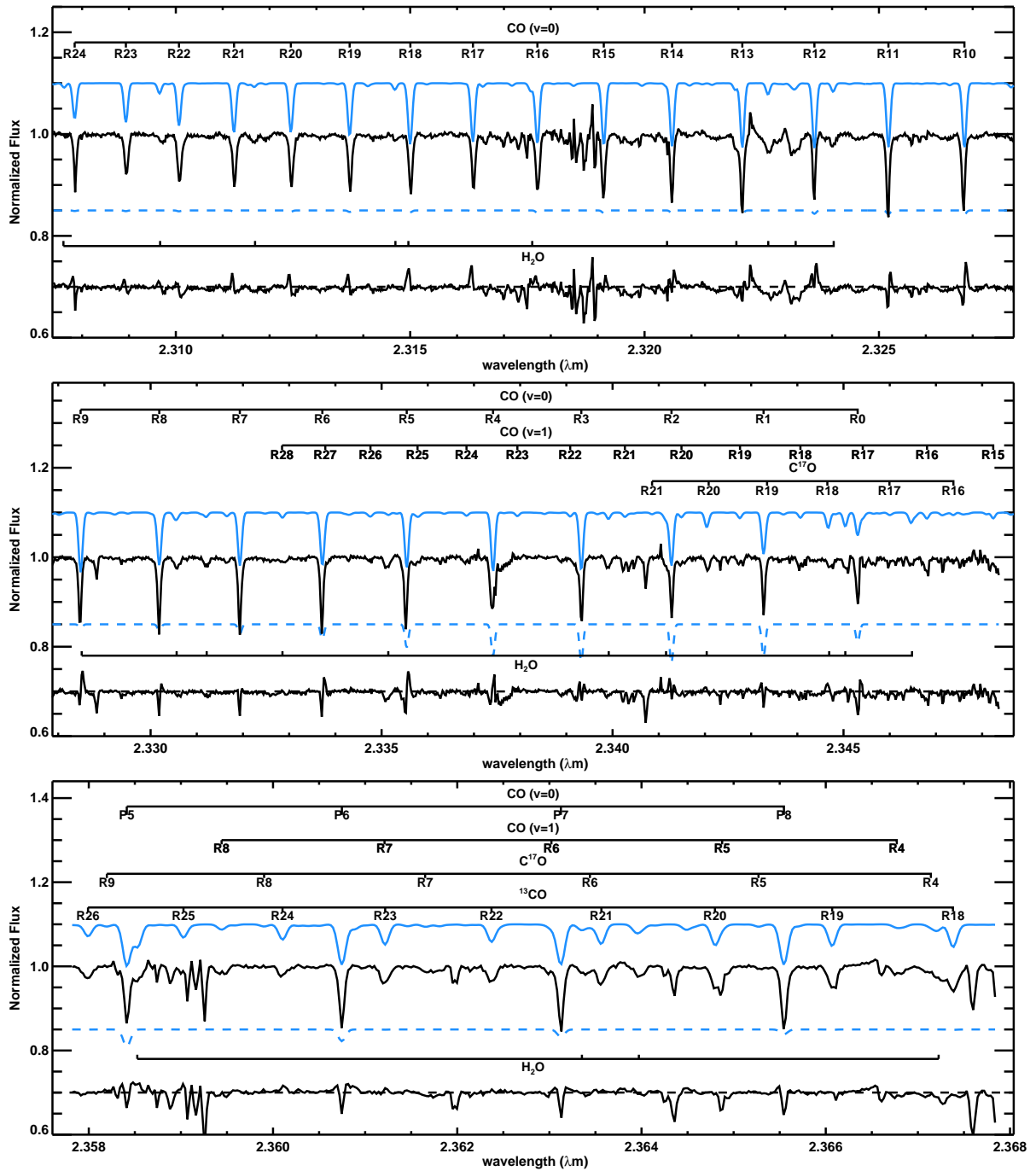


Figure 5.1: We compare the overtone data (black) and the best fit model for CO and H_2O (offset above the spectrum in blue). The CO transitions are labeled above the spectrum and the positions of H_2O absorption lines are indicated below the spectrum. The residual spectrum is offset below the spectrum. We also show the model using the temperatures and column densities determined by Hinkle et al. (2007) in dashed blue lines below the spectrum.

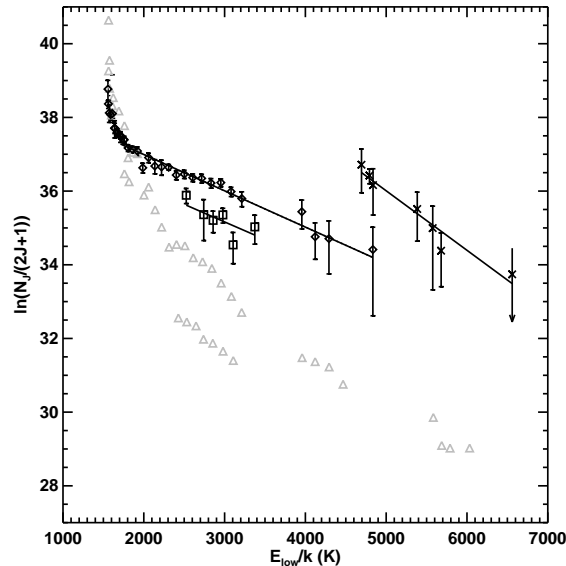


Figure 5.2: Excitation diagram for the overtone CO observations with the $\nu(0 - 2)$ lines indicated by diamonds, the $\nu(1 - 3)$ points indicated by crosses and the ^{13}CO points indicated by squares. The grey triangles indicate the points on the excitation diagram presented by Hinkle et al. (2007). The solid black lines indicate the best fits to the different components. The dashed line shows the extrapolation of the lines originating from the ground state to the first vibrationally excited level.

different values for the temperatures and column densities of the CO gas: our “hot” layer has a temperature of 970 ± 40 K and a column density of $(1.19 \pm 0.04) \times 10^{19} \text{ cm}^{-2}$. The temperature we determine is nearly twice that found by Hinkle et al. (2007) and the column density is two orders of magnitude larger. For the “cold” layer, we find a temperature of 40 ± 10 K and a column density of $(6.1 \pm 0.5) \times 10^{18} \text{ cm}^{-2}$. Here, the temperature and column density are relatively similar to those determined by Hinkle et al. (2007).

If we fit the $\nu(1 - 3)$ lines alone, we find a slight overabundance in the column density and a lower temperature. However, we can also extrapolate the fit for the $\nu(0 - 2)$ lines and find that the population in the $\nu = 1$ state could also be represented reasonably well by this fit. This suggests that the system may be in—or close to—vibrational LTE.

Additionally, for the ^{13}CO lines, we find a column density of $(5.5 \pm 0.6) \times 10^{18} \text{ cm}^{-2}$. This yields a $^{12}\text{C}/^{13}\text{C}$ of 2.1 ± 0.9 , which is slightly lower than the value of 6_{-4}^{+9} reported by Hinkle et al. (2007).

Model Spectra As an independent check, we modeled the CO absorption at $2.3 \mu\text{m}$ using the same methods employed to build the SpectraFactory database (Cami et al., 2010). For these

models, we began once again with CO line lists from Goorvitch (1994, including the ^{13}CO , C^{18}O and C^{17}O isotopologues). From these, we calculated optical depth profiles assuming a population in LTE and a Gaussian intrinsic line profile with a width of 0.5 km s^{-1} (consistent with the b value derived by Hinkle et al., 2007).

We tested a few different model configurations. Initially, we attempted to fit a model consisting of a single layer of LTE gas absorbing a 1200 K blackbody, however, we found that this model did not reproduce all of the CO absorption and found strong residuals, especially for the low J lines. Thus, it seems that at least two layers of CO gas were required; this is consistent with the results from the excitation diagrams. We thus modified our model to include two layers of gas in a slab geometry absorbing a background dust continuum.

In our fit to the CO absorption, we used gas temperatures between 50 and 1000 K in increments of 100 K and column densities between 10^{16} and 10^{20} cm^{-2} in increments of $\log N = 0.2$ for each of the gas layers. We varied $\log[^{12}\text{C}/^{13}\text{C}]$ from 0 to 2; $\log[^{16}\text{O}/^{17}\text{O}]$ and $\log[^{16}\text{O}/^{18}\text{O}]$ from 0 to 3 in increments of 0.2. We also varied the radial velocity (v_{rad}) between -30 and -40 km s^{-1} in increments of 1 km s^{-1} and smoothed our line profiles to yield lines with widths between 2 and 20 km s^{-1} in increments of 2 km s^{-1} to represent the observed line broadening (which is possibly due to the rotation of material in a disk). We compared each model to the entire $2.3 \mu\text{m}$ spectral region and calculated χ_v^2 , the reduced χ^2 statistic for each model.

In Table 5.1, we present the parameters from our best fit model and in Fig. 5.1, we compare this model to the spectrum. We note that this model reproduces the CO absorption very well. In addition, the resulting best-fit temperatures (50 K and 900 K) agree well with those we determined from our excitation diagram (40 K and 970 K) and also the column densities are comparable ($\log N = 18.20$ versus $\log N = 18.7$ for the cold layer and $\log N = 19.20$ versus $\log N = 19.08$ in the hot); this corresponds to a maximum optical depth of $\tau_{\text{max}} \approx 0.5$. We find a χ_v^2 of 3.54 for our best model however, indicating significant residuals.

Note that our model does not only reproduce the ground state $\nu(0 - 2)$ transitions, but also the $\nu(1 - 3)$ lines (see e.g. the R18, R24 and R28 lines in Fig. 5.1). Similarly, the $\nu(1 - 3)$ lines in our excitation diagram are also consistent with the temperature and column density derived for the $\nu(0 - 2)$ lines (see Fig. 5.2). This suggests that the CO gas may even be in vibrational LTE (or close to it).

The critical density for the vibrational levels of CO is $n(\text{H}_2) \approx 10^{12} - 10^{13} \text{ cm}^{-3}$ (Najita et al., 1996), which is much higher than realistic in this environment. However, as described in Paper I, the disk is extremely gas rich and significant radiative trapping is occurring. The gas may thus be radiatively thermalized.

	Model	Excitation Diagram
Gas Layer 1		
Temperature (K)	900 ± 50	970 ± 40
Log N (CO)	19.2 ± 0.1	19.08 ± 0.01
Log N (H ₂ O)	19.4 ± 0.1	...
Gas Layer 2		
Temperature (K)	50 ± 25	40 ± 10
Log N (CO)	18.2 ± 0.1	$18.7^{+0.2}_{-0.3}$
Overall		
¹² C/ ¹³ C	$1.0^{+0.3}$	2.1 ± 0.9
¹⁶ O/ ¹⁸ O	15^{+10}_{-5}	...
¹⁶ O/ ¹⁷ O	4 ± 1	...
Velocity Analysis		
v_{rad} (km s ⁻¹)	-33.0 ± 0.5	-32.7 ± 0.2
v_{FWHM} (km s ⁻¹)	10 ± 1	10.8 ± 0.4

Table 5.1: Temperatures, column densities, isotope ratios and velocity parameters for the model fits to our data with nominal 3σ uncertainties as well as temperatures, column densities and isotope ratios from our excitation diagram as well as velocity parameters from the isolated CO lines.

H₂O

The residual spectrum still exhibits several additional absorption features; some of these are telluric absorption, however, others are consistent with H₂O at the radial velocity of HR 4049. These features are much shallower than the CO lines which makes them much less obvious. We thus recalculated our models for this region with the addition of H₂O using the H₂O line list from Partridge & Schwenke (1997, including the H₂¹⁷O and H₂¹⁸O isotopologues).

We began with the assumption that H₂O was in the same layers as the CO (keeping the same layers reduced the number of free parameters) and varied the column density in each layer between 10^{16} and 10^{20} cm². The best fit for these models indicated an absence of H₂O in the cold molecular layer. Thus, we removed H₂O from our cold CO layer and only included it in the hot layer. Like the hot CO, we find a high column density for H₂O in this region of the spectrum ($\log N = 19.4$), but still corresponding to optically thin lines ($\tau_{\text{max}} \approx 0.14$).

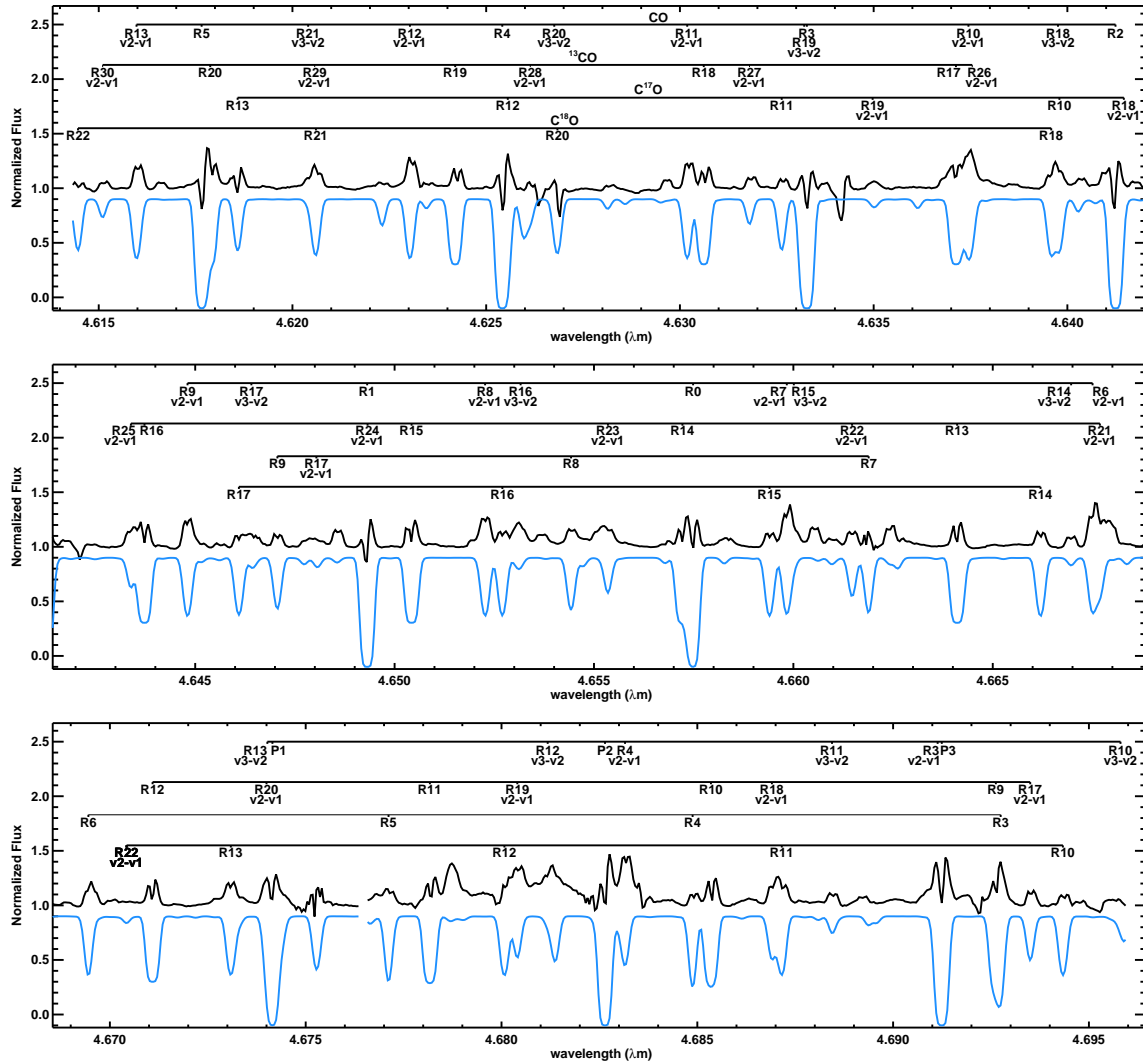


Figure 5.3: The 4.6 μm region of the spectrum of HR 4049 (black) with the absorption model offset below (blue). The individual CO transitions are labeled.

5.3.2 The 4.6 μm Region

Armed with a good characterization of the absorbing gas in the 2.3 μm region, we now turn our attention to the lines near 4.6 μm . We show the spectrum of HR 4049 in this range in Fig. 5.3. In contrast to the pure absorption lines in the CO overtone region, the spectrum here is dominated by emission bands (of both CO and H₂O), many of which show a superposed absorption component as well. Note that some of these absorption features are not just self-absorption of the emission lines, but actually absorb continuum radiation as well.

Such a spectrum, dominated by emission, is somewhat surprising at first sight given our results from above. The overtone lines at 2.3 μm revealed the presence of a hot gas in front of the continuum emission from the star and dust disk. All other things being equal, the same

gas should also produce absorption in the fundamental lines since they originate from the same (ground) state. In fact, since the fundamental lines are intrinsically ~ 100 times stronger than the overtone lines and since the ~ 1200 K blackbody dust emission is almost twice as strong at $4.6 \mu\text{m}$ than it is at $2.3 \mu\text{m}$, we would expect much stronger, saturated absorption lines, as we show in Fig. 5.3. Using the same parameters as for the $2.3 \mu\text{m}$ region, we find that in this range, both the CO and H₂O lines would be very optically thick ($\tau_{\text{MAX}} \sim 100$ for CO and $\tau_{\text{MAX}} \sim 4$ for H₂O) and thus appear as broad, saturated lines. This is in stark contrast with the observations.

Thus, the emission must originate from gas that is not residing in the same line of sight as the gas detected in the overtone and must cover a much larger area to completely fill in the expected absorption. Hinkle et al. (2007) interpreted this in the framework of the wall model and suggested that the gas in absorption was along the inner wall of the disk, while the gas in emission originated from above the cold dust surface. Given our current understanding of the disk from the interferometric and mid-IR spectroscopic observations, this no longer seems to be a viable explanation. Furthermore, the gas in emission must be quite warm (as evidenced by the high J lines and the presence of $\nu(2 - 1)$ and $\nu(3 - 2)$ transitions).

One way to explain these observations is by considering that the line of sight that we probe at $2.3 \mu\text{m}$ is such that the CO is not absorbing the dust emission, but rather the stellar continuum. Given our line depths at $2.3 \mu\text{m}$ and that about 25% of the flux at those wavelengths originate from the star, this could certainly not be ruled out. The total flux we observe is then the sum of this absorbing line of sight and the total emission (gas + dust) of the disk. At the gas temperatures we determined, the gas in the disk would not emit much at $2.3 \mu\text{m}$, thus the main effect would be veiling of the absorption lines by the dust. At $4.6 \mu\text{m}$ however, the starlight contributes only 5% to the continuum, so the depths of the absorption lines would be much more reduced due to veiling. At the same time, the ~ 1000 K gas would also emit very efficiently at $4.6 \mu\text{m}$ and any remaining absorption would be more easily filled in by emission from hot gas.

However, this scenario does not work. If the CO gas in the overtone lines would be absorbing only the stellar radiation, our line of sight through the disk would only probe material at a zero radial velocity since any gas motions would be perpendicular to the line of sight. However, a detailed analysis of the overtone line profiles (see Sect. 5.3.3) shows that the higher J lines have much broader line profiles and thus at least a fraction of the absorption originates from gas with a significant radial velocity; thus, this gas must be absorbing non-stellar radiation.

Therefore, we must conclude that the gas in the overtone region is absorbing dust emission as well. To explain the emission in the fundamental region, there must then be a significant amount of hot gas located in lines of sight that do not intersect the dust emission. At this point, there only seem two plausible locations for that gas.

First, the gas could originate from above (and/or below) the disk midplane, while most of the dust providing the continuum emission would be located near the midplane. As noted by Dominik et al. (2003), the dust settling time for a gas-rich disk is short—typically 150 years for the case of HR 4049; thus, the dust distribution is most likely concentrated near the midplane. At the same time, if the disk is in hydrostatic equilibrium, the high gas temperatures imply that the disk must still have a large scale height. It is thus possible that the dust emission is predominantly originating from the midplane while most of the gas emission is coming from above the midplane. However, there must still be enough (small) dust grains mixed in with the gas at appreciable vertical distances from the midplane to explain the phase-dependent extinction (Waelkens et al., 1991; Acke et al., 2013). Furthermore, if the gas is being heated by the dust, the dust must be able to intercept a sufficient amount of stellar radiation, which would not be possible if all the dust is located at the midplane.

A second possibility is that there is hot gas located inside the dust disk, in the dust-free central cavity. Since the inner boundary of the disk is determined by the sublimation temperature of the dust and since the dissociation temperature for CO (and H₂O) is much larger than the dust sublimation temperature, some gas must indeed be located inside the disk. Some support for an origin inside the disk can be found in the larger widths of the emission components compared to the absorption (by hot gas) in the overtone (see Sect. 5.3.3).

Finally, we should also briefly discuss the absorption components in the emission lines. While most emission lines show some evidence for an absorption component, it is most pronounced in those lines involving the ground vibrational state. Furthermore, the strongest absorption is seen for the low- J lines that even show absorption below the continuum. Thus, this absorption component must originate from a much cooler component (such as the cold component we observe in absorption at 2.3 μm) and cannot be due to self-absorption by the gas (which would not result in continuum absorption). Since some of the absorption lines are slightly blueshifted compared to the emission component, this cold gas may be in an outflow, possibly related to the bipolar lobes.

5.3.3 Kinematics

We also investigated the kinematic properties of the gas. As noted in Sect. 5.3.1, the lines at 2.3 μm appear narrower than the velocity width reported by Hinkle et al. (2007). When we fitted all the overtone lines from the ground state with Gaussians, we determined that the average full-width at half maximum velocity was $v_{\text{FWHM}} = 10 \text{ km s}^{-1}$ rather than their $v_{\text{FWHM}} = 16 \text{ km s}^{-1}$. As an additional check, we also incorporated the line width as a parameter in our full model fit confirmed this result. Note that this also agrees with Lambert et al. (1988) who

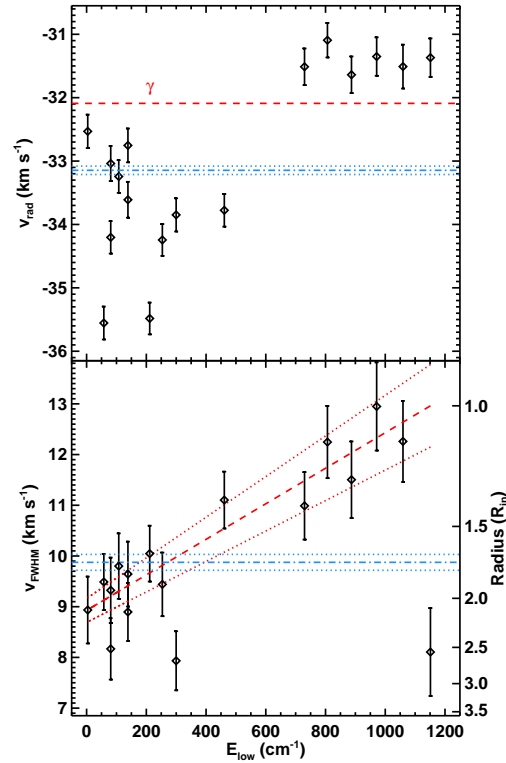


Figure 5.4: The top plot compares the radial velocity of each isolated CO overtone transition to the lower energy of the transition. The blue dot-dashed line shows the weighted mean and the dotted lines indicate the range. The red dashed line indicates the system velocity ($\gamma = -32.07$ km s^{-1} Bakker et al., 1998). The lower plot compares the v_{FWHM} as a function of lower energy. The red dashed line indicates a linear fit to these parameters, with the dotted red lines showing the uncertainties in the fit. Error bars on the velocity measurements are determined with a Monte Carlo technique.

determined that the low J lines were unresolved when observed with an instrumental resolution of 10 km s^{-1} .

To further examine the kinematics of the gas in the disk, we fit unconstrained Gaussian profiles to only the isolated CO overtone transitions from the ground vibrational state (i.e. those that are not blended with lines from hot bands, other isotopologues or H_2O lines) and examined the resulting radial velocities and line widths. We find that on average, the lines have radial velocities of $-32.7 \pm 0.2 \text{ km s}^{-1}$ and a range between -35.5 and -31.1 km s^{-1} . We also find an average line width of $11.0 \pm 0.5 \text{ km s}^{-1}$ and a range between 8.5 and 13.4 km s^{-1} . Interestingly, both the radial velocity and width measurements show some clear variations as a function of the lower state energy of the lines involved (see Fig. 5.4).

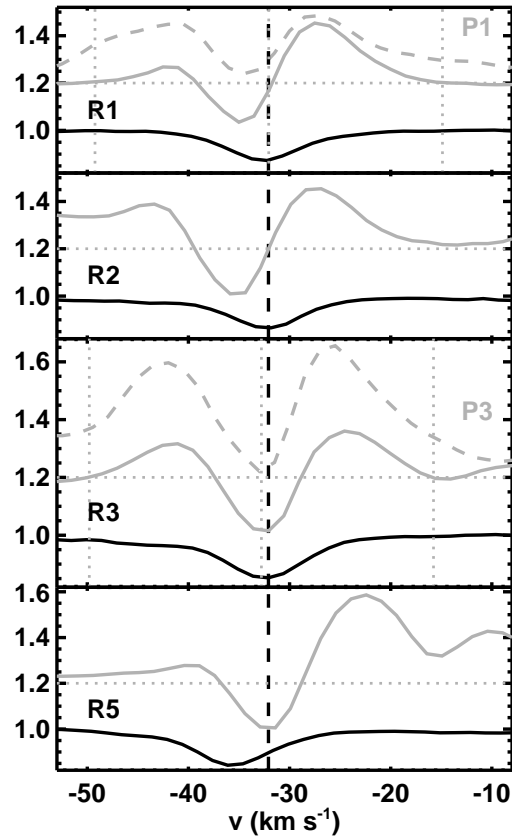


Figure 5.5: A comparison between overtone absorption lines (in black) and the fundamental emission-absorption lines for which the absorption component originates from the same vibrational and rotational states offset by 0.2 (in grey). The R-branch transitions are solid lines while the P-branch transitions are dashed lines. For the R1 and R3 lines we indicate the full width at zero intensity and the midpoint in vertical dotted grey lines. The dashed black line indicates the system velocity. The horizontal grey dotted line indicates the offset in the fundamental observations.

Radial Velocities As seen from Fig. 5.4, we recover a trend noted already by Hinkle et al. (2007, their Fig. 10, but then for the absorption component in the *fundamental* lines): low J lines are blueshifted compared to the higher J lines which are closer to the system velocity. This was interpreted as due to a slow outflow of gas from the system.

To compare both absorption characteristics, we show the profiles of the overtone and fundamental lines that exhibit absorption for lines originating from the same level in Fig. 5.5. Again, we selected only the lines which had relatively clean absorption profiles with as little blending as possible in both the fundamental and the overtone.

It is clear that the centers of the absorption lines do not correspond well to each other; the

$J = 3$ lines are the only ones with a clear overlap. In addition, the variations in the fundamental are different from the overtone: for the overtone the low J lines are at the system velocity and the largest deviations from the system velocity are found for the R5 and R10 lines; for the fundamental, it is only the lowest J lines that are blueshifted.

These observations are hard to explain consistently. For instance, the absorption in the fundamental could on first sight be explained by a cold outflow from the system. Indeed, with the deepest absorption (the R2 line) originating from the $J = 2$ level, this blueshifted gas must have $22\text{K} \lesssim T_{\text{ex}} \lesssim 50\text{K}$. However, at such temperatures, there would still be a significant population in the $J = 3$ state and we would expect to also see the same blueshifted absorption quite strongly in the R3 line—but this is not the case. That points to a low-density gas that is not even in rotational LTE and may be more characteristic of interstellar gas than circumstellar gas.

In the overtone lines, the case for a systematic effect is even less clear (see Fig. 5.4), with some low J lines at the system velocity and others blueshifted. It is not clear at this point whether this represents a true effect or rather points to instrumental or calibration issues.

For completeness, we note that these shifts are only seen in the CO fundamental. There are no discernible trends in the radial velocities of the absorption components of the hot bands and other isotopologues of CO.

Line Widths An interesting trend becomes obvious when looking at the widths of the lines as a function of the lower state energy (bottom panel of Fig. 5.4): overtone absorption lines originating from higher energies are broader than the lower energy lines. A linear fit yields a slope of $(3.4 \pm 1.2) \times 10^{-3} \text{ km s}^{-1} \text{ per cm}^{-1}$. Since only hot gas can contribute to the lines at higher energies and since cold gas dominates the lower energy lines, we conclude that the hotter gas has a larger rotational velocity than the cooler gas, consistent with Keplerian motion in a disk that is hotter on the inside and cooler on the outside. Note that thermal broadening is much smaller than the effect we measure here. We will discuss this further below.

We also note that in Fig. 5.5, the emission component is clearly broader than the overtone absorption. If the broadening mechanism is rotation in a Keplerian disk and the overtone absorption begins at the interior of the dust disk, this suggests that the emission component originates on the interior of the dust disk.

5.4 Discussion

It is clear from our analysis above that the CO (and H₂O) gas probed in the near-IR traces a very complex, gas-rich environment. As pointed out by Dominik et al. (2003), hydrostatic gas

pressure in a gas-rich disk will not only puff up the disk in the vertical direction, but it will also act in radial direction and tend to spread out the disk. Indeed, also the near-IR observations point to such a radially extended disk, in agreement with our conclusions from the mid-IR observations in Paper I.

5.4.1 Dust Temperatures

As we suggest in Sect. 5.3.3, the gas appears to have some temperature variation in which the gas closest to the binary system is hotter than the gas further away. If the gas and dust are mixed, then this should also be true of the dust.

If the dust were grey and in equilibrium with the stellar radiation field, the temperature in the disk would vary from 520 K to 370 K at 15 and 30 AU respectively (using a stellar temperature of 7500 K and a radius of $31 R_{\odot}$ Acke et al., 2013) or 640 and 450 at 10 and 20 AU. The dust must be hotter than this to allow the ~ 1000 K gas component to appear in absorption; indeed, it must be hotter than the gas for the gas to appear in absorption.

In Paper I, we suggest that the optically thick gas in the disk traps and re-radiates the stellar radiation, thus the temperatures of the gas and dust in the disk will increase significantly compared to equilibrium values and they will become more homogeneous. The question thus remains: what type of temperature distribution can the disk have while still reproducing the SED we observe in HR 4049?

As described by Dominik et al. (2003), the SED can be reproduced by the sum of equally weighted black bodies with temperatures between 880 and 1325 K. As well, when they assigned weights for the black bodies based on a power law distribution, they found that the temperatures could vary between 730 and 1238 K. In general, the maximum dust temperature possible is ~ 1300 K.

If the inner rim of the dust component of the disk is determined by the sublimation temperature of the dust, this can put constraints on the type of dust in the disk. For instance, this excludes dust species with high dust condensation temperatures such as e.g. metallic iron or alumina. Instead, we should expect the dust to be composed primarily of dust with a sublimation temperature close to 1300 K.

5.4.2 The size of the gas disk

We can use our measurements to estimate the (radial) size of the gas disk. If we assume that the overtone absorption originates from gas in Keplerian rotation in the disk, the gas velocity

at a distance r from the center of mass is

$$v = \sqrt{\frac{GM}{r}}, \quad (5.2)$$

where G is the gravitational constant, M is the total mass of the binary system (the stars are much closer to each other than the disk is to the stars so they can be treated as a point mass). Since we find v_{in} of 13 ± 3 and v_{out} of 9.2 ± 0.8 , we conclude that $R_{\text{out}}/R_{\text{in}} = (2.0 \pm 0.5)$, compatible with the results by Acke et al. (2013), who determined that the outer radius was $(2.2 \pm 0.3) R_{\text{in}}$ based on their model fits to the interferometric observations and mid-IR SED.

The value for R_{in} is hard to determine, but is most likely between 10 AU (Dominik et al., 2003) and 15 AU (Acke et al., 2013); this would then correspond to outer radii of 20 ± 5 and 30 ± 8 AU and disk surface areas of 900 ± 300 and $2100 \pm 700 \text{ AU}^2$ respectively. The lower values compare especially well to what we determined for the CO_2 gas in the mid-IR where we found an emitting area of 1300 AU^2 (assuming an inclination angle of 60°).

Thus, the circumbinary disk of HR 4049 is a radially extended, gas-rich disk. However, it is not a flat disk. Indeed, the high temperatures of the gas ensure that hydrostatic pressure will still hold up the disk to appreciable vertical scale heights as well, but less than the $H/R \geq 1/3$ that was determined by Dominik et al. (2003).

5.4.3 On the Mass of HR 4049

From v_{in} disk we are able to estimate a mass of the binary system. Using an inclination angle of 60° , we determine a v_{in} of $15 \pm 4 \text{ km s}^{-1}$ at the inner radius; thus, the actual gas velocity is 7.5 km s^{-1} . Then using an inner radius of $15 \pm 1 \text{ AU}$, we find a total mass of $0.94 \pm 0.18 M_\odot$ for the binary. If we then apply the mass function for the primary determined by Bakker et al. (1998, $f(M) = 0.158 \pm 0.004$), we calculate a mass of $0.34 \pm 0.06 M_\odot$ for the primary and $0.60 \pm 0.11 M_\odot$ for the secondary. If we use an inner radius of 10 AU, we determine smaller masses for the binary and individual stars ($M_{\star\star} = 0.64 M_\odot$, $M_1 = 0.17 M_\odot$, $M_2 = 0.46 M_\odot$).

The mass we find for the primary at an inner radius of 15 AU is close to the $0.4 \pm 0.1 M_\odot$ estimated by Acke et al. (2013). It is thus interesting to contemplate the implications of such a low mass for the evolution of the primary. When a star is on the red giant branch (RGB), it burns hydrogen in a shell and adds helium to the core. For a low-mass star, with a degenerate core, the temperature for helium ignition is attained when the core mass reaches $0.45 M_\odot$. Unless part of the core was removed during the common envelope phase, this suggests that either HR 4049 never ignited helium in its core or that it had a non-degenerate core, which can ignite helium at lower masses. However, this latter scenario would require a much higher initial mass for HR 4049, and would suggest that it has lost a great deal of material which is

missing.

When low-mass stars terminate their evolution without igniting helium in their cores, they will end their lives as helium white dwarfs. However, HR 4049 is still a giant star. This suggests that something else may be occurring in this system. Theoretical predictions show that hydrogen shell flashes occur on helium white dwarfs which have sufficient hydrogen atmospheres remaining; these flashes are also thought to return the white dwarf to giant sizes for very short periods of time ($\sim 10^3$ yr; Althaus et al., 2001). The short duration of these flashes is inconsistent with the observational history of HR 4049. Perhaps it has lost most of its envelope, but has kept enough for it to sustain a longer-term hydrogen burning shell. To our knowledge, no evolutionary models of such an object have been attempted.

5.5 Conclusion

Based on our new analysis and re-interpretation of these data, we find that the disk is hot and radially extended, consistent with the results from the mid-IR observations described in Paper I and by the interferometry described by Acke et al. (2013). The gas must play a significant role in determining the physical properties and geometry of the disk. Future radiative transfer modeling should elucidate these effects.

We find evidence that the fundamental CO emission originates from inside the central cavity of the disk and would thus likely end up accreting onto one of the stars in the binary system.

The mass of the system and the individual components are very low and consistent with mass transfer. In particular, the total mass of the system would correspond to a main sequence lifetime on the order of 10 Gyr; such an age is incompatible with the abundances of the system. Therefore, the system must have lost a considerable amount of mass during its evolution.

Bibliography

- Acke B., Degroote P., Lombaert R., et al., 2013, *A&A* 551, A76
- Althaus L.G., Serenelli A.M., Benvenuto O.G., 2001, *MNRAS* 323, 471
- Bakker E.J., Lambert D.L., Van Winckel H., et al., 1998, *A&A* 336, 263
- Cami J., van Malderen R., Markwick A.J., 2010, *ApJS* 187, 409
- Cami J., Yamamura I., 2001, *A&A* 367, L1
- Dominik C., Dullemond C.P., Cami J., van Winckel H., 2003, *A&A* 397, 595
- Goorvitch D., 1994, *ApJS* 95, 535
- Hinkle K.H., Blum R.D., Joyce R.R., et al., 2003, In: Guhathakurta P. (ed.), *Society of Photo-Optical Instrumentation Engineers (SPIE) Conference Series*, vol. 4834 of *Society of Photo-Optical Instrumentation Engineers (SPIE) Conference Series*, pp. 353–363
- Hinkle K.H., Brittain S.D., Lambert D.L., 2007, *ApJ* 664, 501
- Lambert D.L., Hinkle K.H., Luck R.E., 1988, *ApJ* 333, 917
- Lamers H.J.G.L.M., Waters L.B.F.M., Garmany C.D., Perez M.R., Waelkens C., 1986, *A&A* 154, L20
- Malek S., Cami J., submitted to *ApJ*, *ApJ*
- Mathis J.S., Lamers H.J.G.L.M., 1992, *A&A* 259, L39
- Najita J., Carr J.S., Glassgold A.E., Shu F.H., Tokunaga A.T., 1996, *ApJ* 462, 919
- Partridge H., Schwenke D., 1997, "*Journal of Chemical Physics*" 106, 4618
- Spitzer L., 1978, *Physical processes in the interstellar medium*. Wiley & Sons, Inc.
- Van Winckel H., Waelkens C., Waters L.B.F.M., 1995, *A&A* 293, L25

Waelkens C., Lamers H.J.G.L.M., Waters L.B.F.M., et al., 1991, *A&A* 242, 433

Waters L.B.F.M., Trams N.R., Waelkens C., 1992, *A&A* 262, L37

We have a hunger for the mind
which asks us for knowledge of all
around us and the more we gain,
the more is our desire; the more we
see, the more we are capable of
seeing.

Maria Mitchell

Chapter 6

Conclusions and Future Work

Toward the end of its life, a low- or intermediate-mass star will lose the majority of its envelope in a slow, massive wind. As the material ejected from its envelope expands away from the star and cools, it becomes an important site for the formation of complex molecular species and dust grains known as the circumstellar environment (CSE). However, not much is known about the properties and compositions of these CSEs. In addition, the chemical pathways leading to the formation of molecules and dust grains in these environments are not well established either. Furthermore, the effects of the evolution in a binary system on the processing of gas and dust in these environments as well as on the evolution of the stars are also not very well known.

In this thesis, we have made progress toward understanding some of these issues, though we find that our work has perhaps lead to more questions than answers. We will describe some of our important results and conclusions as well as explore some of the possibilities for future research here.

Chemistry in Carbon Stars

In our first project, which we describe in Chapter 3, we analyzed the mid-infrared spectrum of the carbon-rich ($C/O > 1$) pre-planetary nebula (pPN) SMP LMC 11 using data from the Infrared Spectrograph (IRS) on board the *Spitzer* Space Telescope. We found several interesting results which are of importance for understanding the chemical pathways toward the formation of molecular species and dust grains.

We determined that the gas in this CSE is warm ($T = 250 - 375$) and found high column densities for the majority of the molecular species we observed, including C_6H_6 , which is rarely observed in CSEs. We were also able to confirm the presence of CH_3C_2H in the spectrum. Our analysis also suggests that the molecules may reside in a dense torus around the central object.

When we compare our abundances to molecular models and to the pPN CRL 618—the only other pPN in which C_6H_6 has been detected—and to chemical models of CSEs, we find numerous discrepancies. In SMP LMC 11, we do not find evidence for C_6H_2 even though we observe deep absorption from C_4H_2 , and these species are expected to form in the same types of chemical reactions and under the same conditions. Similarly, we could not confirm the presence of HCN or longer cyanopolyynes at all in this spectrum though we observe HC_3N .

These discrepancies are quite intriguing and raise some interesting questions. For instance, we find that compared to CRL 618, the gas in SMP LMC 11 is warmer and denser, which we suggest could be due to a difference in the relative evolutionary states of the two objects (in particular, that SMP LMC 11 left the AGB more recently). However, it is difficult to confirm this since the central star of SMP LMC 11 has not been observed. In addition, there are few observations of objects at these states of evolution so little is known of what to expect from the evolution of the CSE in a star as it evolves.

This points to the need for this type of detailed analysis to be performed on a large number of carbon-rich asymptotic giant branch (AGB) stars and pPNe. Establishing full inventories and relative abundances for many more objects at different points in their evolution would yield valuable insights into the effects of different conditions in the chemistry of the CSEs.

Such an analysis could be undertaken already with observations available in the Spitzer archives. There are a number of spectral observations of carbon-rich AGB and post-AGB stars (including pPNe). While not all of them are as rich in molecular features as the spectrum of SMP LMC 11, some of them could be evolving their way to a similar state. It should be possible to classify these objects based on their evolutionary state and compare how the molecular abundances change as they evolve.

There is also much that is not understood about the evolution of dust in the outflows of carbon-rich environments. However, the dust is very important, most obviously because it drives the outflows from these stars, but also because it later plays important roles in the temperature regulation in the interstellar medium (ISM). An analysis of the molecular features in the outflows of a large number of these stars would also provide the opportunity to examine the formation and processing of the dust in these CSEs since the spectra will also show dust features.

In addition, it would be useful to perform some follow-up observations of SMP LMC 11. While we suspect that this is not an especially unusual object and that indeed many carbon stars eventually go through a phase where they form similar molecular species, it is the only object like it that we know of at this time. Observations at longer wavelengths can probe the cold component of the CSE and yield further insights into the chemical evolution in this environment.

That we also find more C_6H_6 relative to C_2H_2 in SMP LMC 11 compared to either CRL 618 or predictions by the chemical models indicates that for some reason, C_6H_6 is either being formed more efficiently or being destroyed less efficiently in SMP LMC 11. Combined with the unexpected results from the polyacetylene and cyanopolyynes chains, it appears that important chemical pathways are missing in the models for the chemistry in these environments. We thus suggest that additional pathways should be included in future chemical models for carbon-rich environments, including possible ring-closing reactions, which may explain both the abundance of benzene and the absence of long polyacetylene and cyanopolyynes chains.

Stellar Evolution in a Binary System

Our next two projects (described in Chapters 4 and 5) focus on two different regions of the infrared spectrum of the unusual binary HR 4049. For the mid-infrared spectrum of HR 4049, we analyze the CO_2 and H_2O emission. We find that the circumbinary disk of HR 4049 is a very complex environment: the disk is massive, warm, gas-rich and radially extended. There is also evidence for ongoing processing of the dust by the stellar radiation, as we observe a recent—and significant—increase in emission from CO_2 , although it is still not clear what the dust composition is. We are also able to estimate a mass for the primary and find that it may be too low for the star to have undergone a typical evolutionary path, which raises significant questions about what sort of evolutionary state it is in; whatever the evolution, it is not unique and it is evidently quite a long-lived evolutionary state based on the number of objects with similar properties.

Our results point to the need for additional observations of HR 4049. While we find evidence for a radially extended and massive circumbinary disk, we do not know much about the structure of the disk. It would be useful to use the Atacama Large Millimeter Array (ALMA) to map the hot and cold CO lines in the system. Such a study would help characterize the geometry of the disk and place further constraints on its properties (e.g. its mass).

The processing of the dust which appears to be occurring in HR 4049 is another interesting problem. While we see some of the reaction products (CO_2 and H_2O) clearly and find that these have changed recently, it is unlikely that these are the only products of this type of reaction. Indeed, we note that combustion reactions in which polycyclic aromatic hydrocarbons (PAHs) are produced also typically produce H_2O and CO_2 . This thus raises questions about whether the increase in CO_2 emission is perhaps related to the formation of the PAHs in this system and perhaps this is the origin of PAHs in other oxygen-rich environments. Monitoring of similar objects at infrared wavelengths could shed some light on this.

Furthermore, there appear to be some non-local thermodynamic equilibrium (LTE) effects

in the the CO₂ emission in the mid-infrared spectrum. While we note that these effects are small on the overall appearance of the spectrum, including non-LTE effects such as formation pumping in the spectral models could have significant impacts on the estimated temperatures and abundances of the molecules in the system. Such models do not exist for CO₂; note that models for formation pumped CO₂ and H₂O would also be useful for environments other than around evolved stars where these species are formed.

The large column densities of CO₂ and H₂O in the mid-infrared spectrum are particularly interesting for the disk since these molecules are well-known for their ability to effectively trap radiation. Since they are so abundant, it appears possible that they play a significant role in determining the temperature structure of the disk. In particular, this gas may heat the disk significantly and result in a more homogeneous temperature structure within the disk in addition to providing a source of opacity for the mid-infrared continuum emission. This effect has not been included in models for these disks, but is something which we suggest should be included in future models. We furthermore note that these effects can also play a role in other disks as well, including those in young stars. The interaction between the stellar radiation and a long-lived dust disk may also lead to the formation of crystalline silicates in these environments through annealing.

HR 4049 and its class of evolved objects are typically referred to as being in the post-asymptotic giant branch (post-AGB) stage of evolution. However, the mass we estimate for HR 4049 appears to be too low to have ignited helium in its core; without the ignition of helium, the star cannot evolve to the AGB at all and in principle its evolution ceases at the red giant branch (RGB). While this is known to occur in some cases—such as the helium white dwarfs—there are few studies of how much of its envelope a star can lose while continuing hydrogen shell burning or of what the evolutionary path of such a star would be on the HR diagram. While many studies explore the binary interactions of high-mass stars, the evolution of low-mass binary stars is still poorly understood. Current studies of binary interaction among low-mass stars are—to the best of our knowledge—focused on end states such as the helium white dwarfs as opposed to what can occur to a star that loses a significant amount of its envelope, but still retains enough to continue hydrogen shell burning (or if this is possible). This would be a very interesting avenue for future research involving theoretical models and it would answer some of the questions regarding the true evolutionary states of the HR 4049 class of “post-AGB” objects.

With four parameters I can fit an elephant and with five I can make him wiggle his trunk.

John von Neumann

Appendix A

Model Spectra

The molecular bands in the infrared spectra of evolved objects are powerful and important probes of the conditions in their circumstellar environments (CSEs). A very effective way to exploit the appearance of these bands is by creating model spectra and fitting these to the observations while varying the temperature (T) and column density (N) of the various molecular components.

This is the sort of analysis we have applied thus far, however we have not yet described the modelling technique in great detail. Instead, we have only provided a general overview of how the data are modelled and fitted.

Here we will describe in more detail how we calculate these models spectra once we have obtained a line list. We have used optical depth profiles previously calculated using the techniques described in *SpectraFactory* (Cami et al., 2010), however we will begin this discussion with a brief description of how optical depth profiles are calculated including the assumptions which are made in this process in Section A.1. Next, we describe the techniques we use to calculate a model spectrum for a single temperature molecular layer in Section A.2. We also explore how it can be difficult to distinguish between the effects of temperature and column density and describe how we determine the best fit for these parameters as well as how we determine which parameters are statistically significant in Section A.3. Finally, we describe how we calculate models for multiple temperature layers and incorporate kinematical effects in Section A.4.

A.1 Optical Depth Profiles

A line list typically contains the transition energies, probabilities, lower energy levels and quantum numbers for a large number of transitions of a given molecular species. The transition probabilities are expressed using a variety of different ways such as with the Einstein A values

for spontaneous emission, oscillator strengths or line strengths at a given temperature. The first step in the calculation of the optical depth profiles is thus converting these to appropriate units (see e.g. Hilborn, 2002, for details on how to convert between these values).

Once this is done, the relative populations of the individual rovibrational energy levels at a given temperature must be determined. As the temperature of a gas changes, the population of molecules in particular rotational and vibrational levels will also change. Typically, at higher temperatures it is possible for more molecules to populate higher excitation levels.

Here, we assume that the level population is described by local thermodynamic equilibrium (LTE) such that the line strength (S_{ν_0}) for a transition at a particular frequency (ν_0) and given temperature (T) is given by (Rybicki & Lightman, 1979):

$$S_{\nu_0} = \frac{h\nu_0}{4\pi} g_1 B_{12} \frac{e^{-E_1/kT}}{P(T)} (1 - e^{h\nu_0/kT}), \quad (\text{A.1})$$

where B_{12} is the Einstein coefficient for absorption, E_1 is the lower energy level of the transition, g_1 is the statistical weight for the lower energy level, h is the Planck constant, k is the Boltzmann constant and $P(T)$ is the partition function. The partition function is defined such that

$$P(T) = \sum_i g_i e^{-E_i/kT} \quad (\text{A.2})$$

which is summed over all energy levels. These are often calculated at different temperatures for a line list and it is possible to interpolate between these calculated values to obtain the value for a partition function at a different temperature. There are also sometimes polynomial functions which describe the partition function reasonably well for a particular species (e.g. for CO as described by Goorvitch, 1994).

The Einstein coefficient for absorption (B_{12}) is related to the coefficients for spontaneous emission (A_{21}) and stimulated emission (B_{21}) through the *Einstein relations*:

$$g_1 B_{12} = g_2 B_{21} \quad (\text{A.3a})$$

$$A_{21} = \frac{2h\nu^3}{c^2} B_{21} . \quad (\text{A.3b})$$

Here, c is the speed of light. These properties are also sometimes referred to as the *detailed balance relations* and hold whether or not an atom or molecule is in LTE.

While molecules emit and absorb photons of particular energy levels, there are various mechanisms which broaden emission and absorption lines. Thus, each individual line will

have a particular normalized profile ($\phi(\nu)$). This must be multiplied by the total strength of each transition to obtain the optical depth ($\tau(\nu)$) over a narrow range of frequencies:

$$\tau_\nu = NS_{\nu_0}\phi(\nu) , \quad (\text{A.4})$$

where N is the column density (in cm^{-2}) of the molecules along our line of sight.

Possible broadening mechanisms include Doppler broadening (in which the line is broadened by the motion of the particles), natural broadening (in which a line is broadened due to the uncertainty in the energy level due to the uncertainty principle) and collisional broadening (in which a line is broadened by collisions with other particles).

For the purpose of our models we include Doppler broadening for which the profile function is described by:

$$\phi(\nu) = \frac{1}{\Delta\nu_D \sqrt{\pi}} e^{-(\nu-\nu_0)^2/(\Delta\nu_D)^2} . \quad (\text{A.5})$$

Here $\Delta\nu_D$ is the Doppler width, defined as:

$$\Delta\nu_D = \frac{\nu_0}{c} \left(\frac{2kT}{m} + v_{\text{turb}}^2 \right)^{1/2} , \quad (\text{A.6})$$

where m is the mass of the molecule and v_{turb} is the microturbulent velocity. In this equation, the broadening due to the thermal motion of the particles (described by the first term) is combined with the microturbulent velocity. Since we typically model relatively *cool* gas, the microturbulent velocity usually dominates. We have used widths of 10 km s^{-1} (in Chapter 3), 3 km s^{-1} (in Chapter 4) and 0.5 km s^{-1} (in Chapter 5).

A.2 Single Layer Model

The simplest type of model we employ involves a single layer of molecules either in emission or absorbing a continuum source. We use this type of modeling procedure in our analysis of SMP LMC 11 (described in Chapter 3) and in the mid-infrared spectrum of HR 4049 (described in Chapter 4).

For these models, the molecular layer is assumed to be in LTE and we model it as an isothermal slab. Radiative transfer calculations are carried out using

$$I_\nu = I_\nu^0 e^{-\tau_\nu} + B_\nu(T) (1 - e^{-\tau_\nu}) , \quad (\text{A.7})$$

where I_ν is the final intensity, I_ν^0 is the intensity of the background source, τ_ν is the optical depth

for the molecules and $B_\nu(T)$ is the source function (here a black body at the same temperature as the molecules).

In the spectrum of SMP LMC 11, the molecular layer is absorbing a continuum caused by thermal emission of dust, so I_0 represents the dust continuum which we defined as a 400 K black body. In the mid-infrared spectrum of HR 4049, we observe molecular emission which we determined to be consistent with molecules at a lower temperature than expected from the background material. Thus, we modelled this emission without a background layer. In a single layer model without a background source, I_ν^0 is 0 and Equation A.7 simplifies to:

$$I_\nu = B_\nu(T)(1 - e^{-\tau_\nu}). \quad (\text{A.8})$$

Once we have calculated the radiative transfer equation for the molecular layer, we smooth it to instrumental resolution. For the high resolution modes of the Infrared Spectrograph (IRS) on board the *Spitzer* Space Telescope (short high; SH $\lambda = 9.9 - 19.6 \mu\text{m}$ and long high; LH $\lambda = 18.7 - 37.2 \mu\text{m}$), this is 600. Then we compare these to the data.

The optical depth profiles we use are actually normalized by column density. This allows us to vary the column density easily (e.g. without calculating entirely new optical depth profiles for each model). In addition, when we have multiple molecular species and isotopologues in one region of the spectrum, we also combine their optical depth profiles until this becomes too computationally expensive.

A.2.1 Effects of Temperature and Column Density

Thus far, we have described how temperature and column density play a role in the radiative transfer calculations. However we have not yet described the role they play in the overall appearance of the spectrum. While one might naïvely think that distinguishing between the effects of temperature and column density is a simple task, it is not always so. For instance, increasing the column density increases the maximum intensity of the emission or depth of the absorption, but so does increasing the temperature. Increasing temperature and column densities both increase the width of the bands. We illustrate this in Figs. A.1 to A.3 where we show the effect varying the temperature and column density in CO_2 when it appears in emission at a resolution of 600.

In Fig. A.1, we show the ν_2 bending mode of CO_2 at $15 \mu\text{m}$. Here we vary the column density in each column (from $N = 10^{15}$ to 10^{19} cm^{-2}) and the temperature in each row. In this figure, the bands are all normalized to the peak flux between the $15 \mu\text{m}$ and $4 \mu\text{m}$ bands. If they were not normalized, the peak flux would increase with both increasing temperature and increasing column density. Since the plots in Figs. A.1 and A.3 are normalized to whichever

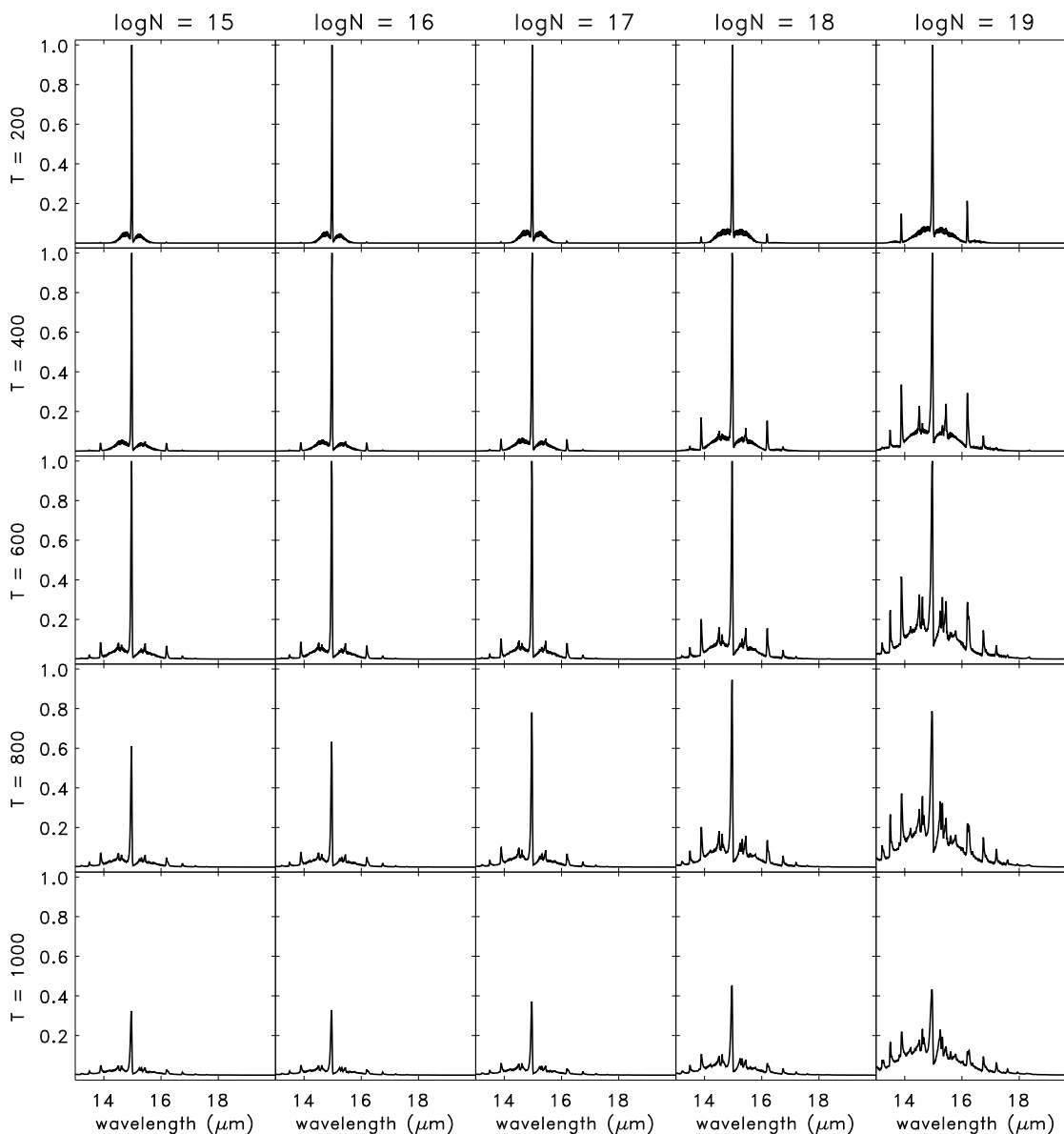


Figure A.1: A series of plots showing CO_2 at a range of temperatures (cooler at the top, hotter at the bottom) and column densities (denser toward the right). These plots have been normalized to the height of the highest peak (in the case of temperatures greater than 600 K, this means the peak at $4 \mu\text{m}$).

is larger (the 15 or $4 \mu\text{m}$ band) we are able to see another effect of temperature, which is that vibrational modes with larger energies become stronger at higher temperatures. However this effect is only noticeable when there are multiple vibrational bands. In addition, since higher densities are required to achieve vibrational LTE than rotational LTE, it is more difficult to predict the appearances of different vibrational bands.

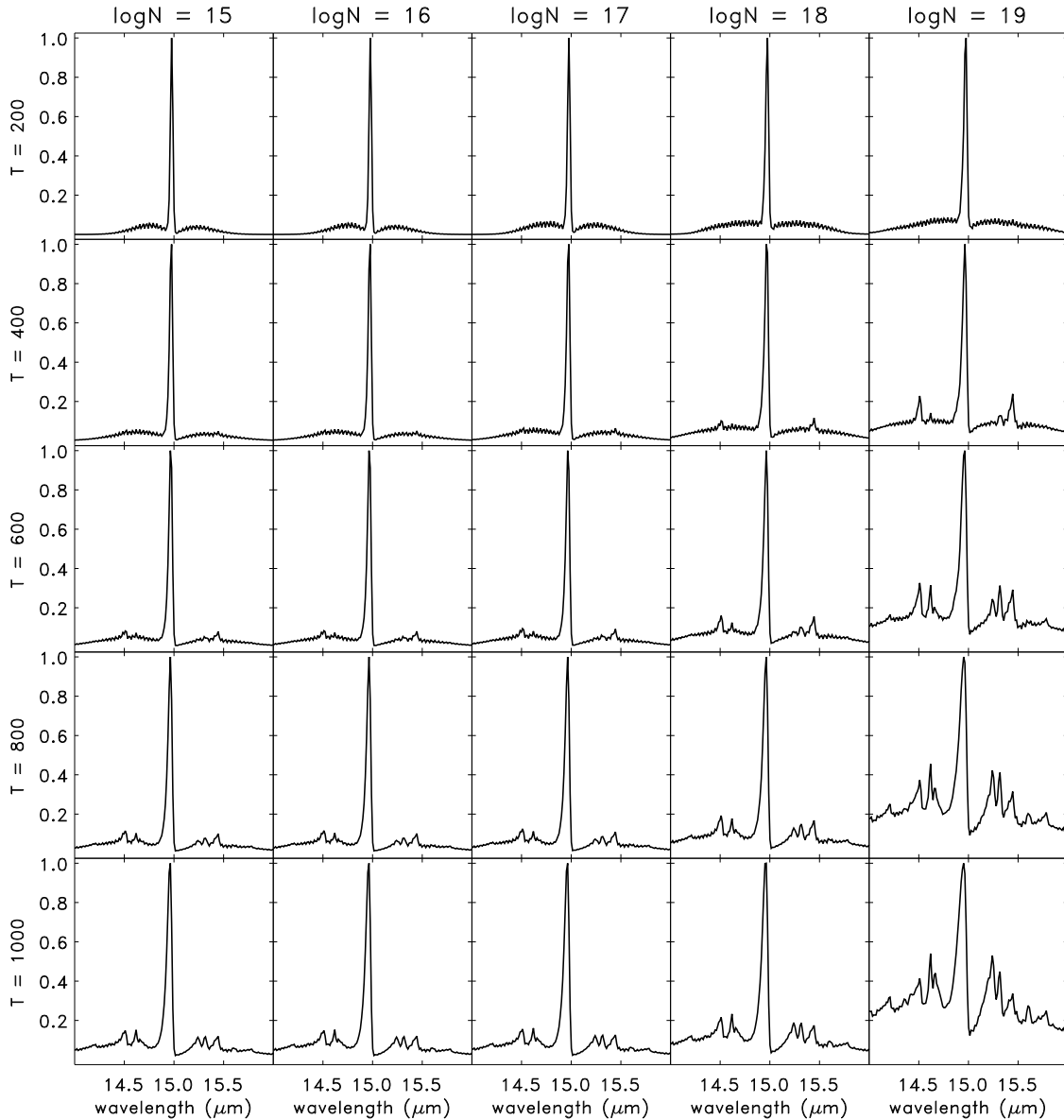


Figure A.2: A series of plots showing CO₂ at a range of temperatures (cooler at the top, hotter at the bottom) and column densities (denser toward the right). These plots have been normalized to the peak of the 15 μm emission.

Looking down a column, we see that the widths of the molecular bands increase with temperature. This is because vibrational and rotational levels with higher energies are more populated at higher temperatures, which broadens the bands. In CO₂, these additional transitions are often combination bands (e.g. the $10^0 01 - 01^1 01$ vibrational transition at $13.873 \mu\text{m}$)¹, though

¹Here we use the notation employed in Herzberg (1989) with the addition of a Fermi polyad ranking ($v_1 v_2^l v_3 r$ where v_1 , v_2 and v_3 are the excitation of the fundamental vibrational modes, l indicates the vibrational angular momentum quantum number for the v_2 mode and r gives the Fermi polyad ranking of the level.

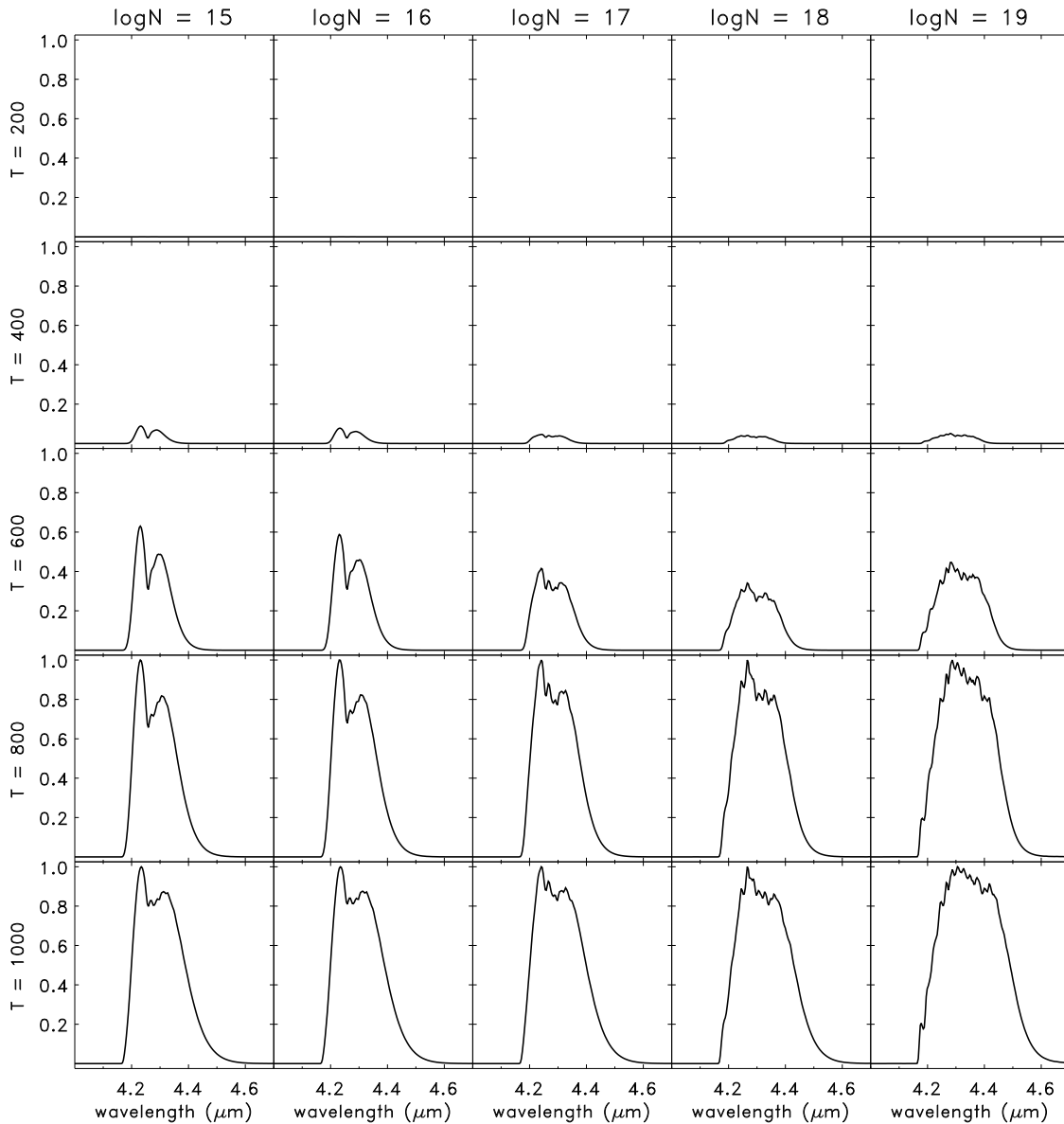


Figure A.3: A series of plots showing CO₂ at a range of temperatures (cooler at the top, hotter at the bottom) and column densities (denser toward the right). These plots have been normalized to the height of the highest peak (in the case of temperatures greater than 600 K, this means the peak at 4 μm).

they are also often overtone transitions (a list of some of the features in the 15 μm region is provided in Table A.1).

Looking across a column, we also see that as the column density increases, the width of the band increases. This occurs because increasing the column density will increase the optical depth and at high column densities, the value of the optical depth will reach and exceed 1 (the

line is then called *optically thick*). If we refer to Equation A.7, we note that the relationship between the intensity and optical depth goes as $e^{-\tau}$. The strongest lines will become optically thick first and when this occurs, the amount of additional flux from increasing the column density becomes smaller. The lines which are not yet optically thick will thus contribute with increasing strength relative to the strongest lines, broadening the bands.

Thus if we look from the top right plot in Fig. A.1 to the plot below and to the left, we note that the overall width of the band is roughly similar and continuing along the diagonal, this is also roughly true. The primary difference along the diagonals is the increase in the number of smaller spikes. Without fully modeling an emission feature in this fashion, however, it can be difficult to distinguish between these effects.

This is also true in Fig. A.2 where we show a small wavelength region surrounding the main ν_2 band at $15 \mu\text{m}$. Overall, increasing the temperature or column density increases the width of the main band, but we also see that increasing the column density leads to an increase in the flux of some of the small peaks. Note that the main peak at $15 \mu\text{m}$ increases primarily on the blue side, especially at higher temperatures. This is due to an increase in excitation of the higher vibrational bands. In Table A.1, we see that these peak slightly to the blue of the 01^101 to 00^001 transition.

If we compare the effects of temperature and column density on the $4 \mu\text{m}$ band as in Fig. A.3, we note that this band becomes significantly stronger relative to the $15 \mu\text{m}$ band at higher temperatures. If we look at the peak positions for the P- and R-branches in the $\log N = 15$ column, we also note that these shift and that the gap between them begins to fill in at higher temperatures. Filling in this gap is also something that occurs at higher column densities.

In emission, there is an additional parameter which will alter the total emission in a band: the size of the emitting region. When gas is optically thin, it can be difficult to distinguish the between the effects of increasing column density and increasing the size of the emitting region since both will cause an increase in overall emission. In optically thick gas, however, increasing the column density does relatively little to change the total amount of molecular emission. Thus, it is possible to directly determine the size of the emitting region, as described in Chapter 4.

A.3 Statistical Techniques

The creation of model spectra thus allow us to probe a greater variety of molecular features in more conditions. However, to compare these model spectra to observational data and determine which model produces the best fit requires robust statistical analyses.

λ (μm)	E_{trans} (cm^{-1})	ν_{upper}	ν_{lower}	E_{upper} (cm^{-1})	E_{lower} (cm^{-1})
9.401	1063.6	00 ⁰ 11	02 ⁰ 01	2349.1459 ^a	1285.5 ^c
10.406	960.955333	00 ⁰ 11	10 ⁰ 01	2349.1459 ^a	1388.1905 ^a
12.636	791.4	11 ¹ 01	02 ⁰ 01	2076.8590 ^a	1285.5 ^c
13.482	741.7234	11 ¹ 01	02 ² 01	2076.8590 ^a	1335.1356 ^a
13.873	720.8083	10 ⁰ 01	01 ¹ 01	1388.1905 ^a	667.3823 ^a
14.521	688.6685	11 ¹ 01	10 ⁰ 01	2076.8590 ^a	1388.1905 ^a
14.959	668.4738	04 ⁴ 01	03 ³ 01	2671.725 ^b	2003.2512 ^a
14.967	668.1156	03 ³ 01	02 ² 01	2003.2512 ^a	1335.1356 ^a
14.976	667.7533	02 ² 01	01 ¹ 01	1335.1356 ^a	667.3823 ^a
14.983	667.3823	01 ¹ 01	00 ⁰ 01	667.3823 ^a	0.0
15.270	654.866	01 ¹ 01	00 ⁰ 11	3004.016 ^b	2349.150 ^b
15.324	652.324	12 ² 02	11 ¹ 02	2585.049 ^b	1932.4724 ^a
15.499	645.2	04 ² 01	03 ¹ 01	2577.7 ^c	1932.5 ^c
15.456	647.0	03 ¹ 01	02 ⁰ 01	1932.5 ^c	1285.5 ^c
16.178	618.1177	02 ⁰ 01	01 ¹ 01	1285.5 ^c	667.3823 ^a
16.644	600.8	04 ⁴ 01	03 ¹ 01	2671.725 ^b	1932.5 ^c
16.740	597.4	03 ¹ 01	02 ² 01	1932.5 ^c	1335.1356 ^a
17.188	581.798	12 ² 02	03 ³ 01	2585.049 ^b	2003.2512 ^a
17.575	568.962	13 ³ 02	04 ⁴ 01	3240.688 ^b	2595.049 ^b
18.372	544.3	03 ¹ 01	10 ⁰ 01	1932.5 ^c	1388.1905 ^a

Table A.1: Transition wavelengths with corresponding upper and lower vibrational states for the main CO₂ isotopologue in the 10—19 μm range.

To fit observational data, we create a series of different models by selecting temperatures and column densities, then performing the appropriate radiative transfer calculations described by Equation A.7. If necessary, we normalize the observations by dividing out the continuum and then we smooth the data to instrumental resolution.

Once we have calculated a model, we compare it to the observations by fitting the χ^2 , which is defined as:

$$\chi^2 = \sum_i \left(\frac{x_{\text{model}}^i - x_{\text{obs}}^i}{\sigma^i} \right)^2. \quad (\text{A.9})$$

Here x_{model}^i is an individual model point, x_{obs}^i is the corresponding data point and σ^i is the error on the data (Bevington & Robinson, 2003).

As we compare different models to the observations and systematically vary the temperatures and column densities, we determine the χ^2 for each model fit to the data. When we find the lowest value for χ^2 in our parameter set, we have found the best fit. We are able to calculate a *reduced* χ^2 value (χ^2_ν) by dividing the χ^2 by the degrees of freedom (ν , defined by removing

the number of parameters we use from the total number of points included in our fit).

The reduced χ^2 describes the *goodness of fit* for a model. A model where $\chi^2_v \approx 1$ is generally a good fit. A value significantly greater than one can indicate either that the model is not good, that the error on the data has been underestimated or that there are systematic issues in the fit; values less than one can be *over fit*, which suggests that there are too many parameters included in the model or that the uncertainties on the data are overestimated.

It is often not obvious which parameters are necessary to include in a model. Adding more terms will inevitably decrease the χ^2 , but they may not decrease it in a significant and meaningful way. Fortunately, there are ways to distinguish between parameters which have a statistically significant impact on the fit and those which do not. One way to determine this is using what is known as an F-test for an additional term.

If we have a model with m parameters which fit N data points, it has $N - m$ degrees of freedom (ν_1). We can also determine a χ^2 value for the fit of this model to the data, which we will call $\chi^2(m)$. If we add an additional parameter to our model, we then have $m + 1$ parameters, $N - m - 1$ degrees of freedom (ν_2) and $\chi^2(m + 1)$.

To determine whether this additional parameter is significant, we take the difference between the two χ^2 values and divide them by the reduced χ^2 of the model with the additional parameter. Thus we obtain the expression (Bevington & Robinson, 2003):

$$F_\chi = \frac{\Delta\chi^2}{\chi^2_v(m + 1)} = \frac{\chi^2(m) - \chi^2(m + 1)}{\chi^2(m)/(N - m - 1)}. \quad (\text{A.10})$$

If F_χ is large, the additional parameter has made a significant difference and should be included in the model; if it is small then we would say that there is some chance that the same improvement in fit could be achieved with the addition of any random parameter.

How large an F_χ value has to be for us to declare that the parameter is significant depends on the number of degrees of freedom and typically, we calculate a probability, $P_F(F : 1, \nu_2)$ describing the likelihood of significance. Bevington & Robinson (2003) include a table with these probabilities, but there also exist routines to calculate them.

A.4 Multi-Layer Models

In Chapter 5, we describe the near-infrared spectrum of HR 4049 which includes CO and H₂O absorption at 2.3 μm . It was already noted by Hinkle et al. (2007) that the CO overtone showed absorption consistent with two layers of gas at different temperatures in LTE. Thus we began to create simple two layer models for the gas. Adding an additional gas layer is relatively simple and it is mostly a matter of adding an additional step to Equation A.7 so that:

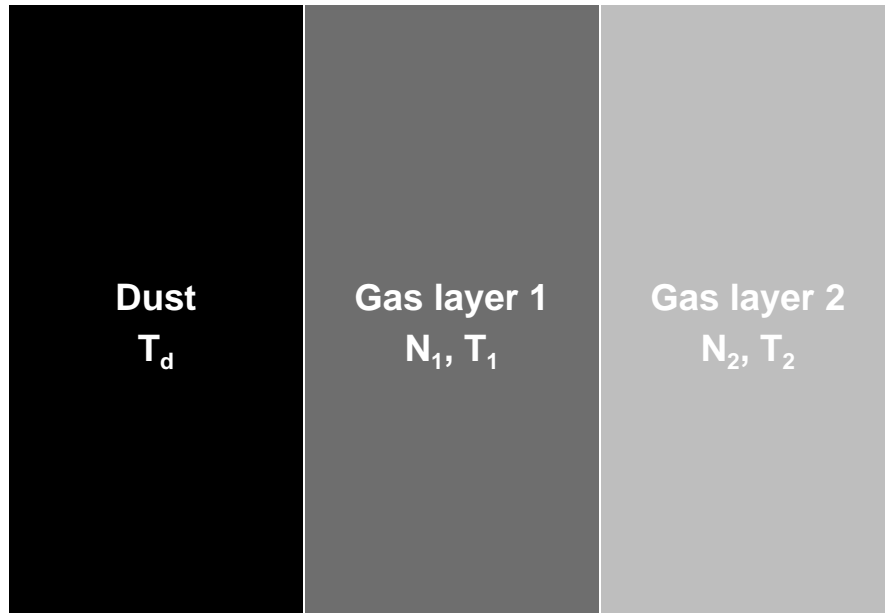


Figure A.4: A schematic of a model in which radiation from the dust (black) is absorbed first by one layer of gas (dark grey) and then by another (light grey). The photons are travelling from the left to the right through each layer.

$$\begin{aligned}
 I_v^1 &= I_v^0 e^{-\tau_{v,1}} + B_v(T_1) (1 - e^{-\tau_{v,1}}) \\
 I_v^2 &= I_v^1 e^{-\tau_{v,2}} + B_v(T_2) (1 - e^{-\tau_{v,2}})
 \end{aligned}
 \tag{A.11}$$

where we have added sub- and superscripts to the different intensity components, optical depths and temperatures to distinguish the two layers. We show a schematic of this type of model in Figure A.4. Note that here, the temperature in the first molecular layer will be warmer than that of the cold molecular layer ($T_1 > T_2$) and the dust is hotter than both gas layers.

In principle, additional layers of gas can be added in a similar process. It is also possible to create a model in which the dust background changes along different lines of sight through the gas though for that it may be necessary to change the weight along different lines of sight to reflect the relative size of the background and gas sources.

Bibliography

Bakker E.J., Lambert D.L., Van Winckel H., et al., 1998, *A&A* 336, 263

Bevington P.R., Robinson D.K., 2003, Data reduction and error analysis for the physical sciences

Bujarrabal V., Alcolea J., 2013, *A&A* 552, A116

Cami J., van Malderen R., Markwick A.J., 2010, *ApJS* 187, 409

Dominik C., Dullemond C.P., Cami J., van Winckel H., 2003, *A&A* 397, 595

Goorvitch D., 1994, *ApJS* 95, 535

Herzberg G., 1989, Molecular Spectra and Molecular Structure II. Infrared and Raman Spectra of Polyatomic Molecules. Krieger Publishing Company

Hilborn R.C., 2002, *ArXiv Physics e-prints*

Hinkle K.H., Brittain S.D., Lambert D.L., 2007, *ApJ* 664, 501

Rybicki G.B., Lightman A.P., 1979, Radiative processes in astrophysics

Curriculum Vitae

Name: Sarah Malek

Post-Secondary Education and Degrees: University of Western Ontario
London, ON, Canada
2009 – 2013 PhD

University of Western Ontario
London, ON, Canada
2007 – 2008 MSc.

McMaster University
Hamilton, ON, Canada
2002 – 2007 BSc. (Hons)

Honours and Awards: Ontario Graduate Scholarship for Science and Technology
2010–2011

Best Student Poster Prize, CASCA General Meeting
2008

Related Work Experience: Research Assistant
The University of Western Ontario
2008 – 2013
Teaching Assistant
The University of Western Ontario
2008 – 2013

Publications

Refereed Journal Articles

Malek, S. E., Cami, J., A Detailed Study of the Gas in HR 4049 I: The Mid-Infrared Spectrum, *submitted to The Astrophysical Journal*

Malek, S. E., Cami, J., Bernard-Salas, J., The Rich Circumstellar Chemistry of SMP LMC 11, 2012, *The Astrophysical Journal* 744, 16

Cami, J., Bernard-Salas, J., Peeters, E., Malek, S. E., Discovery of C₆₀ and C₇₀ in a Young Planetary Nebula, 2010, *Science* 329, 1180

Conference Proceedings

Cami, J., Bernard-Salas, J., Peeters, E., Malek, S. E., Fullerenes in Circumstellar and Interstellar Environments, 2011, in the Proceedings of IAU Symposium 280 “The Molecular Universe”, 216-227

Malek, S. E., Cami, J., The Rich Carbon Chemistry of SMP LMC 11, 2011, in ASP Conf. Ser. 445 Why Galaxies Care about AGB Stars II: Shining Examples and Common Inhabitants (San Francisco, CA; ASP), 347